

Solar resource modelling and shading tolerant modules for the urban environment

Calcabrini, A.

DOI

[10.4233/uuid:02485fcb-1445-4479-9308-518b579e3a6d](https://doi.org/10.4233/uuid:02485fcb-1445-4479-9308-518b579e3a6d)

Publication date

2023

Document Version

Final published version

Citation (APA)

Calcabrini, A. (2023). *Solar resource modelling and shading tolerant modules for the urban environment*. [Dissertation (TU Delft), Delft University of Technology]. <https://doi.org/10.4233/uuid:02485fcb-1445-4479-9308-518b579e3a6d>

Important note

To cite this publication, please use the final published version (if applicable). Please check the document version above.

Copyright

Other than for strictly personal use, it is not permitted to download, forward or distribute the text or part of it, without the consent of the author(s) and/or copyright holder(s), unless the work is under an open content license such as Creative Commons.

Takedown policy

Please contact us and provide details if you believe this document breaches copyrights. We will remove access to the work immediately and investigate your claim.

**SOLAR RESOURCE MODELLING AND SHADING
TOLERANT MODULES FOR THE URBAN
ENVIRONMENT**

SOLAR RESOURCE MODELLING AND SHADING TOLERANT MODULES FOR THE URBAN ENVIRONMENT

Dissertation

for the purpose of obtaining the degree of doctor
at Delft University of Technology,
by the authority of the Rector Magnificus Prof.dr.ir. T.H.J.J. van der Hagen,
chair of the Board for Doctorates
to be defended publicly on
Thursday 26 October 2023 at 10:00 o'clock

by

Andres CALCABRINI

Master of Science in Sustainable Energy Technology,
Delft University of Technology, the Netherlands
born in Quilmes, Argentina.

This dissertation has been approved by the

promotor: Prof.dr. M. Zeman

promotor: Prof.dr.ir. O. Isabella

copromotor: Dr. P. Manganiello

Composition of the doctoral committee:

Rector Magnificus,

Prof.dr. M. Zeman,

Prof.dr.ir. O. Isabella,

Dr. P. Manganiello,

chairperson

Delft University of Technology, promotor

Delft University of Technology, promotor

Delft University of Technology, copromotor

Independent members:

Dr. H. Hanifi

AE Solar, Germany

Prof.dr. G. Spagnuolo

Università degli Studi di Salerno, Italy

Prof.dr. H. Nussbaumer

ZHAW School of Engineering, Switzerland

Prof.dr. E. Eisemann

Delft University of Technology

Prof.dr. M. Popov

Delft University of Technology, reserve member



ISBN 978-94-6384-492-5

Copyright © 2023 by A. Calcabrini

All rights reserved. No part of this publication may be reproduced, stored in a retrieval system, or transmitted in any form or by any means without the prior written permission of the copyright owner.

An electronic version of this thesis is available at <http://repository.tudelft.nl/>.

Printed by *Ipskamp Printing, the Netherlands*.

*All models are wrong,
but some are useful.*

George Box

CONTENTS

Summary	xi
Samenvatting	xiii
1 Introduction	1
1.1 Need for photovoltaics	1
1.2 Photovoltaics in the urban environment	2
1.3 Aim and outline of this work	4
1.4 Main contributions to the field	4
2 Simplified irradiation model for urban environments	7
2.1 Introduction	7
2.2 Time-resolved simulation approaches	8
2.2.1 Transposition model	9
2.2.2 Thermal-electrical model	14
2.3 Simplified irradiation model	15
2.3.1 Solar irradiation indicators.	15
2.3.2 Skyline profiles.	16
2.3.3 Simplified irradiation model	18
2.3.4 Simplified energy yield model	20
2.4 Benchmarking and validation.	20
2.4.1 Benchmark study in different climates.	20
2.4.2 Validation study in the Netherlands	22
2.4.3 Validation study in different climates	24
2.5 Conclusions.	25
3 Detailed irradiance modelling in complex scenarios	27
3.1 Introduction	27
3.2 Irradiance models.	28
3.3 Basic radiometric concepts	30
3.4 The proposed simulation approach.	31
3.4.1 Ray tracing.	31
3.4.2 Irradiance components evaluation.	34
3.4.3 Sky classification.	37
3.5 Irradiance simulations with <i>Radiance</i>	37
3.6 Computational complexity	39
3.7 Experimental validation.	40
3.7.1 Measurement setup	40
3.7.2 Simulation parameters.	42
3.7.3 Irradiation simulations.	43

3.7.4	Spectral simulations	46
3.8	Conclusions.	47
4	Shading tolerant PV module topologies	49
4.1	Introduction	49
4.2	Study cases	52
4.2.1	Shading scenarios	52
4.2.2	Module topologies	53
4.3	Simulation framework	54
4.4	I-V curve approximation	55
4.4.1	The squared approximation	55
4.4.2	Validity of the squared approximation	56
4.5	Results and discussion	58
4.5.1	String inverters vs MLPE	58
4.5.2	PV systems with MLPE	59
4.6	Conclusions.	63
5	A series-parallel reconfigurable PV module	65
5.1	Introduction	65
5.2	Reconfigurable PV generators.	66
5.3	The series-parallel reconfigurable PV module.	66
5.3.1	Reconfiguration algorithm	68
5.4	Energy yield simulation	72
5.4.1	Simulation framework	72
5.4.2	Results	73
5.5	Indoor experimental validation	78
5.5.1	Evaluation of module configurations.	78
5.5.2	Evaluation of the reconfiguration algorithm	80
5.6	Outdoor experimental validation	81
5.6.1	Reconfigurable PV module performance.	84
5.7	Limiting the electrical operating range	87
5.8	A word on reliability.	90
5.9	Conclusions.	91
6	PV modules with low breakdown voltage solar cells	93
6.1	Introduction	93
6.2	Low breakdown voltage IBC solar cells	94
6.3	Breakdown voltage simulations	95
6.4	Annual energy yield simulations	98
6.4.1	Simulation framework	98
6.4.2	Simulation results	100
6.5	Experimental validation.	103
6.6	Conclusions.	107
7	Conclusion and Outlook	109
7.1	Conclusions.	109
7.2	Outlook	111

Acknowledgements	113
List of Publications	135
Curriculum Vitae	137

SUMMARY

The deployment of photovoltaic (PV) systems in urban environments has the potential to supply a significant share of the urban energy demand and help us reduce greenhouse emissions in the hope of alleviating the consequences of climate change. Moreover, recent advancements in the integration of PV technology into multi-functional architectural elements, offer the possibility to deploy solar cells almost on every surface of the urban fabric.

In this dissertation, the solar energy potential of the urban environments and approaches for improving the performance of urban PV systems are investigated. The first part of this thesis is focused on computational models to evaluate the solar radiation reaching a PV system in complex geometric environments. The second part, delves into the effects of partial shading on the electrical output of PV systems and proposes strategies to increase the shading tolerance of PV modules.

In Chapter 2, a model for the computation of the solar irradiation in urban environments is presented. The model proposes a simplification in the calculations using two indicators to quantify the effect of the skyline profile on the annual irradiation received by a PV module. The reduced computational cost of the simplified irradiation model enables the evaluation of the energy potential using digital elevation models to find the best places for installing specific PV systems in urban areas.

Once the best places are identified, a more detail analysis of the irradiance incident on each of the solar cells of a PV module is needed to obtain an accurate estimation of the electrical yield of the system. In Chapter 3, a ray tracing simulation approach is proposed for the calculation of the irradiance incident on PV systems in complex geometric environments. The approach consists in decoupling the calculations to extend the simulation capabilities of current ray tracing models. The proposed approach enables the simulation irradiance with high temporal and spectral resolution in scenes with time-varying optical properties. A validation study using different types of solar radiation sensors suggests that the accuracy of the approach is comparable to other state-of-the-art ray tracing simulation models for PV systems. Moreover, it is expected that the implemented features will contribute to increase the accuracy of the simulation of bifacial PV systems and future tandem modules.

Starting in Chapter 4, the electrical performance under partial shading condition of different systems and module topologies is evaluated employing simulations and experiments. The results of the simulation study presented in Chapter 4, facilitate the quantification of the annual energy yield enhancement that can be achieved with shade tolerant PV modules topologies with bypass diodes and parallel interconnections. This analysis demonstrates that shade tolerant module topologies are particularly beneficial when shading is caused by objects situated in close proximity to the modules.

In Chapter 5, the concept of reconfigurable PV generators is explored as a strategy to mitigate current mismatch losses caused by partial shading. A version of a series-

parallel reconfigurable PV module is proposed and compared through simulations to shade tolerant module topologies with static interconnections. Moreover, the outdoor performance of the proposed reconfigurable module is evaluated using a full-scale prototype under different shading scenarios. While it is important to reduce the electrical output range of the reconfigurable module to facilitate the design of an appropriate power converter, results suggest that the dynamic reconfiguration of the electrical interconnections within the module can boost the energy yield in partially shaded locations by more than 10 %.

Finally, Chapter 6 is dedicated to the analysis of the role of the reverse current-voltage characteristics of solar cells in the performance of partially shaded PV modules. In particular, the breakdown characteristics of interdigitated back contact solar cells with tunnelling oxide passivating contacts is investigated. An approach to reduce the breakdown voltage is evaluated through device-level simulations and the effect of the breakdown voltage on the energy yield is estimated by performing system-level simulations. These simulations are complemented by outdoor experiments with PV modules composed of solar cells with different breakdown characteristics. Results indicate that reducing the breakdown voltage of solar cells can improve the electrical performance of partially shaded PV modules between 4 % and 20 %, while simultaneously minimising the thermal stress in reverse biased solar cells.

SAMENVATTING

Het implementeren van fotovoltaïsche systemen in de gebouwde omgeving heeft het potentieel om in een significant gedeelte van de stedelijke energievraag te voorzien en kan ons helpen om de uitstoot van broeikasgassen te verminderen, in de hoop de gevolgen van klimaatverandering te minimaliseren. Bovendien bieden recente ontwikkelingen op het gebied van de integratie van fotovoltaïsche technologie in multifunctionele architectonische elementen de mogelijkheid om zonnecellen op bijna ieder oppervlak in de gebouwde omgeving toe te passen.

In dit proefschrift wordt het potentieel van zonne-energie in stedelijk gebied onderzocht, evenals manieren om de prestaties van stedelijke fotovoltaïsche systemen te verbeteren. Het eerste gedeelte van dit proefschrift richt zich op rekenmodellen om de zonne-instraling te evalueren die een fotovoltaïsch systeem in complexe geometrische omgevingen bereikt. Het tweede deel gaat in op de effecten van gedeeltelijke schaduw op de elektriciteitsproductie van fotovoltaïsche systemen en stelt strategieën voor om de tolerantie van fotovoltaïsche modules ten aanzien van schaduw te vergroten.

In hoofdstuk 2 wordt een model gepresenteerd voor het berekenen van zonne-instraling in stedelijk gebied. Het model stelt een versimpeling in de rekenmethodiek voor waarbij gebruik wordt gemaakt van twee indicatoren om het effect te kwantificeren dat het profiel van de horizon heeft op de jaarlijkse instraling die wordt opgevangen door een fotovoltaïsche module. De verminderde vereiste rekenkracht van het versimpelde instralingsmodel maakt het mogelijk om het energiepotentieel te evalueren op basis van digitale hoogtemodellen en zo de beste plekken te vinden om een gegeven fotovoltaïsche systeem te installeren in stedelijk gebied.

Zodra de beste plaatsen zijn geïdentificeerd, is een meer gedetailleerde evaluatie van de instraling die valt op elk van de zonnecellen van een fotovoltaïsche module noodzakelijk om een nauwkeurige inschatting te verkrijgen van de elektriciteitsopbrengst van het systeem. In hoofdstuk 3 wordt een benadering met een ray-tracing simulatie voorgesteld voor de berekening van de instraling die valt op PV-systemen in complexe geometrische omgevingen. De aanpak bestaat uit het loskoppelen van de berekening om de simulatiemogelijkheden van huidige ray-tracing modellen uit te breiden. De voorgestelde aanpak maakt het mogelijk om de simulatie van instraling met hoge temporale en spectrale resolutie toe te passen in omgevingen met optische eigenschappen die variëren in de tijd. Een validatie studie die gebruik maakt van verschillende type zonne-instralingsensoren suggereert dat de nauwkeurigheid van de aanpak vergelijkbaar is met andere state-of-the-art ray-tracing simulatiemodellen voor fotovoltaïsche systemen. Bovendien wordt verwacht dat de toegepaste functies bij zullen dragen aan een hogere nauwkeurigheid van de simulatie van tweezijdige fotovoltaïsche systemen en toekomstige tandem-modules.

Vanaf hoofdstuk 4 wordt de elektrische prestatie van verschillende systeem- en module-configuraties bij gedeeltelijke schaduw bestudeerd door gebruik te maken van si-

mulaties en experimenten. De resultaten van de simulatiestudie die wordt gepresenteerd in hoofdstuk 4, maakt het mogelijk om de verbetering van de jaarlijkse energieopbrengst te kwantificeren die kan worden bereikt met schaduw-tolerante fotonvoltaïsche module topologieën die bypass diodes en parallelle verbindingen tussen zonnecellen bevatten. Deze analyse toont aan dat schaduw-tolerante module topologieën vooral gunstig zijn wanneer de schaduw wordt veroorzaakt door objecten die zich dichtbij de modules bevinden.

In hoofdstuk 5 wordt het concept van herconfigureerbare fotonvoltaïsche opwekkers verkend als een strategie om mismatch-verliezen te voorkomen die worden veroorzaakt door gedeeltelijke schaduwvorming. Een serie-parallele herconfigureerbare fotonvoltaïsche module wordt geïntroduceerd en met behulp van simulaties vergeleken met schaduw-tolerante module-topologieën met vaste verbindingen. Bovendien wordt de buitenprestatie van de voorgestelde herconfigureerbare module geëvalueerd door gebruik te maken van een prototype op ware grootte dat wordt blootgesteld aan verschillende schaduw scenario's. Hoewel het belangrijk is om het bereik van de uitgangsstroom te verkleinen om het ontwerp van een geschikte omvormer te vergemakkelijken, suggereren de resultaten dat dynamische herconfiguratie van de elektrische verbindingen in de module de energieopbrengst op gedeeltelijk beschaduwde locaties met meer dan 10% kan verhogen.

Tenslotte is hoofdstuk 6 gewijd aan de studie naar de rol van achterwaartse stroomspanning karakteristieken van zonnecellen in de prestatie van gedeeltelijk beschaduwde fotonvoltaïsche modules. In het bijzonder worden de doorslagkarakteristieken van interdigitated-back-contact zonnecellen met tunnelling oxide passivating contacten onderzocht. Een manier om de doorslagspanning te verlagen is bestudeerd met simulaties op zonnecel-niveau en het effect van de doorslagspanning op de energieopbrengst wordt ingeschat door middel van simulaties op systeemniveau. De simulaties worden ondersteund door buitenexperimenten met fotonvoltaïsche modules die bestaan uit zonnecellen met verschillende doorslagkarakteristieken. De resultaten laten zien dat het verlagen van de doorslagspanning van zonnecellen de elektrische prestaties van gedeeltelijk beschaduwde fotonvoltaïsche modules kan verbeteren met waarden tussen 4% en 20%, terwijl tegelijkertijd de thermische spanning in zonnecellen met een achterwaartse spanning wordt geminimaliseerd.

1

INTRODUCTION

Climate change is the most threatening challenge the world has ever faced. It has the potential to trigger uncountable crises with irreversible effects and directly endangers life on Earth. Without any doubt, this human-induced phenomenon is going to have unavoidable and regretful consequences for our planet. In this context, time is of the essence, and immediate action is needed to prevent further exacerbation of the problem.

1.1. NEED FOR PHOTOVOLTAICS

The energy sector is the largest contributor to greenhouse gas emissions, which are the primary cause of climate change [1]. On top of that, the worldwide primary energy consumption has shown an average annual increase of 1.4 % over the last decade driven by population growth, urbanisation, and economic development [2]. Anticipated trends indicate that energy consumption will continue in its growth trajectory, particularly in developing countries, which will further contribute to the emission of greenhouse gases. These facts put in evidence the urgent need for a transformation that requires a coordinated effort from all sectors of society to accelerate the electrification of the energy sector and the substitution of fossil fuels with cleaner energy sources.

Currently, only 13 %¹ of the total global power generation is supplied by renewable sources [2]. Although the total sustainable power generation capacity is still low, it has been growing at an average annual rate of 14.9 % over the last decade. In particular, the growth of the installed photovoltaic (PV) capacity has been the fastest among all sustainable energy technologies. Throughout the past decade, the installed PV capacity has experienced an average 27.9 % growth per year, reaching 849 GW_p in the year 2021 [3].

Certainly, the expansion of PV power generation capacity has been truly remarkable. However, Figure 1.1 shows the great challenge that still lies ahead. In order to meet the Net Zero Emissions by 2050 Scenario (NZE2050), the annual PV generation growth needs to remain at 25 % for the coming decade [4]. This ambitious goal is only reachable if

¹Excluding hydroelectricity.

PV installations are rapidly deployed not only in large-scale solar farms, but also in the commercial and residential sectors.

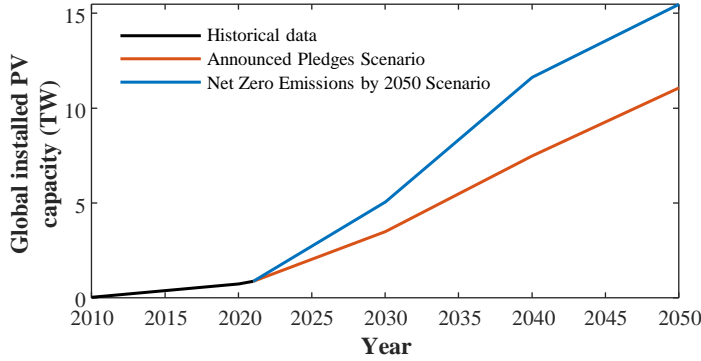


Figure 1.1: Global installed solar PV capacity by scenario. Data from year 2022 retrieved from [5].

1.2. PHOTOVOLTAICS IN THE URBAN ENVIRONMENT

The expansion in population and the increasing energy demand have led to a growing interest in PV systems as a source of sustainable energy in urban environments. According to the International Energy Agency, the installed capacity of PV systems in urban areas is expected to grow significantly, and the residential PV market is anticipated to more than triple in size during the 2020-2030 decade [6]. In addition, it is estimated that over 2 TW_p could be installed on suitable rooftops only in the European Union and the United States [7], [8]. However, urban PV deployment is not limited only to roofs. Solar cells can be incorporated into various architectural elements beyond traditional rooftops, including façades [9], carports [10], and shading structures [11]. The integration of PV technology extends to a wide range of building components, such as tiles [12], windows [13], shading devices [14] and chimneys [15], resulting in multi-functional building elements, which can provide additional functionality such as weather protection, thermal insulation, and privacy.

The installation of PV systems on existing building surfaces and infrastructure maximises the use of the limited space in urban areas and reduces the need for additional land to be dedicated to energy generation. Additionally, the deployment of PV systems in urban areas contributes to the distributed generation of electricity. Decentralised urban PV generation can help to improve the reliability of the electrical grid system providing grid stability and power quality, while reducing the need for large-scale transmission and distribution infrastructure.

Consumers can also benefit directly from urban PV. A reduced dependence on centralised grids provides an increased resilience to power outages and improves energy security. Additionally, distributed generation of electricity can reduce the cost of energy for consumers, as they are not subject to the same losses and costs associated with the transmission of electricity over long distances.

Nevertheless, there are several challenges that urban PV needs to overcome. In particular, the nominal operating hours of PV systems in the urban environment are typically 10 % to 40 % lower compared to PV systems in rural environments [16]. The main factors influencing the performance of urban PV systems include:

- **Orientation and tilt:** The orientation and tilt angle at which PV modules are installed affect how much sunlight they receive. Ideally, fixed PV systems should be installed facing South in the northern hemisphere, and facing North in the southern hemisphere. The optimal tilt angle for fixed PV modules depends on the latitude and the ratio of diffuse to beam irradiance at the installation site. However, in the urban environment, the orientation and tilt of PV modules are often constrained by the building structures on which they are mounted, and it is common to find PV systems installed vertically and facing East or West [17], [18].
- **Shading:** Shadows from buildings, trees, and other urban structures reduce the amount of solar radiation that can reach the PV modules, directly impacting the energy yield of the PV system [19]. Partial shading is particularly problematic because typically solar cells in a PV module are connected in series forming a string, and shading even one cell can restrict the current flow through the whole string reducing the power output of the entire module. In addition, shading can lead to the formation of hot spots, which can shorten the lifetime of PV modules and cause permanent damage to the cells.
- **Temperature:** Urban environments tend to be hotter than rural areas due to the urban heat island effect [20]. Moreover, the way PV modules are usually mounted or integrated in urban structures limits the airflow on the rear side of the modules, contributing to rise the module temperature even further [21]. As a consequence of the increase in the module temperature, the conversion efficiency of solar cells is significantly reduced². High temperatures can also cause thermal stress on the modules, which can lead to warping, cracking, and other physical damage that impacts negatively the yield of the PV system [22].
- **Air pollution:** Urban environments are often associated with high levels of air pollution, which can reduce the efficiency of PV panels over time [23], [24]. Regular cleaning and maintenance is important for optimal performance, especially in urban environments where dust and debris tend to accumulate more quickly on the surface of PV modules.

The reduced specific energy yield caused by the above-mentioned factors is one of the reasons why the levelised cost of electricity (LCOE) of urban PV systems is significantly higher compared to utility scale solar farms. However, with proper placement and design, most of these effects can be mitigated, enabling urban PV systems to provide significant amounts of clean and economical sustainable energy.

²In the case crystalline silicon, an increase of 10 °C in the module temperature causes a conversion efficiency reduction between 2.5 % and 4 %

1.3. AIM AND OUTLINE OF THIS WORK

The objective of this dissertation is to investigate the performance of PV systems in the urban environment and explore different strategies to improve it. The first part of this study concentrates on developing simulation models to compute the solar radiation reaching a PV system in complex geometric environments. The second part of this research delves into the effects of shading on the electrical output of PV modules and proposes two strategies to improve their shading tolerance.

This dissertation is organised in seven chapters, with Chapter 1 (this chapter) serving as the introductory chapter.

Chapter 2 presents a simplified irradiation model to determine the most suitable locations for installing PV systems in urban areas based on indicators of the solar potential.

Once the best locations are identified, higher levels of detail and accuracy are required to compute the irradiance on each cell of a PV module. In Chapter 3, a ray tracing simulation approach is proposed to evaluate the spectral irradiance incident on surfaces in complex urban environments with time-varying optical properties.

Due to the intricate geometry of urban environments, shading can affect even the most favourable locations. Chapter 4 explores the effect of partial shading on the electrical performance of PV modules, and proposes a simple approach to estimate the energy yield of PV modules with bypass diodes and series/parallel interconnections.

Chapter 5 is dedicated to the investigation of a reconfigurable PV module design enhanced with a switching matrix that dynamically modifies the electrical interconnections between solar cells to maximise the power generated under partial shading. The shading tolerance of the reconfigurable module concept is evaluated through simulations and experiments.

Chapter 6 presents an analysis on the impact of reverse current-voltage characteristics of solar cells on the electrical output of partially shaded PV modules. An approach to improve the performance of reverse biased solar cells is explored and the potential energy yield gain from using PV modules made with low breakdown voltage solar cells is assessed.

Finally, the conclusions of this study are presented in Chapter 7 together with recommendations for future research.

1.4. MAIN CONTRIBUTIONS TO THE FIELD

The research outlined in this dissertation makes a series of small but significant contributions to the field of photovoltaics. The main highlights are summarised below:

- A calculation method for the direct estimation of the solar irradiation in urban environments with reduced computational cost.
- A ray tracing simulation approach that enables the computation of spectral irradiance in complex geometric scenarios with time-varying optical properties by decoupling the ray tracing calculations from the illuminations conditions and the optical reflectivity of the surfaces in the scene.
- An extensive evaluation of the shading tolerance of various PV system and PV module topologies in different urban shading scenarios.

- An in-depth analysis of reconfigurable series-parallel PV modules as a means of improving the shading tolerance of PV systems.
- A study of the role and impact of the reverse characteristics of solar cell on the shading tolerance of PV modules.

2

SIMPLIFIED IRRADIATION MODEL FOR URBAN ENVIRONMENTS

This chapter is based on the following publication:

A. Calcabrini, H. Ziar, O. Isabella, M. Zeman, *A simplified skyline-based method for estimating the annual solar energy potential in urban environments.*, Nature Energy **4**, 206 (2019).

2.1. INTRODUCTION

The declining cost of photovoltaic technology and the improvement in the aesthetics of PV modules are contributing to the rapid expansion of photovoltaics in urban environments. Beyond the traditional Building Added Photovoltaics (BAPV), today the PV market is offering more alternatives for Building Integrated Photovoltaics (BIPV) [25]. In the near future, technological advances will make it possible to deploy PV almost on any surface of the urban fabric [26]–[28]. In this context, simulation tools will become increasingly important to ensure the energy gain and profitability of PV systems.

Over the last decades, multiple simulation tools have been developed to compute the solar irradiation and the energy yield of PV systems in urban environments. Some of these include *In my backyard tool* [29]; the *PVsites project* [30]; ray-tracing-based methods [31]–[33]; various GIS-based tools [34], [35]; among many others reported in a comprehensive review by Freitas et al. [36]. The vast majority of these tools calculate the hourly irradiance incident on the plane of array (PoA) considering the sky luminosity distribution, the module tilt and orientation, and the objects surrounding the target surface [37]. Then, hourly irradiance values can be integrated to determine the annual solar energy potential. For this reason, such methodologies for calculating the solar potential are herein referred to as time-resolved approaches.

Time-resolved approaches are useful when the power generated by a PV system at

every hour during a year is of interest. However, in some cases, only the annual energy potential is of interest. For instance, when looking at the optimum locations to install a distributed PV system in an urban planning framework, it might be necessary to estimate its annual energy yield at a large number of locations. In this case, hourly irradiance levels are merely intermediate calculations that are needed to compute the annual integral and find the optimal locations. When the solar potential needs to be evaluated over large areas, the repetitive calculations combined with the complex geometry of the landscape make time-resolved approaches computationally extensive [38], [39].

In an effort to simplify the calculations and reduce the computation time, different methodologies and indicators for solar potential in urban environments have been explored. For example, the work of Robinson [40] uses the sky view factor as an irradiation indicator in locations with a high amount of diffuse radiation. Rodriguez et al. present in [41] an urban modelling platform for estimating the solar potential using the 3D geometry of buildings and the simple Hay and Davies sky model to reduce the computation time [42]. More recently, Chatzipoulka et al. presented a study for vertical façades, where the sky view factor is correlated with the global irradiation to facilitate the calculations [43]. These approaches, although mostly applicable to cloudy climates, are useful to give a quick estimation of the solar potential available in urban environments.

This chapter presents a model for the direct estimation of the solar energy potential in urban areas, which implies a significant reduction in computation effort compared to time-resolved models. The proposed model is based on the correlation between the annual irradiation and two parameters that quantify the skyline profile: the sky view factor (*SVF*) and the sun coverage factor (*SCF*). The numerical coefficients correlating annual irradiation and skyline profile, are valid within a climatic region and can be quickly calculated for a specific module tilt and orientation using a time-resolved model and synthetic skyline profiles. After the coefficients are computed, the problem of calculating the PoA irradiation at any real location is reduced to capturing the skyline profile. The *SVF* and the *SCF* of the real skyline profile can be then computed and - with the pre-calculated coefficients - it is possible to obtain a quick estimation of the annual irradiation.

In the following section the time-resolved approach employed to calculate the required correlation coefficients is explained. Subsequently, a detailed description of the proposed model is presented. In the final section, the model is benchmarked against the time-resolved approach and validated with actual PV system data.

2.2. TIME-RESOLVED SIMULATION APPROACHES

Most time-resolved approaches for calculating the annual irradiation and energy yield of a PV module combine irradiance, thermal, and electrical models. These models constitute a simulation framework, as the one depicted in Figure 2.1, which enables the calculation of the instantaneous irradiance on the plane of array and the electric power generated by the PV module.

Most irradiance models implemented in PV simulation software are transposition models, which combine direct normal irradiance (*DNI*), diffuse horizontal irradiance (*DHI*) and global horizontal irradiance (*GHI*) values to compute the global irradiance on the plane of array.

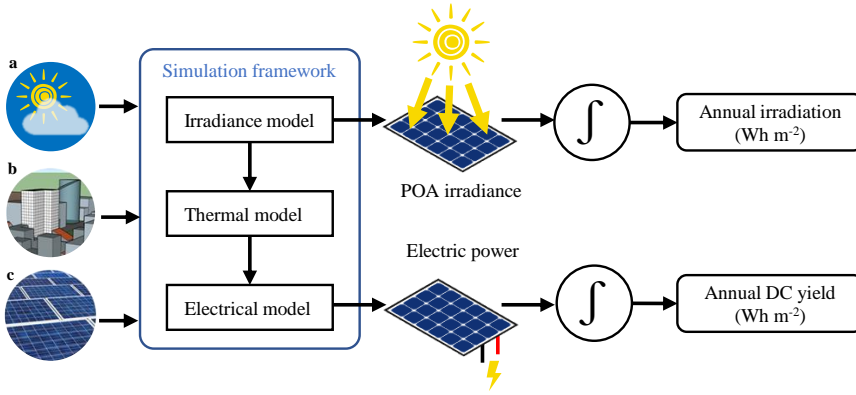


Figure 2.1: General block diagram of the simulation framework of time-resolved approaches for calculating the annual irradiation on a surface and the PV system's annual DC yield. The required inputs are clustered in three groups. **(a)** Meteorological data, i.e., irradiance measurements, ambient and ground temperature, wind speed and cloud cover. **(b)** Location specifications, including geographical coordinates and a 3D model of the landscape and objects surrounding the PV module. **(c)** PV module data, which include mechanical, dimensional, electrical, optical and thermal parameters of the PV module. The irradiance model uses the location specifications and the meteorological data to calculate the amount of solar irradiance impinging on the plane of array of the PV module. The thermal model allows to determine the operating temperature of the PV module which, together with the computed irradiance, are the inputs to the electrical model to calculate the instantaneous power generated by the PV module.

2.2.1. TRANSPPOSITION MODEL

The transposition model employed in this chapter combines three irradiance components to calculate the total (or global) plane of array irradiance (G_{tot}), namely the beam¹ (G_{beam}), the diffuse (G_{diff}) and the reflected (G_{refl}) components.

$$G_{\text{tot}} = G_{\text{beam}} + G_{\text{diff}} + G_{\text{refl}} \quad (2.1)$$

The beam component G_{beam} is proportional to DNI [44] and can be expressed as:

$$G_{\text{beam}} = DNI \cdot \cos(AOI) \quad (2.2)$$

where AOI is the angle between the solar vector and the normal to the surface of the PV module [45].

The diffuse irradiance component G_{diff} is calculated from DHI . In this chapter, the simplified version of the Perez model [46] is used. The simplified Perez model divides the diffuse irradiance into three sub-components, namely isotropic (G_{iso}), circumsolar (G_{cir}), and horizontal ribbon (G_{hr}), which respectively correspond to the terms in Equation (2.3):

$$G_{\text{diff}} = DHI \cdot \left((1 - F_1) \cdot SVF + F_1 \cdot \frac{a}{b} + F_2 \cdot \sin(\theta_M) \right) \quad (2.3)$$

¹In transposition models, the beam component is also frequently referred to as direct component. Herein the term "direct" is employed in contrast to "reflected", to refer to radiation that reaches the module without interacting with any other surrounding surfaces.

where F_1 and F_2 are the empirical coefficients corresponding to the circumsolar and horizontal ribbon components, a and b are geometrical coefficients that depend on the solar position, and SVF is the sky view factor.

For a tilted module mounted close to the ground, the reflected irradiance component (also called the albedo component) is considered to be proportional to the albedo coefficient of the ground surface α_s :

$$G_{\text{refl}} = GHI \cdot \alpha_s \cdot (1 - SVF) \quad (2.4)$$

By repeatedly solving Equation (2.1), the total irradiance on the PV module can be calculated for every hour of the year. Irradiance values are then input into the thermal and electrical models to compute the generated electric power.

EFFECT OF THE SKYLINE ON THE SOLAR IRRADIANCE COMPONENTS

The skyline profiles of the urban environment affect the irradiance components in different ways. The calculation of the irradiance components at locations with raised skyline profiles is herein modified according to the following assumptions:

- G_{beam} : the beam component is distributed over the sun disk, yet in the simplified Perez model the sun is assumed to be a point source centred at the sun disk [47]. Therefore, this component is zero when the centre of the sun disk is behind the skyline profile.
- G_{cir} : the circumsolar component is distributed around the sun disk, but in the Perez model it is also reduced to a point source centred at the sun disk. Consequently, this component is zero when the centre of the sun disk is behind the skyline profile.
- G_{hr} : when the objects that constitute the horizon profile are low and very distant from the module, the horizontal ribbon component is only slightly affected. However, if the objects are close to the PoA like in most urban landscapes, the horizontal ribbon effect is assumed to be negligible [48].
- G_{iso} : the diffuse isotropic component is reduced proportionally to the sky view factor.
- G_{refl} : the reflected component is proportional to the global horizontal irradiance which is also affected by the skyline profile (SP). At locations with a raised skyline, the global horizontal irradiance on the ground in front of the module, GHI_{SP} , can be expressed as:

$$GHI_{\text{SP}} = DNI \cdot \sin(a_S) + DHI \cdot \left((1 - F_1) \cdot SVF + F_1 \cdot \frac{a}{b} \right) \quad (2.5)$$

if the sun is in front of the module and above the skyline, or:

$$GHI_{\text{SP}} = DHI \cdot ((1 - F_1) \cdot SVF) \quad (2.6)$$

if the sun is behind the module or blocked by the skyline profile.

SKY VIEW FACTOR CALCULATION

The sky view factor of a differential area element (dA_M) is defined as the view factor from the differential area element to the visible part of the sky, in other words, it is the fraction of radiant flux emitted by the differential area dA_M that is intercepted by the sky. Following the mathematical definition of view factors, the *SVF* is defined as:

$$SVF = \iint_{sky} \frac{\cos(\theta_1)}{\pi} d\Omega \quad (2.7)$$

where θ_1 is the angle between the normal to dA_M and the vector that points to the differential sky area element $d\Omega$.

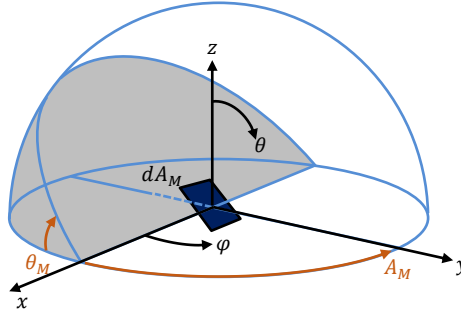


Figure 2.2: Representation of the tilt and orientation of a differential area of a PV module in spherical coordinates. The grey region represents the part of the sky behind the plane of array.

At free-horizon locations, the calculation of the sky view factor is simplified². Its expression can be derived from Equation (2.7) in spherical coordinates for a differential area on a PV module with tilt θ_M and azimuth A_M :

$$SVF = \frac{1}{\pi} \iint_{sky} \begin{bmatrix} \sin(\theta_M) \cos(A_M) \\ \sin(\theta_M) \sin(A_M) \\ \cos(\theta_M) \end{bmatrix}^T \cdot \begin{bmatrix} \sin(\theta) \cos(\varphi) \\ \sin(\theta) \sin(\varphi) \\ \cos(\theta) \end{bmatrix} \cdot \sin(\theta) d\varphi d\theta \quad (2.8)$$

where φ is the azimuth and θ is the zenith angle or colatitude represented in Figure 2.2.

The integration over the spherical wedge that corresponds to the visible part of the sky can be simplified by assuming $A_M = 90^\circ$ and then rotating the differential module area and the ground by 90° around the y axis using the right-hand rule:

$$SVF = \frac{1}{\pi} \int_0^{\frac{\pi}{2}} \int_{\theta_M - \frac{\pi}{2}}^{\frac{\pi}{2}} \left(\begin{bmatrix} 0 & 0 & 1 \\ 0 & 1 & 0 \\ -1 & 0 & 0 \end{bmatrix} \cdot \begin{bmatrix} 0 \\ \sin(\theta_M) \\ \cos(\theta_M) \end{bmatrix} \right)^T \cdot \begin{bmatrix} \sin(\theta) \cos(\varphi) \\ \sin(\theta) \sin(\varphi) \\ \cos(\theta) \end{bmatrix} \cdot \sin(\theta) d\varphi d\theta \quad (2.9)$$

$$SVF = \frac{1}{\pi} \int_0^{\frac{\pi}{2}} \int_{\theta_M - \frac{\pi}{2}}^{\frac{\pi}{2}} \begin{bmatrix} \cos(\theta_M) \\ \sin(\theta_M) \\ 0 \end{bmatrix}^T \cdot \begin{bmatrix} \sin(\theta) \cos(\varphi) \\ \sin(\theta) \sin(\varphi) \\ \cos(\theta) \end{bmatrix} \cdot \sin(\theta) d\varphi d\theta \quad (2.10)$$

²Note that the frequent confusion present in the literature related to the expression of the *SVF* at free-horizon locations [49], [50], stems from a misinterpretation of the its definition.

The integral in Equation (2.10) can be easily solved to obtain the reduced expression of the sky view factor at free-horizon locations:

$$SVF = \frac{1 + \cos(\theta_M)}{2} \quad (2.11)$$

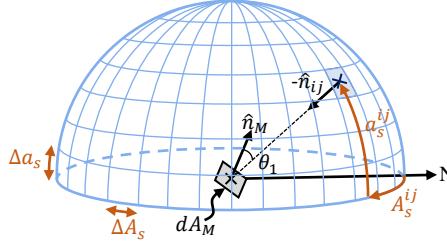


Figure 2.3: Sky view factor calculation. A_s and a_s represent the azimuth and altitude of a sky patch, respectively. The sky view factor to the sky patch ij can be calculated using Equation (2.13)

At raised horizon locations, the sky view factor can be approximated considering an equiangular discretisation of the sky dome illustrated in Figure 2.3, as the sum of the view factors from dA_M to each visible sky patch ij :

$$SVF = \sum_i \sum_j VF_{M \rightarrow ij} \quad (2.12)$$

where the view factors $VF_{M \rightarrow ij}$ can be calculated following the notation in Figure 2.3 as:

$$VF_{M \rightarrow ij} = \frac{\hat{n}_M \cdot \hat{n}_{ij}}{\pi} \cos a_s^{ij} \Delta A_s \Delta a_s \quad (2.13)$$

Sky patches that are behind the skyline profile or below a raised horizon are excluded in the calculation of the SVF . Moreover, only positive view factors are considered in the summation in Equation (2.12). Negative view factors correspond to sky patches that are not visible to the module because they lie behind the plane of array defined by the tilt and orientation of dA_M (i.e., the grey region shown in Figure 2.2).

It should be noted that the sky view factor can be calculated at an infinite number of points on the surface of a PV module. For simplicity, in this chapter a single point at the centre of the PV module is considered. It is assumed that the sky view factor calculated at this point is representative of the entire module.

IRRADIANCE MODEL VALIDATION

In order to evaluate the accuracy of the simplified Perez model with the modification of the irradiance components, the irradiance on the modules of the e-Bike charging station located in Delft (Figure 2.4a) was simulated and compared to measurements. The DNI and DHI inputs for the transposition model were obtained from the CESAR observatory in Cabauw [51], the Netherlands. The skyline profile at the location of this PV system was captured using the Horicatcher tool (Figure 2.4a). Figure 2.4c presents a comparison

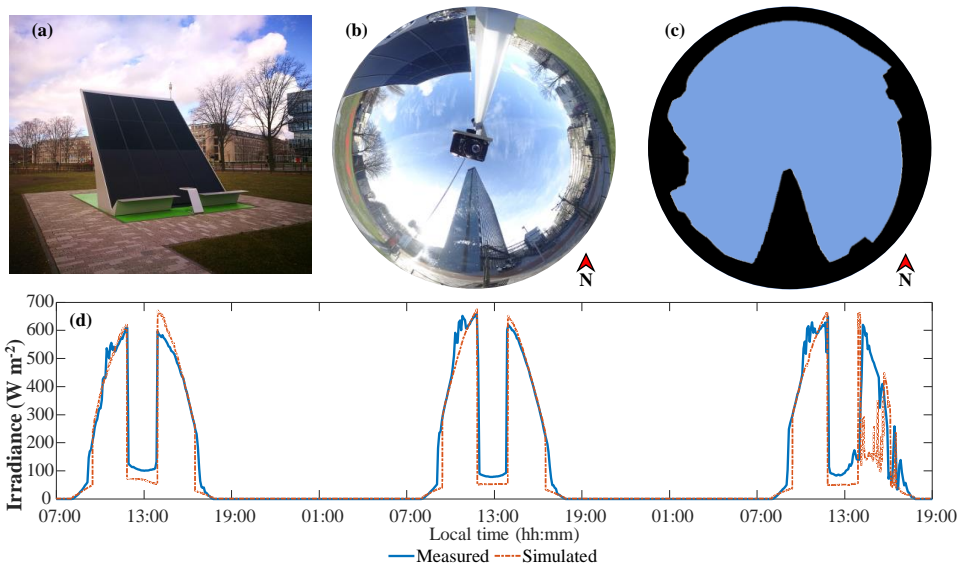


Figure 2.4: Comparison between the measured and simulated PoA irradiance on the e-Bike charging station. (a) Picture of the PV-powered e-Bike charging station in TU Delft campus. (b) Skyline picture captured with the Horicatcher tool next to the solar e-bike charging station. (c) Processed skyline profile after removing the part of the sky blocked by the e-Bike charging station. (d) Measured and simulated plane of array irradiance on the e-Bike charging station.

between the simulated PoA irradiance and measurements taken on the PoA of the e-Bike charging station with a thermopile pyranometer during 3 consecutive days. This specific period of time was selected because the sky was mostly clear, making it possible to employ the *DNI* and *DHI* values measured in Cabauw to estimate the performance of the PV system located in Delft which is 38 km away from the CESAR observatory.

In Figure 2.4c, it can be noticed that both the measured and simulated irradiance drop significantly around noon. The reason is the shading caused by the tall building shown in Figure 2.4a located south of the e-Bike charging station.

Day	Measured (Wh m^{-2})	Simulated (Wh m^{-2})	MBE (%)	RMSE (Wh m^{-2})
2017-02-13	2737	2541	+7.1	68.9
2017-02-14	2931	2598	+11.3	77.0
2017-02-15	2654	1954	+26.4	167.3

Table 2.1: Measured and simulated daily irradiation at the e-Bike charging station. The relative deviation and the root mean squared error (RMSE) are given for comparison.

The measured and simulated daily irradiation are summarised in Table 2.1. The differences between the measurements and the simulations can be attributed to several factors:

1. The simplified Perez model assumes that the beam and the circumsolar components are concentrated in one point at the centre of the sun disk [47]. In reality, these components are distributed on and around the sun disk, and when the sun approaches an obstacle its radiance is gradually reduced before the sun falls completely behind the skyline profile [52]. For the same reasons, in reality the irradiance increases progressively when the Sun starts rising from behind the skyline profile.
2. The point on the ground considered for the calculation of GHI_{SP} is right in front of the PV modules. When the sun is blocked by the tall building, this point on the ground is also shaded and thus Equation (2.6) is used. However, in reality parts of the ground around the module are yet sunlit and the effective GHI_{SP} value is in between the values from Equations 2.5 and 2.6. As a result, when the sun is behind the building, the reflected irradiance on the PoA is underestimated.
3. The irradiance peaks in the morning are due to specular reflections on the windows of one of the surrounding buildings. These peaks cannot be reproduced because transposition models implicitly assume that all reflective surfaces are ideal diffuse (i.e. Lambertian) reflectors.
4. Finally, differences on the afternoon of the 15th of February are due to the differences in cloud cover between Delft, where the sky was mostly clear during the entire day, and Cabauw, where the measured DNI was affected by a stronger presence of clouds.

2.2.2. THERMAL-ELECTRICAL MODEL

After the calculation of the PoA irradiance, the module temperature needs to be determined. In this study, the fluid dynamic model proposed by Fuentes [53] is used to estimate the temperature the module in steady-state conditions. The Fuentes model calculates the module temperature considering the global PoA irradiance, the wind speed, the ambient and ground temperatures, the cloud cover and the mounting of the PV module.

The effective irradiance reaching the solar cell and the cell temperature are inputs to the electrical model that determines the current and voltage generated by the PV module. Even though single- and double-diode models [54] are the most precise approaches for calculating the power output of PV generators, in this chapter the model described in [55] was employed. The advantage of the chosen method lies in its simplicity and the fact that all the required parameters can be easily obtained from commercial PV module datasheets. The PV module efficiency η_M at given irradiance (G_{tot}) and temperature (T_M) is calculated according to [55]:

$$\eta_M = \eta_M^{STC} \cdot (1 + \beta \cdot (T_M - T_M^{STC})) \cdot \left(1 + \ln\left(\frac{G_{tot}}{G_{STC}}\right)\right)^\gamma \quad (2.14)$$

where η_M^{STC} is the efficiency of the module under standard test conditions, β is the module's power temperature coefficient, and γ is given by:

$$\gamma = \frac{N_s \cdot n \cdot k_B \cdot T_M}{q \cdot V_{OC}^{STC}} \quad (2.15)$$

where N_s is the number of series connected PV cells in the module, n the ideality factor of the solar cell that represents different recombination processes [56], k_B the Boltzmann constant, q the elementary charge, and V_{OC}^{STC} the open circuit voltage of the module under STC.

2.3. SIMPLIFIED IRRADIATION MODEL

In order to avoid the repetitive calculations of the time-resolved approach, two indicators to directly estimate the annual irradiation are proposed. In this section these indicators and the mathematical expression of the proposed irradiation model are presented. Furthermore, the model is applied to a specific PV system as an example, and it is shown how to extend the model to estimate the yield of PV systems.

2.3.1. SOLAR IRRADIATION INDICATORS

The annual irradiation on a PV module depends on the local meteorological conditions, which vary from one year to the next one. Thus, climate data is used to estimate the average annual irradiation on a PV system³. From the results of time-resolved simulations using climate data, it was determined that it is possible to approximate the annual irradiation at a given location with two figures of merit that quantify the landscape surrounding a PV module.

The first indicator used to quantify the landscape around a PV module is the already mentioned sky view factor, which can be calculated from the skyline profile as explained in Section 2.2.1. The reason for using this parameter is straightforward. The diffuse isotropic and ground reflected components of the Perez model depend (almost) linearly on the SVF [47].

However, the remaining irradiance components are not directly related to the value of the sky view factor. In fact, it is easy to imagine a case where the beam and circumsolar irradiation components cannot be estimated using the SVF [40]. For example, for a horizontal PV module in the northern hemisphere, all the objects located to the north of the PV module do not overlap with the sun path. These objects reduce the SVF, but they do not affect the beam nor the diffuse circumsolar irradiance components which originate from the centre of the sun disk [46]. Therefore, to estimate the irradiation contribution of to these other two components, a different indicator is proposed: the sun coverage factor. The SCF at a location with a raised horizon is defined as the ratio between the time that the sun is behind the module or blocked by the skyline per year and the annual sunshine duration at the same location with a clear horizon. This can be expressed as:

$$SCF = \frac{\sum_{\text{year}} \chi_{sp}(A_S(t), a_S(t))}{\sum_{\text{year}} \chi_{fh}(a_S(t))} \quad (2.16)$$

where A_S and a_S are the time-dependent solar azimuth and elevation angles respectively, and:

³While weather data describes the atmospheric conditions for a particular year, climate data is obtained by evaluating weather conditions during several years. All the results presented in this chapter were obtained using synthetic typical meteorological year data generated with Meteonorm.

$$\chi_{sp}(A_S, a_S) = \begin{cases} 1 & 0 < a_S \leq a_{sp}(A_S) \\ 0 & \text{otherwise} \end{cases} \quad (2.17)$$

$$\chi_{fh}(a_S) = \begin{cases} 1 & a_S > 0 \\ 0 & \text{otherwise} \end{cases} \quad (2.18)$$

where and a_{sp} is the altitude of the skyline profile as a function of the azimuth angle A :

$$a_{sp}(A), \quad A \in [0^\circ, 360^\circ) \quad (2.19)$$

From its definition, it is evident that the *SCF* is not an irradiance-weighted parameter. This implies that blocking the sun one hour in the early morning contributes to reducing the *SCF* in the same amount as blocking the sun one hour at noon. In some cases, this simplification can result in a weak correlation with hourly irradiance values. However, as shown in the following sections, the *SCF* demonstrates a strong correlation with the annual irradiation while it can be rapidly calculated solely from the skyline profile and annual sun path.

2.3.2. SKYLINE PROFILES

Ideally, a detailed 3D model of the objects surrounding the PV modules is required for an accurate calculation of the yield of a PV system in a complex urban environment. A full 3D description of the scene enables the accurate calculation of the irradiance on the surfaces surrounding the PV modules by individually distinguishing their position, orientation and reflective properties. In turn, this allows for an accurate calculation of the reflected irradiance on the PV modules.

Synthetic skyline profile functions	
$a_{sp0} = 0^\circ$	
$a_{spAn} = 9^\circ \cdot n$	$a_{spIn} = 5^\circ + \frac{9^\circ \cdot n - 5^\circ}{360^\circ} \cdot A$
$a_{spBn} = 9^\circ \cdot n \cdot \sum_{i=1}^2 \Pi \left(\frac{A - 180^\circ \cdot i + 90^\circ}{90^\circ} \right)$	$a_{spJn} = a_{spIn} ((A - 90^\circ) \bmod 360^\circ)$
$a_{spCn} = 9^\circ \cdot n \cdot \sum_{i=1}^3 \Pi \left(\frac{A - 120^\circ \cdot i + 60^\circ}{90^\circ} \right)$	$a_{spKn} = a_{spIn} ((A - 180^\circ) \bmod 360^\circ)$
$a_{spDn} = 9^\circ \cdot n \cdot \sum_{i=1}^4 \Pi \left(\frac{A - 90^\circ \cdot i + 45^\circ}{60^\circ} \right)$	$a_{spLn} = a_{spIn} ((A - 270^\circ) \bmod 360^\circ)$
$a_{spEn} = 9^\circ \cdot n - \frac{9^\circ \cdot n - 5^\circ}{360^\circ} \cdot A$	$a_{spMn} = 5^\circ + \frac{ A - 180^\circ }{20^\circ} \cdot n$
$a_{spFn} = a_{spEn} ((A - 90^\circ) \bmod 360^\circ)$	$a_{spNn} = a_{spMn} ((A - 90^\circ) \bmod 360^\circ)$
$a_{spGn} = a_{spEn} ((A - 180^\circ) \bmod 360^\circ)$	$a_{spOn} = a_{spMn} ((A - 180^\circ) \bmod 360^\circ)$
$a_{spHn} = a_{spEn} ((A - 270^\circ) \bmod 360^\circ)$	$a_{spPn} = a_{spMn} ((A - 270^\circ) \bmod 360^\circ)$

Table 2.2: Synthetic skyline profile functions used to generate the regression coefficients for the annual irradiation and DC yield models. In the functions, A is the azimuth angle, mod is the modulo operation, Π is the rectangle function and $n \in \{1, 2, 3, 4, 5, 6, 7, 8, 9, 10\}$.

Nonetheless, transpositions models approximate the 3D scene by using the skyline profile to compute the irradiation on the PV modules. The skyline profile is a 2D projection of the surrounding landscape as seen from the point of interest on the surface of

the PV module. The simplification of the surrounding geometry introduces errors in the calculations which are considered acceptable at the level of detail discussed this chapter.

Synthetic skyline profiles were used to find the correlations between the indicators and the annual irradiation. Each synthetic profile consists of a number of geometrical shapes distributed along the horizon line. The advantage of using synthetic skylines lies in the fact that the skyline shapes can be modified at will, so as to mimic a wide range of different real urban landscapes. The 161 synthetic skyline profiles employed in this work are listed in Table 2.2. Figure 2.5 shows some examples of the synthetic profiles used to obtain the results presented in the following sections.

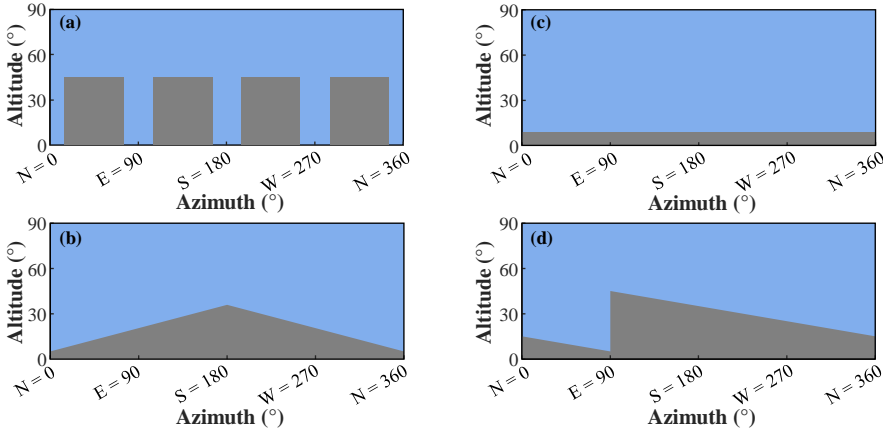


Figure 2.5: Examples of synthetic skyline profiles: (a)–(d) Synthetic skyline profiles. These synthetic skylines respectively correspond to the functions a_{spD5} , a_{spO4} , a_{spA1} and a_{spE5} listed in Table 2.2

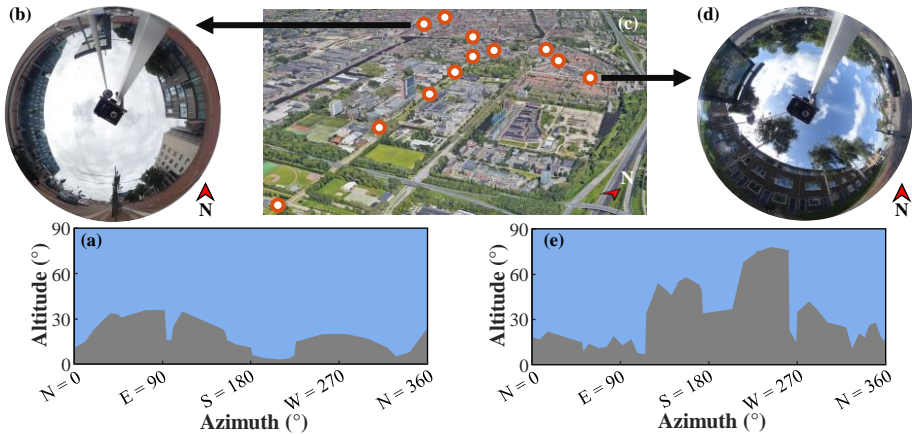


Figure 2.6: Real skyline profiles: (a)–(e) Skylines of the city of Delft, the Netherlands. (c) Locations in Delft where the real skyline profiles were captured. (b),(d) Examples of the images obtained with the Horicatcher tool at two different locations. (a),(e) Post-processed skyline profiles of the Horicatcher images.

Additionally, the skyline profiles of 12 real locations in Delft were captured using the Horicatcher tool [57] and post-processed to generate skyline profile functions. These real skyline profiles were included in the simulations as control points to ensure that the synthetic skyline profiles are representative of actual urban landscapes. The locations in Delft where the skyline profiles were captured, as well as the images taken with the Horicatcher tool and the post-process skyline profiles are presented in Figure 2.6.

2.3.3. SIMPLIFIED IRRADIATION MODEL

The irradiance on tilted surfaces was simulated considering each synthetic and real skyline profile to demonstrate how the annual irradiation components correlate with SVF and SCF . As an example, the correlation coefficients calculated for the PV-powered e-Bike charging station are given in Figure 2.7 for the case when the PV modules are tilted 51° and facing southwest.

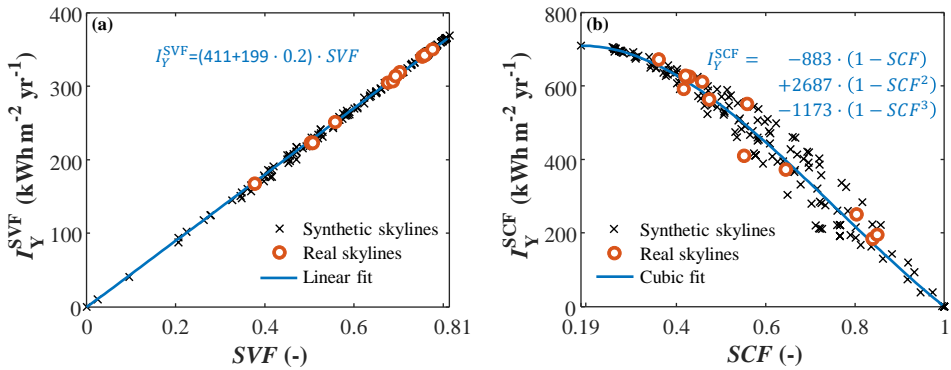


Figure 2.7: Example of the correlation between SVF , SCF and the irradiation components for the southwest-facing e-Bike charging station tilted 51° in Delft, the Netherlands. (a) Correlation between SVF and the diffuse isotropic plus albedo irradiation. (b) Correlation between SCF and the beam plus circumsolar irradiation. Crosses and circles correspond to simulations with synthetic and real skyline profiles, respectively. The solid lines and the equations correspond to the polynomial regressions that best fits the results

In Figure 2.7a, the sum of the simulated isotropic diffuse and albedo components (I_Y^{SVF}) is plotted against the sky view factor of the corresponding skyline profiles. The maximum SVF value on the horizontal axis equals 0.81 which corresponds to the sky view factor of a module tilted 51° in a free horizon location. The correlation is highly linear because the diffuse isotropic component, which depends linearly on SVF , is generally much larger than the albedo component. Deviations from the linear fit are due to quadratic relation between albedo component and the SVF when the beam component is blocked as expressed in Equations 2.4 and 2.6.

In Figure 2.7b, the sum of the simulated beam and circumsolar components (I_Y^{SCF}) is correlated with the sun coverage factor. From the minimum value in the horizontal axis, it can be noticed that even when the horizon is free, the sun is behind the PoA 19% of the time because the PV modules are tilted 51° . Besides, it can be observed that the annual irradiation drops faster as SCF increases. This can be explained by realising that small SCF values usually correspond to low skyline profiles that block the sun mostly during

sunrise and/or sunset, when the PoA irradiance is much lower than at midday.

The total annual irradiation on a given surface (I_Y) can be expressed as:

$$I_Y = I_Y^{SCF} + I_Y^{SVF} \quad (2.20)$$

and I_Y^{SVF} and I_Y^{SCF} can be approximated with polynomial regressions:

$$I_Y^{SCF} = \sum_{k=1}^3 c_k \cdot (1 - SCF^k) \quad (2.21)$$

$$I_Y^{SVF} = (c_4 + c_5 \cdot \alpha_s) \cdot SVF \quad (2.22)$$

The coefficients c_1, \dots, c_5 are obtained from the linear and cubic fittings shown in Figure 2.7 and are valid for a specific module tilt and orientation within a climatic region. Furthermore, the ground albedo (α_s) can be modified in Equation (2.22) to match the local albedo.

There are two limit cases regarding the skyline profile that are worth mentioning. When the sky view is completely obstructed SVF is 0 and SCF is 1. Under these conditions, the estimated annual irradiation is always zero. On the other hand, when the horizon is free, the maximum irradiation for a horizontal surface is given by:

$$I_{Y(max)} = \sum_{k=1}^4 c_k \quad (2.23)$$

Table 2.3 presents the coefficients used for estimating the annual irradiation on the e-Bike charging station for different module orientations in Delft. To explain the use of these coefficients, consider the case of a south-facing PV system tilted 51° in a free horizon location in Delft. It can be quickly determined from the sun path that $SCF = 0.115$ and $SVF = 0.814$. Assuming that the albedo of the bricks around the PV system in Figure 2.7a is 0.2, the coefficients corresponding to a south-oriented surface in Table 2.3 can be substituted in Equations 2.21 and 2.22 to calculate the annual irradiation, which yields 1082 kWh m^{-2} .

A_M	c_1	c_2	c_3	c_4	c_5
N = 0	-1147	1875	-801	411	144
NE = 45	-6353	9105	-3863	411	148
E = 90	-2261	4344	-1903	411	174
SE = 135	-895	2708	-1174	411	202
S = 180	-665	2553	-1143	411	211
SW = 225	-883	2687	-1173	411	199
W = 270	-2025	3980	-1747	411	174
NW = 315	-5960	8526	-3613	411	145

Table 2.3: Correlation coefficients for a 51° tilted surface in Delft, the Netherlands. The coefficients (expressed in kWh yr^{-1}) were calculated for eight main PV module orientations.

2.3.4. SIMPLIFIED ENERGY YIELD MODEL

The average operative efficiency of the PV modules can be employed to estimate the annual DC yield of a PV system from the annual irradiation on its PV modules. The operative efficiency is defined as the actual conversion efficiency from solar irradiance to electric power of a PV module in the field and it depends on the irradiance and the module temperature among other factors. Operative efficiencies are typically lower than standard test conditions (STC) efficiencies, since the module operating temperature is usually higher than 25 °C. Despite the fact that the ambient temperature and the solar irradiance, which affect the operative efficiency, vary significantly from month to month, relative variations in the monthly performance ratios of a PV system are generally lower than 10 % [58]. This suggests that the proposed irradiation model can be extended to estimate the annual DC energy yield E_Y of a PV module resulting in:

$$E_Y = E_Y^{SCF} + E_Y^{SVF} \quad (2.24)$$

where:

$$E_Y^{SCF} = \sum_{k=1}^3 d_k \cdot (1 - SCF^k) \quad (2.25)$$

$$E_Y^{SVF} = (d_4 + d_5 \cdot \alpha_{\text{gnd}}) \cdot SVF \quad (2.26)$$

The usefulness of a fast energy yield estimation model is self-evident. If correlation coefficients for a specific PV system are calculated, for example, the e-Bike charging station, it is possible to estimate how much electricity the system would generate at different locations in an urban environment. Then, it would be possible to use the digital elevation model of urban areas to create energy potential maps and find all the places where it is energetically and financially sound to install a certain PV system.

2.4. BENCHMARKING AND VALIDATION

2.4.1. BENCHMARK STUDY IN DIFFERENT CLIMATES

The estimations of the irradiation model were evaluated using synthetic skyline profiles in cloudy and sunny climates by comparing results with the time-resolved irradiance simulation approach. The annual irradiation on surfaces with different tilt angles (0°, 45° and 90°) was simulated by applying the time-resolved approach in two cities with different climates: Delft, the Netherlands, where the annual global horizontal irradiation is approximately 1 MWhm⁻² and the mean annual cloud cover⁴ is 5.5 okta; and Antofagasta in the Atacama Desert, Chile, with an annual irradiation close to 2 MWhm⁻² and 3.4 okta average cloud cover.

The regression coefficients for the annual irradiation model were generated from the time-resolved simulation results. Then, the annual irradiation for each synthetic skyline profile was estimated using the proposed model and compared to the original results of the time-resolved simulation. Figure 2.8 shows the deviations between the results. The high values of the coefficient of determination ($R > 0.97$ for all cases) show a good

⁴The cloud cover is a good indicator of the proportion of diffuse and beam solar radiation in a certain region.

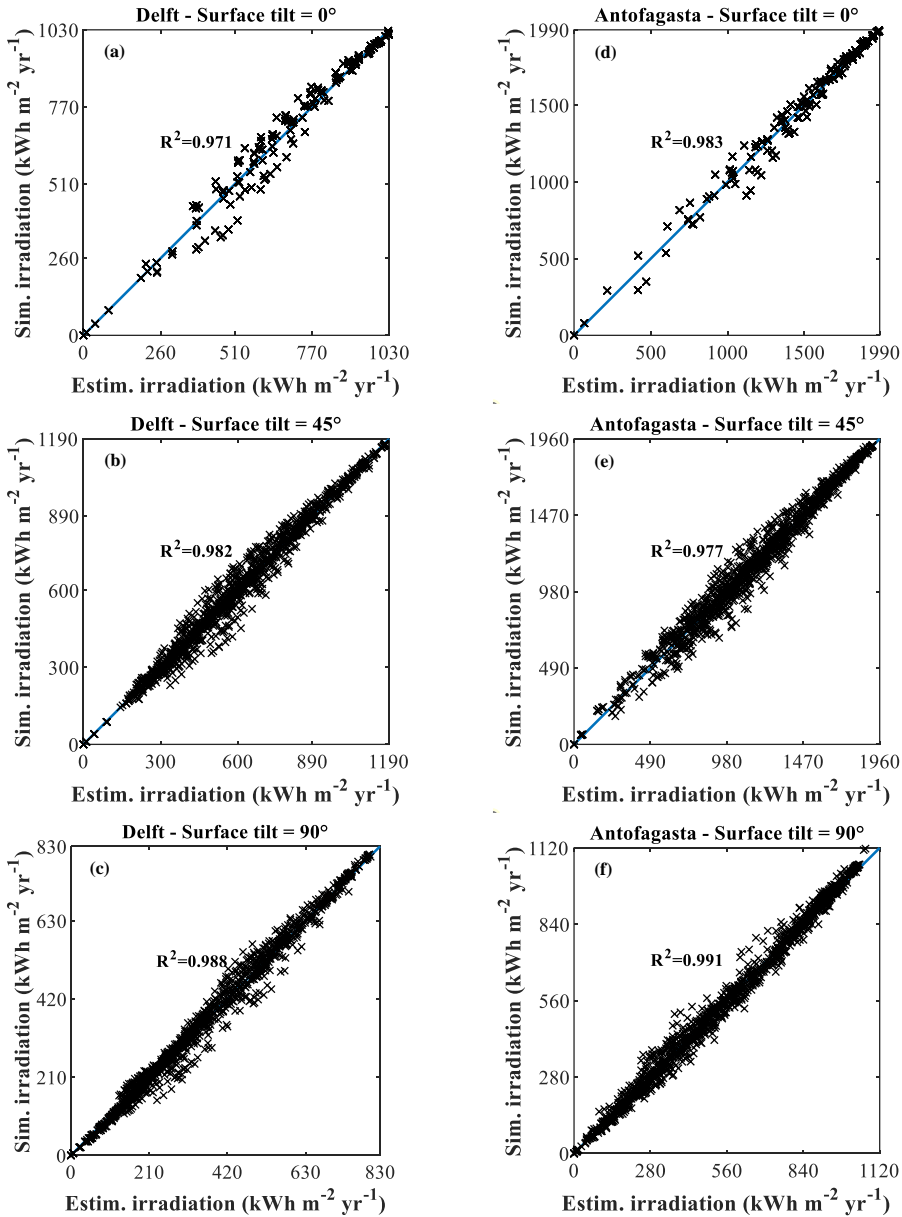


Figure 2.8: Benchmark of the proposed annual irradiation model by comparison with the results of time-resolved simulations in Delft and Antofagasta for different module tilt angles and orientations. For surfaces tilted 45° and 90°, the comparison was carried with 161 synthetic skylines and eight possible module orientations. For horizontal surfaces (0° tilt), only 161 results are shown because the orientation of the surface is irrelevant.

performance of the proposed model in both locations. Moreover, from the analysis of the results it was determined that in 85 % of the simulations the relative deviations from the estimations are lower than 10 %, and the largest relative deviations correspond to surfaces with low solar energy potential, which are also the least attractive ones for installing PV.

2

COMPUTATION TIME

The proposed irradiation model implies a significant improvement in terms of computational cost with respect to the time-resolved approach. The computation time of both approaches was compared using serial implementations of the respective algorithms in MATLAB on a computer with a dual-core Intel Core i7-5500U processor. In average, each simulation to calculate the annual irradiation took 260 ms using the time-resolved approach and 14 ms using the proposed model.

It is important to emphasise that the computation time and the extent to which it can be reduced strongly depend on how the algorithms are implemented and the specific platform used for their execution. For example, both the time-resolved approach and the proposed simplified irradiation approach present a high degree of parallelism, which would help to significantly reduce the computation times.

The proposed approach is particularly relevant in the context of Geographic Information Systems (GIS) and in the prospecting stages of a project, where it can facilitate conducting solar energy potential assessment studies with existing GIS software over large-scale urban areas by combining the proposed model with different methods for obtaining the skyline from three-dimensional urban point clouds [59], [60]. For example, considering the above-mentioned simulation times, the calculation of the potential of a given PV system over a cadastre of 100 hectares with 1 m resolution using the time-resolved approach would take approximately 3 days while with the proposed model it could be done in less than 4 hours.

2.4.2. VALIDATION STUDY IN THE NETHERLANDS

The annual energy yield model was applied to estimate the yield of multiple PV systems monitored by [Solar Monkey](#) in the Netherlands. Ten grid-connected PV systems with the same tilt ($\theta_M = 35^\circ$), PV modules (JA Solar JAM6-60-270BK) and inverters (SolarEdge SE3500) were studied. The coefficients of the annual DC yield model were calculated using climate data and the results were compared to the actual energy yield measured between the years 2016 and 2017.

The coefficients for estimating the annual DC yield of the PV modules are presented in Table 2.4. It is important to notice, that these coefficients are only valid for a particular PV module model with a specific tilt angle. This limitation is a consequence of extending the irradiation model to calculate the DC energy yield.

For every PV system, the irradiance indicators were calculated at the central point of the PV array using skylines profiles generated from a LIDAR digital elevation model [61]. With these values, the coefficients given in Table 2.4, and assuming an average albedo of 0.2, the annual DC yield of the systems can be calculated. However, as only AC yields were available for the monitored PV systems, it was necessary to estimate the AC yield of the PV systems from the DC yield of the PV modules. The AC yield was calculated

A_M	d_1	d_2	d_3	d_4	d_5
N = 0°	-249	467	-186	106	21
NE = 45°	-536	964	-421	106	21
E = 90°	-319	746	-315	106	23
SE = 135°	-187	630	-262	106	25
S = 180°	-160	648	-283	106	26
SW = 225°	-193	648	-274	106	25
W = 270°	-311	736	-314	106	23
NW = 315°	-506	913	-397	106	21

Table 2.4: Model coefficients (expressed in kWh yr⁻¹) for estimating the DC yield of a JA Solar JAM6-60-270BK PV module tilted 35° in the southern part of the Netherlands.

taking into account the European efficiency of the SE3500 solar inverter (97.6 %), and the following system losses [62]: MPPT losses (accounting for 1 % absolute efficiency loss at system level); module mismatch losses (1 % absolute), ohmic losses (3 % absolute); availability of the system (1 % absolute); and soiling losses (1 % absolute). All factors taken into account, the resulting DC to AC conversion efficiency was 90.6 %.

Location	Size (kWp)	Azimuth (°)	SVF (-)	SCF (-)	Meas. yield (MWh yr ⁻¹)	Estim. yield (MWh yr ⁻¹)	Error (%)
U. Heuvelrug	4.86	11 (ESE)	0.76	0.38	4.22	4.01	-5.0
Culemborg	5.94	95 (E)	0.83	0.45	4.95	4.47	-9.8
Son en Breugel	7.29	161 (SSE)	0.86	0.29	6.63	6.81	2.7
Son en Breugel	2.70	171 (S)	0.78	0.15	2.65	2.71	2.3
Eindhoven	2.70	262 (W)	0.90	0.29	2.6	2.72	4.6
Eindhoven	3.51	91 (E)	0.89	0.44	2.27	2.16	-4.8
Laarbeek	11.07	228 (SW)	0.84	0.37	9.14	9.80	7.2
Gemert-Bakel	6.48	178 (S)	0.81	0.20	6.43	6.52	1.4
Venlo	3.24	231 (SW)	0.88	0.32	2.86	2.99	4.5
Emmen	5.94	231 (SW)	0.84	0.28	5.21	5.46	4.8

Table 2.5: Model validation in the Netherlands using 10 PV systems monitored during an entire year (2016-2017). All the systems studied are tilted 35° and built with the same type of PV modules and inverters. The error between the measured AC yield and the estimated annual AC yield is given in the last column.

In Table 2.5 the characteristics and results of the analysed PV systems are presented. From the comparison between the measured and estimated AC yields, the average estimation error was 0.7 %, with the maximum error corresponding to the PV system installed in Culemborg (underestimated by 9.8 %). The energy yield of PV systems up to 5 kWp was estimated with higher accuracy, with the largest deviation being 4 % for the system in Venlo. On the other hand, the yield of large systems was slightly overestimated. This overestimation is most likely due to larger variations in the irradiation received by the PV modules, i.e., in a larger system it is more probable that some modules are more

shaded than others. In order to improve the estimation for large systems, the *SVF* and *SCF* values could be calculated at different points in the array.

2.4.3. VALIDATION STUDY IN DIFFERENT CLIMATES

The model performance was also evaluated in different climates using PV systems from the *PVOutput* online database [63]. *PVOutput* is a free online service that allows users to configure their PV systems to automatically upload live monitored data.

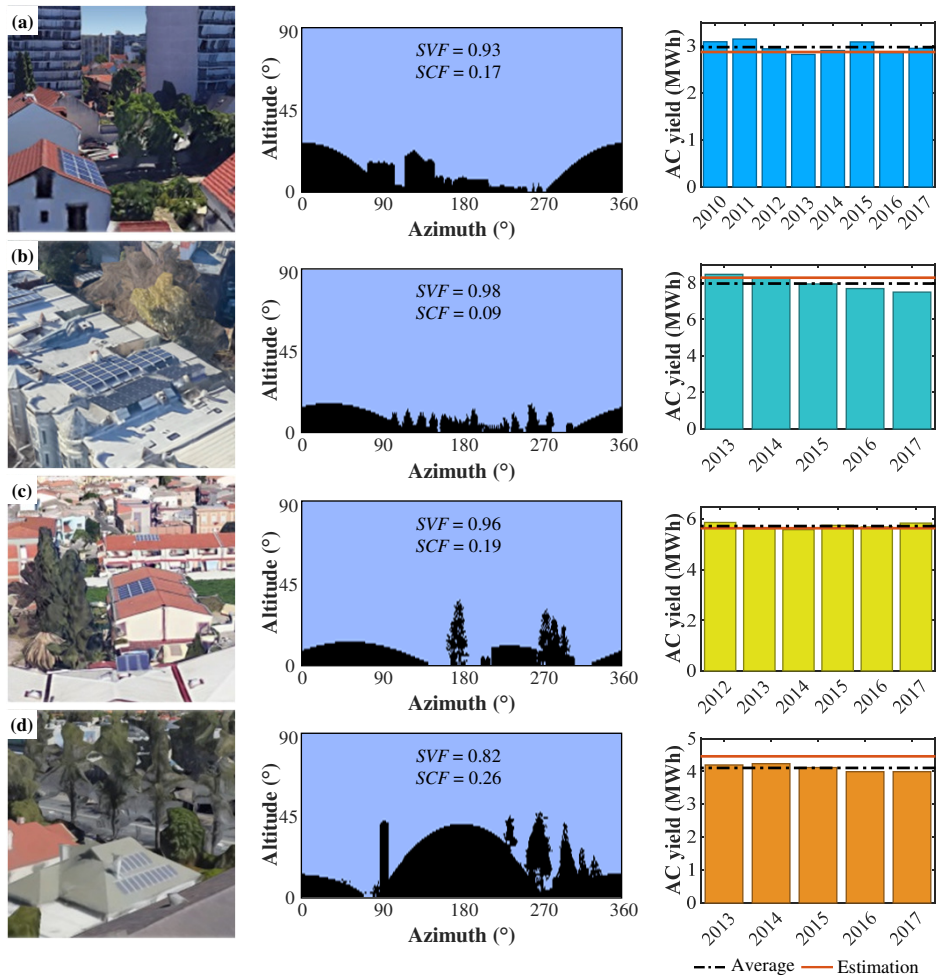


Figure 2.9: Model validation with PV systems from *PVOutput*. From left to right: image of the PV system, reconstructed skyline profile and AC yield. In the bar plots, the bars represent measured values, the dashed lines represent the average of the bars and the red solid line is the estimation of the proposed model. (a) PV system in Paris, France. (b) PV systems in Washington, U.S.A. (c) PV system in Cagliari, Italy. (d) PV system in Adelaide, Australia.

The four systems shown in Figure 2.9 were selected according to the following re-

quirements:

- Monitoring time must be larger than 5 years.
- Data loss for any year must be lower than 1 %.
- The generated electrical energy must be consistent through time.
- The PV system must be visible on Google Earth.
- Photogrammetry data must be available to reconstruct the skyline profile.
- The PV module and inverter models must be identified.

The correlation coefficients for each of these systems were generated using climate data generated with Meteonorm. The bar plots in Figure 2.9 show again a good agreement between the estimated and measured yields. The largest deviation corresponds to the system in Adelaide, which on average generated 7.9 % less energy than the estimated by the proposed model. The AC yield bar graph corresponding to the system in Adelaide shows a clear decreasing trend in time. This drop was partly due to changes the annual irradiation, which decreased approximately 4 % from the year 2013 to the year 2017 [64], but it could also be associated with the degradation of PV modules performance which is not considered in the annual energy yield model.

The presented benchmarking and validation studies suggest that the estimation error of the proposed approach is lower than 10 %. It should be noted that such uncertainty level might not acceptable for all kind of applications or phases of development of a PV project. For example, significantly lower errors [65], [66] are expected to ensure the profitability of commercial and utility scale PV projects.

Therefore, it is important to emphasise that the proposed approach is particularly suitable for evaluating the best locations to install a PV system with a given orientation in large geographical areas. Moreover, it can also be valuable to improve current solar-based urban planning design methods which take into account the solar potential of a building as a design parameter [67]–[69]. For instance, the application of the proposed irradiation model could facilitate finding the optimum shape and distribution of buildings in a cadastre to maximise the combined solar energy potential of the entire group of buildings.

2.5. CONCLUSIONS

In this chapter, a simplified model to estimate the annual irradiation and yield of PV systems was presented. The model is specially advantageous when exploring the energy potential of a PV system in a large number of locations, and hence it is particularly useful for evaluating the best locations to install PV systems in urban environments.

The presented model is based on two indicators: the sky view factor and the sun coverage factor, and it requires the generation of five correlation coefficients that depend on the local climate. These coefficients are generated one time, and later used to directly predict the irradiation and yield of a PV system in any place within a region with a similar

climate. At each new site, the *SVF* and the *SCF* of the PV module must be determined, and using the corresponding correlation coefficients the annual irradiation and yield can be quickly calculated.

The main novelty in the irradiation model is the introduction of the sun coverage factor to estimate the beam and circumsolar irradiation. The *SCF*, can be easily calculated knowing the sun path and the shape of the skyline profile. However, since the *SCF* is not an irradiance-weighted parameter, higher deviations are obtained on surfaces with a low solar potential, which are the least interesting for PV applications after all. The outcomes of the presented benchmarking and validation studies suggest that the estimation error of the proposed model is below 10 %.

Moreover, the irradiation model entails a significant reduction in the computational requirements for calculating the yield of PV systems in complex urban environments in comparison to time-resolved approaches. This improvement allows to quickly transform digital elevation models into detailed solar energy potential maps which can help architects, engineers and urban planners to build more sustainable cities.

3

DETAILED IRRADIANCE MODELLING IN COMPLEX SCENARIOS

This chapter is based on the following publication:

A. Calcabrini, R. Cardose, D. Gribnau, B. Pavel, P. Manganiello, M. Zeman, O. Isabella, *Time-varying, ray tracing irradiance simulation approach for photovoltaic systems in complex scenarios with decoupled geometry, optical properties and illumination conditions*, Progress in Photovoltaics **31**, 134 (2023).

3.1. INTRODUCTION

The developments in the photovoltaic (PV) field over the last decades have fostered the deployment of PV modules from utility-scale power plants to buildings [15], [25] to vehicles [70], [71]. As a result, many PV systems are installed in landscapes with complex geometries where PV modules are often subject to partial shading. To add to this, partially shaded PV systems will become increasingly common since the integration of PV in the urban environment will be of utmost importance for the development of net-zero-energy districts and the achievement of the UN Sustainable Development Goals [72]. In this context, accurate simulation models will become increasingly important to improve the calculation the irradiance incident on the solar cells and, subsequently, the electrical power generated by a PV system.

While Chapter 2 focused on finding the best locations to install PV in urban environments, this chapter examines in detail the characteristics of the solar radiation at a given location. In this chapter a backward ray tracing model is proposed to compute the irradiance on PV modules in scenarios with arbitrarily oriented diffuse and specular surfaces.

The main novelty in this approach is that it decouples ray tracing calculations from illumination conditions and from the optical properties of the materials in the scene. As a consequence, it enables the simulation of surfaces with time-varying optical properties and the performance spectrally-resolved irradiance simulations.

3.2. IRRADIANCE MODELS

The selection of an adequate irradiance simulation model for a specific application depends mainly on the size of the PV system and the complexity of the landscape surrounding the installation. Since the required computing power and computation time increase with the accuracy of the models, there is not a single model that is most appropriate for every application.

The most common irradiance simulation models for PV applications can be classified in three main groups summarised in Table 3.1: transposition models, view factor models and ray tracing models.

Simple transposition	Beam component		$DNI \cdot \cos(AOI)$
	Diffuse component		[47], [73]–[75]
	Reflected component		[73], [76]
View factor (VF)	2D VF		[77]–[79]
	3D VF		[80]–[83]
Ray tracing (RT)	Direct method	Forward RT	[84], [85]
		Backward RT	[86], [87]
	Daylight coefficients	Forward RT	[88], [89]
		Backward RT	[90]–[92]

Table 3.1: Main irradiance simulation approaches and models used in the PV field to calculate the plane of array irradiance and some of the most relevant contributions.

Transposition models, already introduced in Section 2.2, calculate the irradiance incident on a PV module by adding the contributions of the beam, diffuse and ground reflected sunlight components on the plane of array (PoA). The diffuse component can be determined using one of several sky diffuse models that make different levels of approximations to describe the radiance distribution over the sky dome [47], [73], [74]. Transposition models are the simplest and fastest approach to calculate the PoA irradiance. For example, the irradiance impinging on each cell of a 72-cell PV module can be simulated with 1-minute resolution for an entire year using the simplified Perez diffuse sky model [47] in few seconds with a modern personal computer. The main limitation of transposition models is the low accuracy in the calculation of the diffuse and reflected irradiance components. In a simple landscape, the expected simulation error is typically below 10% [93]. However, errors can increase to about 15% when the PV module is not optimally oriented [94], [95]. Further limitations of these models are the underlying assumptions that the ground is uniformly illuminated and its reflectivity is constant [76]. As a result, transposition models are mostly used to simulate the irradiance on monofacial PV modules in relatively open landscapes such as large PV power plants or on rooftop PV systems in areas with low building density.

View factor models calculate the ground reflected irradiance component by computing the view factors from the PV module to the shaded and unshaded areas on the ground. This refinement in the calculations makes view factor models suitable for simulating the irradiance on the rear side of modules in bifacial PV power plants. In addition, view factor models can be classified in two main types. The first type, usually referred to as 2D view factor models, assumes that rows of modules are infinitely long to simplify the calculation of view factors [79]. 2D view factor models have been implemented in commercial software packages [77] and errors lower than 16% were reported in the calculation of the rear side irradiance [78]. The second type of view factor models, usually referred to as 3D view factor models [80]–[83], considers that rows of PV modules are finite in length, which allows the inclusion of edge effects in the simulations. Experimental studies reported errors that range from 5% to 15% in the rear side irradiance calculation [96], [97]. 3D view factor models are also quite fast because the view factors are computed with closed-form formulas [98]. However, these formulas are not directly applicable in geometrically complex scenarios with non-horizontal surfaces, such as urban environments. In these cases, the estimation of view factors can be achieved by means of the ray casting method [99].

Ray tracing (RT) are the most general irradiance simulation models and enable the simulation of surfaces with arbitrary orientations and bidirectional scattering distribution functions (*BSDF*) [100]. RT algorithms are classified into two main types. Forward RT (FRT) algorithms calculate the irradiance on the PV module by tracing rays from the light sources (i.e., the sun and the sky dome) to the PV module and its surroundings [84], [88]. Frequently, FRT is not computationally efficient for simulating light propagation at system-scale because most of the traced rays do not contribute to the irradiance on the PV module. In contrast, backward RT (BRT) algorithms calculate the irradiance on the PV module by following the path of rays from the PV module to the light sources, which significantly reduces the number of rays needed to compute the incident irradiance. In practice, BRT is mainly employed to solve the irradiance incident on the front (or back) surface of a PV module and FRT is typically used in combination the transfer matrix method to solve the reflection and absorption in the internal layers of the PV module and the solar cells [101]–[104]. The software suite *Radiance* [105] is the most widely adopted backward ray tracer in the field of photovoltaics [86], [87], [89], [92], [106].

In order to alleviate the computational time, RT can be employed to calculate daylight coefficients [107], which are defined as the ratio between the irradiance incident on a target surface to the radiance emitted by a specific sky sector. Daylight coefficients are calculated to decouple the illumination conditions from the ray tracing solution of a specific geometry [108]. RT models provide a practical method to calculate daylight coefficients and to generate sensitivity maps [88] or daylight coefficient matrices [92]. These maps or matrices can be multiplied by the sky radiance distribution to calculate the irradiance on the solar cells under different sky conditions without repeating the ray tracing simulations.

Two main desirable features for irradiance models, that are not readily available in current ray tracing models, are the ability to perform spectrally-resolved simulations and to simulate surfaces with time-varying optical properties. Spectrally-resolved irradiance simulations are important for bifacial PV systems [109]–[111] and will be essential in the

near future to simulate the yield of tandem PV modules [112], [113]. Meanwhile, the ability to simulate time-varying optical properties can be useful to model the effects of rain and snow on the surface reflectivity [114] and improve the calculation of the bifacial energy gain in large PV power plants [115]. Whereas the implementation of these features in transposition and view factor models is rather simple, adding these simulation capabilities to existing RT models entails a heavy computational burden. Since daylight coefficients depend on the wavelength-specific optical properties of the surfaces composing the scene, ray tracing simulations need be repeated to calculate daylight coefficients at every wavelength and for every possible combination of optical properties.

3

3.3. BASIC RADIOMETRIC CONCEPTS

In order to explain the proposed simulation approach, first it is necessary to revisit and refine the definition of some basic radiometric concepts introduced in Chapter 1.

The irradiance G on a differential area element of a solar cell dA_c is generally defined as the total incident radiant flux $d\Phi$ per unit area. When neglecting the radiant flux transmitted through translucent materials, G can be divided into three basic components depicted in Figure 3.1: (1) the beam irradiance (G_{beam}) due to the radiant flux coming from the sun disk; (2) the diffuse irradiance (G_{diff}) due to the radiant flux coming directly from the sky dome; and (3) the reflected irradiance (G_{refl}) due to the radiant flux that bounces on the surface of objects in the scene before reaching the solar cell¹:

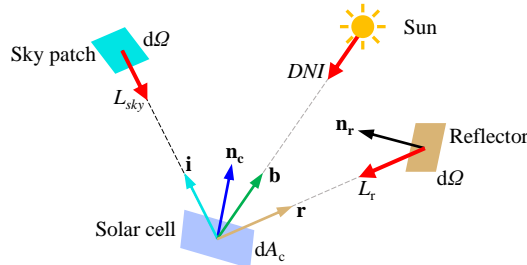


Figure 3.1: Irradiance components incident on a differential area of a solar cell dA_c . The beam component originates in the sun, the diffuse component emanates from the sky dome and the reflected component comes from surfaces around the solar cell.

$$G_{\text{tot}} = \frac{d\Phi}{dA_c} = G_{\text{beam}} + G_{\text{diff}} + G_{\text{refl}} \quad (3.1)$$

Assuming that the sun is a point source, the beam irradiance can be calculated using Equation (3.2) from the direct normal irradiance (DNI), and the scalar product of the normal vector to the solar cell \mathbf{n}_c and the vector that points from the centre of the solar cell to the centre of the solar disk \mathbf{b} :

$$G_{\text{beam}} = DNI (\mathbf{b} \cdot \mathbf{n}_c) \quad (3.2)$$

¹All the vectors in the equations of this article are unitary vectors.

The diffuse irradiance can be determined by integrating the sky radiance L_{sky} incident from direction \mathbf{i} over the visible part of the sky Ω_V :

$$G_{\text{diff}} = \int_{\Omega_V} L_{\text{sky}}(\mathbf{i}) (\mathbf{i} \cdot \mathbf{n}_c) d\Omega = \pi \int_{\Omega_V} L_{\text{sky}}(\mathbf{i}) dF_{c \rightarrow s} \quad (3.3)$$

where $d\Omega$ is the solid angle of a differential sky sector (i.e., sky patch). The second integral in Equation (3.3) is expressed in terms of the view factor from the differential area of the solar cell to a differential area element of the sky, which is defined as:

$$dF_{c \rightarrow s} = \frac{1}{\pi} (\mathbf{i} \cdot \mathbf{n}_c) d\Omega \quad (3.4)$$

Likewise, the reflected irradiance can be calculated by integrating the reflected radiance L_r incident from direction \mathbf{r} over the spacial region around the solar cell that projects onto reflective surfaces Ω_B :

$$G_{\text{refl}} = \int_{\Omega_B} L_r(\mathbf{r}) (\mathbf{r} \cdot \mathbf{n}_c) d\Omega \quad (3.5)$$

The reflected radiance L_r is determined by the radiance incident on the reflector and its optical properties described by the Bidirectional Reflectance Distribution Function (*BRDF*). The *BRDF* of an opaque reflective surface with normal \mathbf{n}_r , is defined as the ratio between the outgoing radiance dL_r in direction \mathbf{r} to the radiance incident L_i from direction \mathbf{i} :

$$L_r(\mathbf{r}) = \int_{\Omega_H} dL_r(\mathbf{r}) = \int_{\Omega_H} BRDF(\mathbf{i}, \mathbf{r}) L_i(\mathbf{i}) (\mathbf{i} \cdot \mathbf{n}_r) d\Omega \quad (3.6)$$

where Ω_H is the hemisphere in front of the reflective surface.

It must be noted that the incident radiance on each reflector L_i depends on higher order reflections. Since the radiance incident on the reflector (L_i) must be the emitted or reflected radiance at a point on another surface, L_r is defined in terms of itself [116]. Therefore, practical methods, such as ray tracing, are needed to limit the recursivity of the problem and approximate the reflected irradiance on a solar cell.

3.4. THE PROPOSED SIMULATION APPROACH

The irradiance simulation approach described in this section is based on a deterministic backward ray tracer limited to two ray bounces, which enables the simulation of Lambertian and specular reflectors. The novelty of the approach lies in the order in which calculations are performed and the selection of results that are saved to reduce the computation time. Next, the proposed ray tracing method is described and then the evaluation of the irradiance using the ray tracing results is explained.

3.4.1. RAY TRACING

When surfaces in the scene have arbitrary shapes and orientations, it is not possible to calculate view factors using closed-form formulas as in 3D view factor models and the scene must be sampled by casting rays. In this section, the scene in Figure 3.2a is used to illustrate the steps of the ray tracing algorithm in the proposed approach.

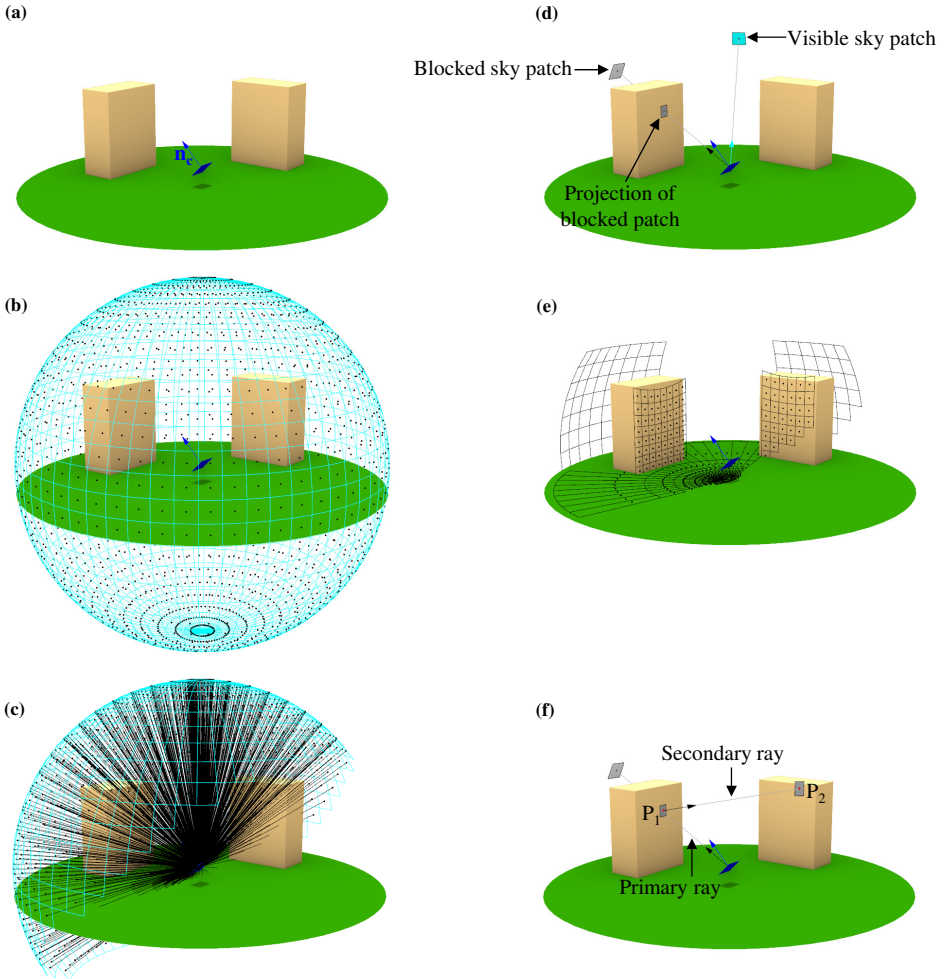


Figure 3.2: Graphical representation of the proposed ray tracing approach. (a) Example of a solar cell surrounded by two obstacles. (b) Spherical discretisation. (c) Hemispherical sampling. (d) Visible and blocked sky patches. (e) Projection of the blocked patches on the surfaces intersected by the primary rays. (f) Primary and secondary rays.

First, a deterministic hemispherical sampling is performed by discretising an imaginary sphere centred at the solar cell as shown in Figure 3.2b. In Figure 3.2b an equiangular discretisation is applied, yet it is important to note that the method is not limited to this specific discretisation. With the sky discretisation, the view factors from the solar cell to each sky patch ($dF_{c \rightarrow s}$) are determined by the position (\mathbf{s}) and the solid angle of the sky patch ($d\Omega$) as expressed in Equation (3.4).

Next, primary rays are cast from the centre of the solar cell to the centroids of the sky patches in front of the cell (Figure 3.2c). Intersections between the scene and the rays can be solved by combining an appropriate data structure (e.g., octrees, kD-trees, etc.) with

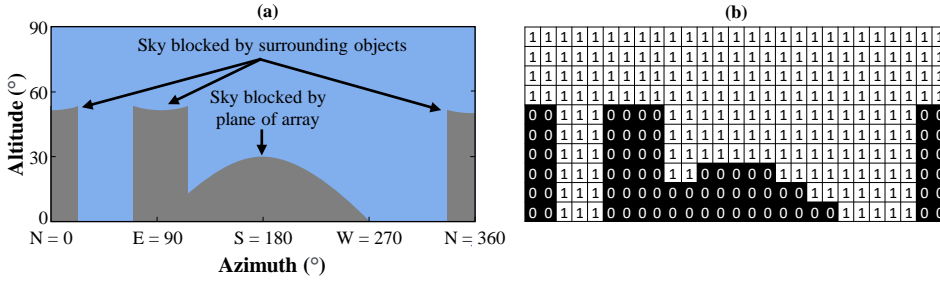


Figure 3.3: Skyline representation. (a) Sky view at the centre of the solar cell in Figure 3.2a, which is facing North and tilted 30° . (b) Corresponding shadow map. The angular resolution of this map was chosen only for illustrative purposes. The typical resolution of shadow maps is 1° or higher.

efficient ray-surface intersection algorithms (e.g., Möller–Trumbore [117]). Rays that do not intersect with surfaces in the scene correspond to sky patches that are visible from the solar cell ("visible sky patch" in Figure 3.2d). For rays that intersect with surfaces in the scene, the projections of the corresponding sky patches at the intersection points are considered ("projection of blocked patch" in Figure 3.2d). It should be noted that the view factor from the solar cell to each blocked sky patch (in Figure 3.2e) is equivalent to the view factor from the solar cell to the corresponding projected patches. A list with all the blocked rays and the indices of the corresponding intersected surfaces is stored in memory after the primary ray tracing.

A second independent hemispherical sampling is performed with a higher angular resolution from the centre of the solar cell to generate a shadow map. A shadow map is a binary representation of the sky visibility from a given point in the scene and it will be used to calculate the beam irradiance component. To generate shadow maps only rays that point forward from the solar cell and to the sky need to be traced. An example of a shadow map is shown in Figure 3.3, where the zeros correspond to sky patches blocked by the objects on the scene and ones to visible sky patches. The resulting shadow map is stored in memory. Shadow maps are binary arrays and require very limited storage space despite the high angular resolution. Approximately, 1000 shadow maps with an angular resolution of 1° occupy only 3 MB.

Then, for each intersection point between a primary ray and the scene (i.e., for every primary intersection point), the simulation develops differently depending on the type of intersected surface. If the intersected surface is an ideal specular reflector, a single secondary ray is cast from the primary intersection point. The direction of the secondary ray is given by the specular reflection of the primary ray on the intersected surface. If the secondary ray does not intersect with the scene, the index of the pointed sky patch is associated with the specular reflector patch and stored in memory, otherwise, it is neglected. Otherwise, if the surface intersected by the primary ray is a Lambertian reflector, a secondary hemispherical sampling is performed from the primary intersection point (e.g., P_1 in Figure 3.2f). Again, some of the rays cast during the secondary hemispherical sampling will reach the sky and some will intersect with surfaces in the scene at secondary intersection points (e.g., P_2 in Figure 3.2f). The results of each of the secondary

hemispherical samplings are stored in memory, same as in the case of the primary sampling. A shadow map is also generated and stored at every primary intersection point on a Lambertian reflector.

Finally, at each secondary intersection point (e.g., P_2 in Figure 3.2f), the proposed approach only calculates the beam and diffuse irradiance contributions. For this purpose, a third-order hemispherical sampling is performed to generate shadow maps at every secondary intersection point. The shadow map, the secondary intersection point and the normal to the intersected surface are also stored in memory. To reduce the number of hemispherical samplings, new shadow maps are only calculated when a new intersection point is further than a specific user-defined distance from all previously calculated and stored intersection points².

The described ray tracer only distinguishes between specular and diffuse reflectors. Therefore, the results of the hemispherical samplings and the shadow maps stored in memory are independent from the sky radiance and the reflectivity of the surfaces in the 3D model. Once the ray tracing calculations are completed, the irradiance is calculated as explained in the following section.

3.4.2. IRRADIANCE COMPONENTS EVALUATION

The beam irradiance incident on the solar cell is calculated by multiplying Equation (3.2) and the shading factor (SF). The shading factor is the time-dependent binary function defined in Equation (3.7) that indicates when the sun is blocked by the surroundings and it can be easily determined using shadow maps as look-up tables.

$$SF(t) = \begin{cases} 1 & \text{if the sun is visible,} \\ 0 & \text{if the sun is blocked,} \end{cases} \quad (3.7)$$

The discrete form of Equation (3.3) is employed to calculate the diffuse component of the irradiance incident on the solar cell considering the view factors from the cell to the unobstructed sky patches. In this chapter, the diffuse sky radiance (L_{sky}) in Equation (3.3) is calculated using Perez all-weather sky radiance distribution model [52].

The irradiance contribution of specular reflectors is calculated considering that the $BRDF$ is a Dirac delta function. Then, the irradiance contribution of an ideal specular patch with normal \mathbf{n}_r and solid angle $d\Omega_r$ intersected by a primary ray with direction \mathbf{r}_1 can be expressed as:

$$\begin{aligned} dG_{\text{refl}} &= L_{\text{sky}}(\mathbf{p}) F_R(\mathbf{p}, \mathbf{n}_r) (\mathbf{r}_1 \cdot \mathbf{n}_c) d\Omega_{r1} \\ &= \pi L_{\text{sky}}(\mathbf{p}) F_R(\mathbf{p}, \mathbf{n}_r) dF_{c \rightarrow r1} \end{aligned} \quad (3.8)$$

where \mathbf{p} is the specular reflection of \mathbf{r}_1 about \mathbf{n}_r , and F_R is the Fresnel factor which also depends on the refractive indices of the reflective material (n) and the air (n_{air}).

In the case of Lambertian reflectors with normal \mathbf{n}_r and solid angle $d\Omega_{r1}$, the contribution to the irradiance on the solar cell is calculated as:

$$dG_{\text{refl}} = \frac{\rho_1}{\pi} G_{\text{hemi}(r1)} (\mathbf{r}_1 \cdot \mathbf{n}_c) d\Omega_{r1} = \rho_1 G_{\text{hemi}(r1)} dF_{c \rightarrow r1} \quad (3.9)$$

²For the results presented in this chapter, this distance was set to 0.2 m

where ρ_1 and $G_{\text{hemi}(r1)}$ are the reflectivity and the irradiance of the primary Lambertian reflector intersected by \mathbf{r}_1 , respectively. The irradiance $G_{\text{hemi}(r1)}$ consists of three components: (1) the beam irradiance; (2) the diffuse irradiance; and (3) the reflected irradiance by secondary reflectors (i.e., surfaces intercepted by secondary rays). The first two components can be determined using Equation (3.2) and Equation (3.3) considering the position of each primary reflector instead of the position of the solar cell. The third component is calculated recursively using Equation (3.9) also from the positions of the primary reflectors. To limit the recursivity of the problem, the irradiance incident on secondary reflectors ($G_{\text{hemi}(r2)}$) is calculated considering only the sky beam and sky diffuse irradiance according to Equation (3.10).

$$G_{\text{hemi}(r2)} = DNI(\mathbf{b} \cdot \mathbf{n}_2) SF + Pz(DHI, SVF) \quad (3.10)$$

where \mathbf{n}_2 is the normal vector to the secondary reflector and Pz is the simplified Perez diffuse irradiance model³ according to which the diffuse irradiance is calculated as the sum of the circumsolar, horizon band and isotropic background contributions [47]. For each secondary reflector, the corresponding shading factor (SF) and sky view factor (SVF) can be calculated from the shadow maps stored in memory.

It should be noted that an intrinsic bias arises in this approach since it is limited to two ray reflections. This means that, even for an ideal simulation where the number of rays tends to infinity, the simulated irradiance on a specific sensor might differ from the actual irradiance received by the sensor. Assuming a perfect description of the optical properties of the materials in the scene and a perfect description of the sky radiance distribution, the proposed approach should result in an underestimation of the irradiance incident on the sensor. It is also worth noting, that this bias is implicitly present and even larger in view factor models (both 2D and 3D) because most methods described in the literature are equivalent to a ray tracing model limited to a single ray bounce. To compensate for this bias in view factor models, the most common practice consists in overestimating the irradiance incident on the ground by considering that unshaded sectors receive the global horizontal irradiance (GHI) and shaded sectors receive only the diffuse horizontal irradiance (DHI) [80], [81], [83], [96]. The overestimation of irradiance approximately compensates the bias introduced by the limitations of the view factor models. It is possible to apply a similar workaround to the proposed approach by adding a third term to Equation (3.10) to approximate the reflected light on secondary reflectors considering the local albedo α :

$$G_{\text{hemi}(r2)} = DNI(\mathbf{b} \cdot \mathbf{n}_2) SF + Pz(DHI, SVF) + \alpha GHI(1 - SVF) \quad (3.11)$$

The irradiance incident on the solar cell can be quickly recalculated using the ray tracing results if the reflectivity of a surface changes. This allows the efficient simulation of surfaces with time-varying reflectivity values by considering $\rho(t)$ in Equation (3.9).

Furthermore, all the presented equations can be expressed as a function of wavelength and later integrated over the relevant spectral range to quickly perform spectrally resolved irradiance simulations. While several studies propose spectral sky models [118]–[123], more research is needed to develop a generalised model that can accurately

³Refer to Equation (2.3) for the full expression of this term.

describe the spectral sky radiance in the presence of clouds. In this thesis, to demonstrate the ability of the proposed approach to perform spectral simulations, the solar spectrum was modelled combining *DNI* and *DHI* spectra generated with the SMARTS [124]–[126] and the SBDART models [127]. *DNI* and *DHI* spectra were originally generated for solar azimuth angles ranging from 0° to 89° in steps of 1° , and then interpolated to calculate the spectral distribution of the beam and diffuse components for different solar altitude angles. SBDART was used to generate spectra for 3 different sky conditions (clear, cloudy and overcast) and a *DNI*-based sky classifier was used to identify the sky condition at each time. By contrast, SMARTS can only generate spectra for clear sky conditions, thus it is expected to differ significantly from actual spectra measured under partially cloudy and overcast skies. The values of the parameters used to generate the spectra with SMARTS and SBDART are listed in Table 3.2.

SMARTS		SBDART			
Parameter	Value	Parameter	Clear	Cloudy	Overcast
Surf. Pressure	1013.25 mb	nf	1	1	1
Altitude	0 km	iast	0	0	0
Atmosphere	U.S. Std Atm 1976	wlinf	0.28	0.28	0.28
Water vapor	From atm. and alt.	wlsup	4	4	4
Ozone	Def. ref. atm.	wlinc	0.001	0.001	0.001
CO2	370 ppm	sza	01:29.5	01:29.5	01:29.5
Ext. Spectrum	Gueymard 2002	isalb	6	6	6
Aerosol model	Urban S&F	iadtm	6	6	6
Turbidity	0.084	uw	1.42	1.42	1.42
Albedo	Light soil	uo3	0.324	0.324	0.324
Spectral range	280 - 4000 nm	iaer	1	1	1
Circumsolar	Rad. aperture 2.9	tbaer	0.084	0.084	0.084
		zcloud	n/a	2	2.0 -6.0
		tcloud	n/a	1	60.0 60.0
		nre	n/a	10	20.0 20.0
		zout	0,1	0,1	0,1
		iout	1	1	1

Table 3.2: Parameters used for the generation of spectral *DNI* and *DHI* datasets with SMARTS and SBDART.

Another relevant characteristic of the proposed approach is that it allows for the direct inclusion of the incidence angle modifier (IAM) and transmissivity of the PV module front and rear layers [128]. Since the direction of all the irradiance contributions is known, the angular effects can be easily included by adding a multiplicative factor in Equations 3.2, 3.3 and 3.5. In opposition to most irradiance models that use an effective angle of incidence [129], with the proposed approach the optical losses associated the diffuse and reflected components can be more accurately calculated.

3.4.3. SKY CLASSIFICATION

A sky classifier algorithm is needed to select right the *DHI* and *DNI* spectra generated with SBDART according to the prevailing sky conditions. The algorithm in Figure 3.4 is proposed to distinguish the sky condition at each simulated time instant.

In essence the algorithm identifies and counts fluctuations in the *DNI* time series to classify the types of sky. A two-step approach is used to count dips in the daily *DNI* time series and select one out of three sky conditions (clear, cloudy or overcast) at each time instant. As a first step, the predominant sky condition during the entire day is identified by defining thresholds for a minimum daily average *DNI* and a maximum number of *DNI* dips per day. The threshold values used in this work are specified in Figure 3.4 and are valid only when using *DNI* data with minutely resolution. Subsequently to the general day type classification, the daily *DNI* time series is further evaluated by applying a 40 min moving window to identify variations in cloud cover throughout the day.

It should be noted that the described sky classifier relies on the availability of *DNI* data with high temporal resolution, ideally with a sampling time of 10 minutes or less. If only hourly *DNI* data is available, a different algorithm should be implemented to determine the prevailing sky type. For instance, the sky brightness parameter used by Perez [52] could be employed to classify the sky without requiring additional weather measurements such as cloud cover measurements or all-sky images.

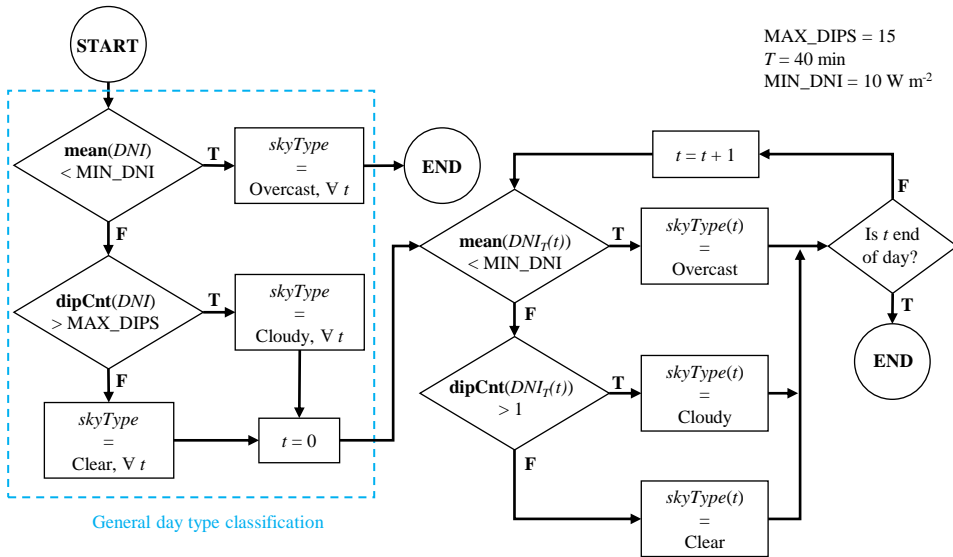


Figure 3.4: Simple *DNI*-based sky classifier algorithm. The function *dipCnt* calculates the number of dips in a time series. $DNI_T(t)$ indicates an interval of the *DNI* time series with length T and centred at instant t .

3.5. IRRADIANCE SIMULATIONS WITH *Radiance*

Radiance is a highly flexible and optimised lighting simulation tool that has been continuously improved and validated over the last three decades [116]. There are several

programs that form part of this software suite. The program `rtrace` was used to trace the rays through the scene, calculate the irradiance on the solar cells and benchmark the results. Therefore, it is relevant to highlight the similarities and differences between *Radiance* and the proposed approach.

In order to perform a ray tracing simulation with `rtrace`, the illumination conditions (i.e., *DNI*, *DHI* and the solar position) must be specified to generate a description of the light sources with the program `gendaylit`. In *Radiance*, direct and diffuse light sources are sampled separately [116]. The sun is considered a directional point light source and it is sampled with a single deterministic ray. The sky dome is considered an extended diffuse light source described by Perez model [52] and it is sampled stochastically. The stochastic sampling approach, can reduce noise and artefacts in image rendering more efficiently than the proposed deterministic sampling [130].

Unlike the proposed approach, *Radiance* is not limited to 2 ray bounces nor to simulate ideally diffuse and specular reflectors. The calculation of diffuse interreflections in *Radiance* can be controlled with a user-defined parameter that sets the maximum number of ray bounces. Moreover, the user can define arbitrary *BPDF* functions to simulate translucent and reflective materials.

In addition, ray tracing calculations are accelerated using the irradiance caching algorithm [131] that significantly reduces the number of points where higher order hemispherical samplings need to be performed. Irradiance caching is based on the assumption that diffuse illumination varies slowly over the scene, and hence it is not always necessary to initiate a new hemispherical sampling at each intersection point between a sampling ray and the scene. Under certain conditions, the irradiance at the new sampling point can be interpolated from cached values using irradiance gradients. The user can control the radius of validity of the gradient-based interpolation with different input parameters.

The most relevant parameters when performing a simulation with `rtrace` are the following:

- Ambient divisions (`ad`): it indicates the number of primary rays used for hemispherical sampling.
- Ambient super-samples (`as`): it indicates the number of additional sample rays used in ambient divisions that present high variance.
- Ambient bounces (`ab`): it limits the maximum number of ray bounces allowed in the calculation of interreflections.
- Ambient accuracy (`aa`): there is an associated error that is estimated for each point where the irradiance is interpolated using irradiance gradients. If the interpolation error is larger than the ambient accuracy parameter, interpolation cannot be used and a new hemispherical sampling is initiated.
- Ambient resolution (`ar`): it determines the minimum distance between ambient sampling points. When the distance between two sampling points is smaller than the maximum scene dimension multiplied by `aa` and divided by `ar`, the new ambient value is interpolated from the irradiance gradient independently of the error associated with the interpolation.

A major difference between `rtrace` and the proposed approach is the computation time. When the program `rtrace` is used to simulate the irradiance on a sensor point, the density of sampling rays is adapted according to the scene brightness to refine the sampling in regions with larger irradiance gradients. Hence, the ray tracing simulations must be repeated at every time step and sky condition⁴. Hence, the total computation time increases linearly with the number of simulated time instants. On the contrary, the total computation time with the proposed approach is almost independent of the number of simulated instants.

Another important aspect is that the proposed approach can easily handle dozens of spectral bands. However, *Radiance* is limited to only three independent channels (R, G and B) to calculate spectral irradiance. These channels can be used to perform spectral simulations using 3 arbitrary spectral bands, not necessarily in the visible spectrum. As a result, when using *Radiance*, ray tracing simulations must be repeated to evaluate the spectral irradiance with more bands.

3.6. COMPUTATIONAL COMPLEXITY

The total computation time of ray tracing irradiance models is mainly determined by the total number of cast rays.

In *Radiance*, the irradiance caching algorithm limits the geometric growth of the number of samplings required to solve diffuse interreflections. Assuming that in average, the irradiance caching algorithm reduces the number of sampling required at each higher level by 50 % [116], the total number of rays that are traced in one `rtrace` execution with $ab = 2$ is approximately equal to:

$$R_1 = r + \frac{r^2}{2} + \frac{r^3}{8} \quad (3.12)$$

where r is the original number of sampling rays (i.e., primary rays). The irradiance caching algorithm is particularly effective to evaluate the irradiance on multiple test points, thus R_1 is assumed to be independent of the number of evaluated test points. Nevertheless, since `rtrace` must be executed once per simulated time instant, the total number of traced rays and thus the total computation time increase linearly with the number of simulated time steps.

By contrast, the total number of rays that are traced with the proposed approach is independent of the number of simulated time steps, and it equals to the sum of the primary rays, secondary rays and the rays needed to generate the shadow maps. Therefore, the total number of rays needed to evaluate p test points with the proposed approach is:

$$R_2 = p (r + r^2 + r_m + r r_m^2) + m r_m \quad (3.13)$$

where r is the number of rays cast in each primary and secondary samplings, r_m is the number of rays cast to create each shadow map, and m is the number of shadow maps to solve the irradiance at secondary intersection points. For shadow maps with an angular resolution of 1° , $r_m = 360 \times 90$. Since shadow maps at secondary intersection points are

⁴Alternatively, the program `rfluxmtx` in *Radiance*, can be used to calculate daylight coefficients [132], but this program was not used for this study.

cached, typically less than 10000 shadow maps are enough to calculate the irradiance on all secondary intersection points.

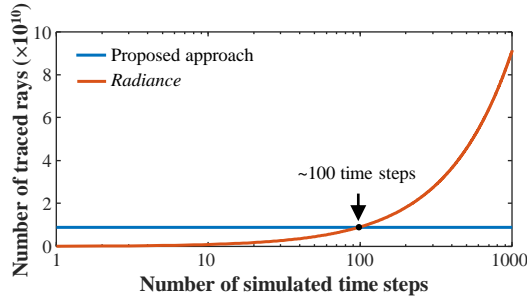


Figure 3.5: Required number of rays for a typical simulation of a 72-cell PV module. The number of required rays is approximated using Equations 3.12 and 3.13 where $r = 900$, $r_m = 32400$, $p = 288$ and $m = 10000$.

Figure 3.5 shows a comparison between the total number of rays required by `rtrace` (*Radiance*) and the proposed approach for simulating a PV module with 72 solar cells and 4 test points per cell. The figure shows that the ray tracing calculations with the proposed approach take about the same time as 100 `rtrace` executions. In other words, the proposed approach is faster than using `rtrace` when simulating more than 100 time steps.

It should be noted that, for irradiance simulations in scenes with invariant optical properties, the daylight coefficient method is relatively faster compared to the proposed approach. As daylight coefficients can be calculated applying a stochastic and adaptive hemispherical sampling method, less rays need to be traced compared to the deterministic hemispherical sampling in the proposed approach to achieve a similar level of accuracy. On the other hand, when performing spectrally resolved irradiance simulations, the computation time of the daylight coefficient method increases linearly with the number of spectral bands and is significantly higher than that of the proposed approach.

3.7. EXPERIMENTAL VALIDATION

3.7.1. MEASUREMENT SETUP

The irradiance model described in Section 3.4, was implemented and validated using measurements taken at the PVMD monitoring station shown in Figure 3.6a located in Delft, the Netherlands.

At the monitoring station, a Kipp & Zonen SOLYS2 sun tracker equipped with a SMP 21 pyranometer and a SHP1 pyrhemliometer was used to measure the diffuse horizontal irradiance (*DHI*) and the direct normal irradiance (*DNI*), respectively. The three irradiance sensors indicated in Figure 3.6b were used to validate the model: a monocrystalline ISET sensor (IKS Photovoltaik) facing south and tilted 30° (S1); a SMP10 thermopile pyranometer (Kipp & Zonen) facing 65° east of north and tilted 90° (S2); and a MS-700 spectroradiometer (EKO Instruments) mounted horizontally (S3).

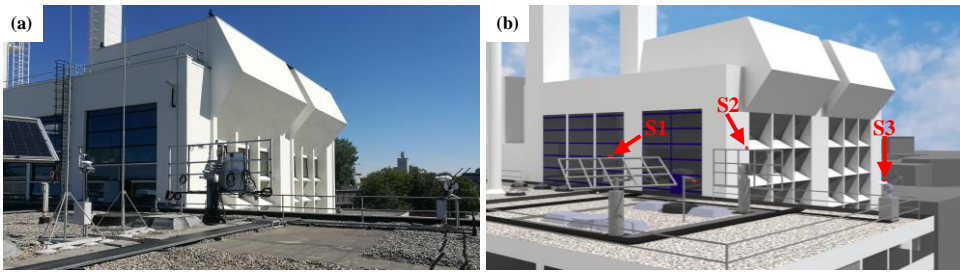


Figure 3.6: PVMD monitoring station. (a) Photograph. (b) Ray traced rendering of the CAD model.

The 3D model of the monitoring station shown in Figure 3.6b was created to simulate the irradiance at the position of sensors S1, S2 and S3. The 3D model was built combining information from floor plans, Lidar data and in-situ measurements. The accuracy of the 3D model was evaluated by comparing photographs taken with an Horicatcher device with raster images generated from the 3D model. The relative difference in the sky view factor between the photographs and the raster images was below 2% for the 10 positions evaluated. Rasterised images generated with the implemented ray tracer from the perspective of the three sensors are shown in Figure 3.7.

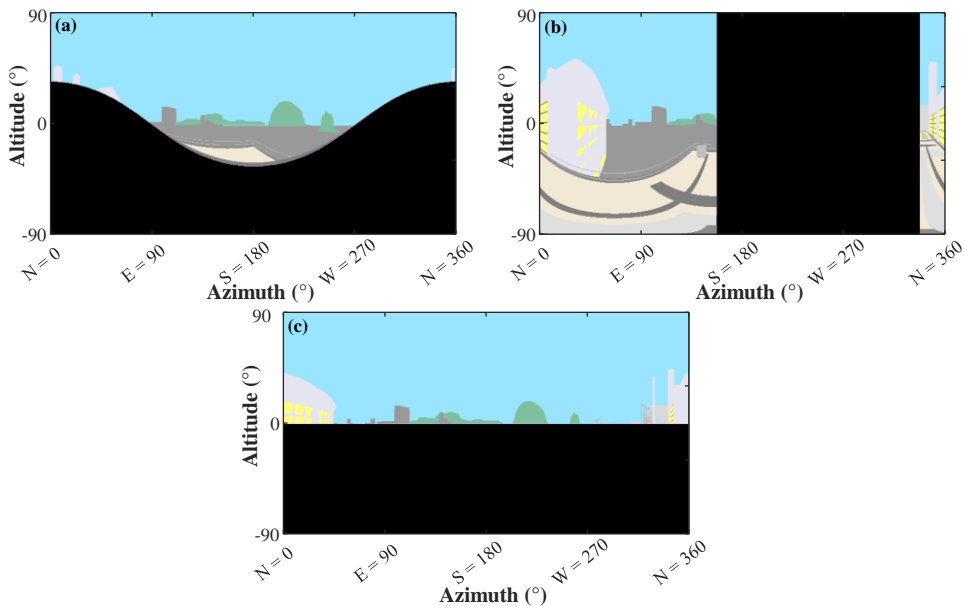


Figure 3.7: Field of view images generated with the implemented ray tracer. The black regions represent the hemisphere behind the PoA. (a) View from reference cell S1 tilted 31° facing south. (b) View from pyranometer S2 tilted 90° facing 65° east of north. (c) View from spectroradiometer S3 installed horizontally.

All the surfaces in the 3D model were defined as either ideal specular or Lambertian reflectors. Samples of the most relevant surfaces in the scene were characterised

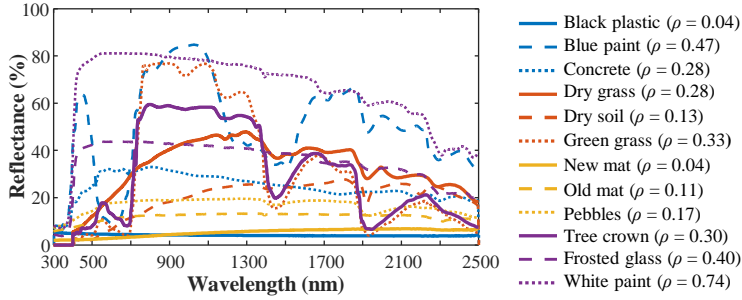


Figure 3.8: Spectral reflectivity of the surfaces in the scene. The weighted average reflectivity of each material considering the AM1.5G solar spectrum is indicated in the legend in between parentheses.

using a LAMBDA 1050 spectrophotometer. The spectral reflectance of the surrounding vegetation and the concrete was retrieved from the ECOSTRESS Spectral Library [133], [134]. The spectral and average reflectivity of all the materials in the scene is presented in Figure 3.8.

3.7.2. SIMULATION PARAMETERS

The irradiance calculated with the proposed approach was compared to measurements and to simulations performed with *Radiance*. The selection of the input parameters for *rtrace* is crucial to obtain accurate results and reasonable computation times. Considering the size and the level of detail of the scene the following values were chosen: $ad = 1024$, $as = 64$, $ab = 2$, $aa = 0.1$, $ar = 1024$.

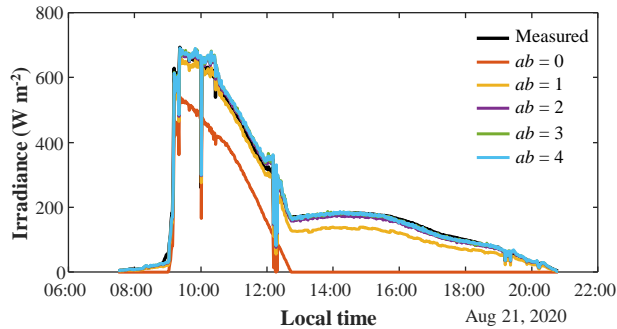


Figure 3.9: Effect of the ambient bounces (ab) parameter on the simulated irradiance on sensor S2 with *Radiance*. The simulation with $ab = 0$ only calculates the beam irradiance incident on the sensor.

The effect of the ambient bounces (ab) in the simulated irradiance on sensor S2 is shown in Figure 3.9 using minutely *DNI* and *DHI* measurements of a clear sky day as inputs to the Perez model. As already explained, higher ab improves the accuracy of the simulation. However, doubling the value of ab approximately doubles the computation time. Due to the highly reflective white wall ($\rho = 0.74$) in front of the sensor, it is clear in Figure 3.9 that more than one ambient bounce is required to obtain reasonable results.

The normalised⁵ mean bias errors (nMBE) and root square errors (nRMSE) obtained for different ab values are summarised in Table 3.3. As expected, results converge when the number of ambient bounces is increased. In this scenario, the most accurate simulation ($ab = 4$) overestimates the daily irradiation by 2% as indicated by the nMBE value in Table 3.3. Results show that in this case more than 3 ambient bounces do not contribute to improve the simulation accuracy, yet it significantly increases the total computation time. For the simulations presented in the following section the ab parameter was set to 2, since this ab value offered the most reasonable compromise between accuracy and computation time.

ab	nMBE (%)	nMAE (%)	nRMSE (%)
0	58.0	58.0	65.1
1	12.3	12.4	14.5
2	0.3	4.1	5.6
3	-2.0	3.9	6.3
4	-2.1	4.0	6.3

Table 3.3: Normalised mean bias error, mean absolute error and root mean square error corresponding to Figure 3.9. Errors are normalised by the mean of the measured data and negative nMBE values indicate that the simulation overestimates the computed irradiation.

To make a fair comparison between the proposed approach and *Radiance*, the number of primary rays in both models must be similar. The simulation results of the proposed approach presented in the following sections were obtained using an equiangular discretisation (Figure 3.2b) with 60 azimuthal and 30 polar divisions. Hence, when hemispherical sampling is performed, 900 rays are cast with the proposed approach compared to the ad value of 1024 typically employed in *Radiance*.

When using the proposed approach, the results of the ray tracing calculations for each of the simulated sensors were stored in memory to accelerate the irradiance calculations. Ray tracing results include the indices of the primary and secondary rays that intersect with the scene, the normal vectors and optical properties of the intersected surfaces, and shadow maps. Considering that the simulation results with 900 primary rays occupied only 5 MB on average per each evaluated test point, the ray tracing results of a 72-cell PV module with 4 test points per cell in a similar complex scenario would occupy less than 1.5 GB of storage space.

3.7.3. IRRADIATION SIMULATIONS

The irradiance incident on sensors S1 and S2 was simulated using minutely *DNI* and *DHI* measurements taken between August 2020 and February 2021. A comparison between the proposed approach and *Radiance* was carried out considering the average reflectivity values for the surfaces listed in Figure 3.8.

The incidence angle modifier (IAM) of reference cell S1 was modelled according to the physical model presented in [135] since manufacturer data was not available. In the proposed approach, the calculation of the IAM for the radiance incident on the solar

⁵Errors are normalised by the mean irradiance value.

cell from each direction is straightforward, as explained in Section 3.4.2. On the other hand, `rtrace` does not output the angular distribution of the incident radiance. Hence, to improve the simulation of the IAM effect, the diffuse and reflected components were separated from the beam component by performing simulations with 0 and 2 ambient bounces. Then, the angle of incidence of the beam component was calculated as in Equation (3.2), and the effective angle of incidence of the reflected and diffuse components (56.8°) was calculated according to [129].

In Figure 3.10 the irradiance simulated with the proposed approach is compared to the measurements of sensors S1 and S2 during days with clear and overcast sky conditions. The simulated global irradiance was decomposed into its three components. The reflected irradiance component on sensor S1 was almost negligible due to the low tilt of the sensor. Contrarily, the reflected component had a significant contribution to the global irradiance received by sensor S2, which was oriented vertically and in close proximity to a highly reflective white wall. This effect is more evident during the afternoon of the clear sky day (August 21, 2020), when the sun was behind the sensor and the white wall was directly illuminated.

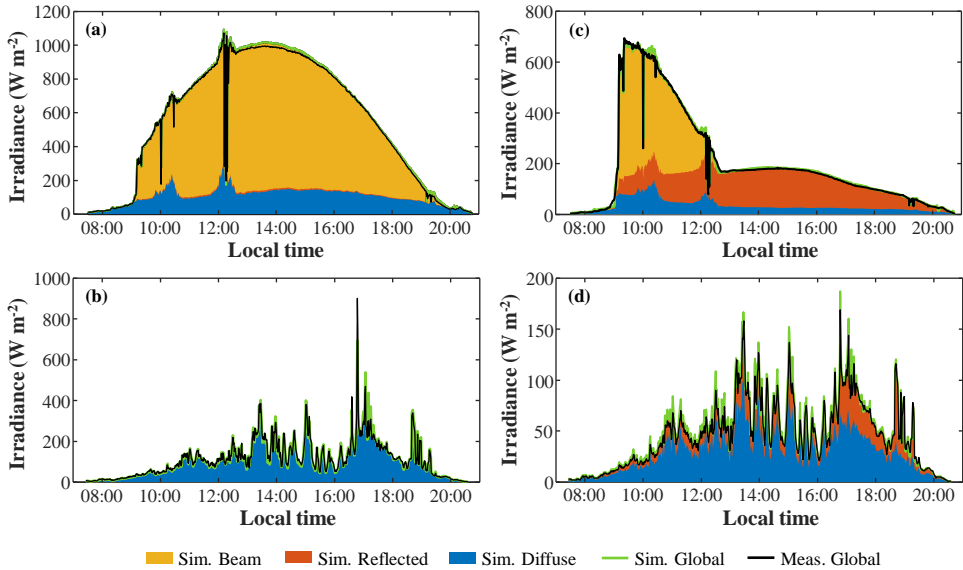


Figure 3.10: Simulated and measured irradiance on sensor S1 and S2. (a) Irradiance on sensor S1 under a clear sky (21 Aug. 2020). (b) Irradiance on sensor S1 under an overcast sky (26 Aug. 2020). (c) Irradiance on sensor S2 under a clear sky (21 Aug. 2020). (d) Irradiance on sensor S2 under an overcast sky (26 Aug. 2020)

The simulated weekly irradiation with proposed approach was compared to *Radiance* and against the measurements in Figure 3.11. The irradiation was calculated by integrating the minutely irradiance over an entire week after filtering out the outliers (0.2% of the data points). Both models match well with the measurements throughout the entire period. The relative mean bias error in the daily irradiation simulated with the proposed approach was 0.6% and 0.2% for sensors S1 and S2, respectively.

The normalised errors calculated based on minutely measurements are presented in

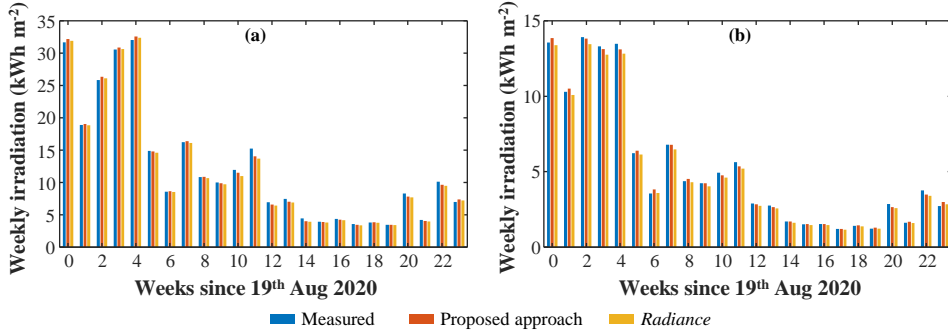


Figure 3.11: Comparison between the measured and simulated weekly irradiation on reference cell S1 (a) and pyranometer S2 (b).

Table 3.4. The error of the simulated irradiance on sensor S1 was more lower with the proposed approach than with *Radiance*, likely due to the approximation of the effective angle of incidence of the diffuse irradiance component. Despite the fact that reference cells tend to underestimate the measured irradiance in cloudy skies and low solar altitudes as a result of the spectral response of silicon [136], the simulated irradiances on reference cell S1 presents a lower nMAE compared to pyranometer S2. The reason being that sensor S1 received much less reflected irradiance than sensor S2.

	Proposed approach		<i>Radiance</i>	
Sensor	S1	S2	S1	S2
nMBE (%)	0.1	-0.1	1.4	3.4
nMAE (%)	7.7	8.1	7.2	7.6
nRMSE (%)	21.1	12.7	21.5	12.9

Table 3.4: Normalised mean bias error, mean absolute error and root mean square error of the simulated irradiance on sensors S1 and S2 between August 19, 2020 and February 5, 2021. Values are normalised by the mean of the measured data and negative nMBE values indicate that the simulation overestimates the irradiance.

It can also be noticed, especially in Figure 3.11b, that the proposed approach tends to yield higher values than *Radiance*. In part, this is because the proposed approach considers the contribution of the reflected irradiance on secondary reflectors expressed in Equation (3.11). If this contribution is neglected and Equation (3.10) is used instead, the nMBE of the proposed approach at sensor S2 is almost twice as high. On the other hand, the high nRMSE of sensor S1 is explained by the large response time difference between the reference cell S1 ($\tau_{95\%} < 100\text{ms}$) and the thermopile sensors that measure *DNI* and *DHI* ($\tau_{95\%} < 2\text{s}$). Especially during partially cloudy days when illumination conditions were varying quickly, the difference in response time caused an increased RMSE.

3.7.4. SPECTRAL SIMULATIONS

To demonstrate the ability of the proposed approach to perform spectrally resolved simulations, the measured and simulated irradiance at the position of spectroradiometer S3 are compared in Figure 3.12 during an entire day.

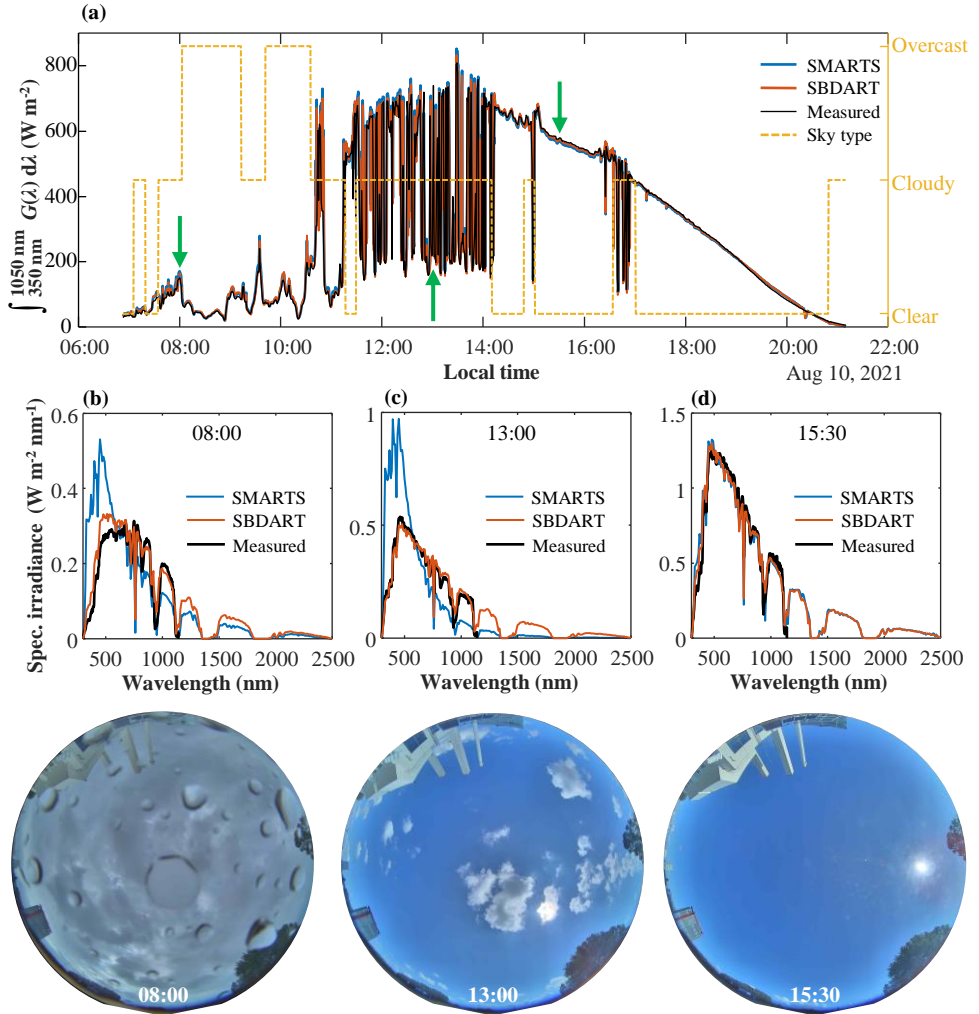


Figure 3.12: Spectral irradiance simulations with the proposed approach. **(a)** Integrated measured and simulated spectral irradiance on sensor S3. The green arrows indicate the instants at which the spectra are compared. The yellow dashed line indicates which SBDART spectra was chosen at each instant according to the simple sky classifier in Section 3.4.3. **(b,c,d)** Spectra and sky images at 8:00 a.m., 1:00 p.m. and 3:30 p.m., respectively.

The spectral irradiance was simulated with 5 nm resolution between 300 nm and 2500 nm, using *DNI* and *DHI* measurements to scale the spectra generated with SMARTS and SBDART. The time resolution for the spectral simulations was 30 s. Using the pre-

calculated ray tracing solution at the position of S3, it took approximately 3 min to evaluate the spectral irradiance for an entire day.

The irradiance in Figure 3.12a was integrated between 350 nm and 1050 nm, which is the valid measurement range of S3. It should be noticed, that this wavelength range concentrates approximately 77.5% of the power in the AM1.5G spectrum and covers the most significant part of the spectral responsivity of any PV module on the market. The sky camera pictures in Figure 3.12, show that during the morning it was rainy and the sky was overcast. Towards the afternoon the clouds dispersed and the sky became clear. Overall, the simulated integral irradiance was in good agreement with the measurements. The largest deviations from the measurements occurred when the sun was covered by clouds.

In particular, the comparison between the measurements and the simulations using SMARTS spectra as input (Figure 3.12b) shows a significant spectral mismatch in the morning. This mismatch was expected since clouds cause a red-shift in the spectrum [118] and SMARTS can only be used to generate spectra for clear sky days. As clouds disappeared in Figure 3.12d and Figure 3.12e, the spectral match improved for the same reasons.

As expected, the results of the simulations in the presence of clouds using SBDART spectra as input are in better agreement with the measurements than the results obtained with SMARTS input spectra. However, the spectral mismatch at 8 a.m. illustrates the challenge of generalising cloudy and overcast spectra. Spectral matching in the presence of clouds could be improved by defining new sky types and using additional inputs to the sky classifier algorithm to identify each sky type.

These results show that the proposed approach is able to perform simulations with high spectral and temporal resolution. Nevertheless, it is also evident the importance of using a proper sky model to describe the effect of clouds.

3.8. CONCLUSIONS

In this chapter, a simulation approach for the accurate computation of the irradiance incident on PV systems in geometrically complex scenes was introduced. The approach is based on a backward ray tracer limited to two ray bounces, which only considers ideally diffuse and specular reflectors to simplify the calculation of interreflections.

The presented method can be considered an extension of the daylight coefficient method for it allows the decoupling of the solution of the ray tracing problem from both the reflectivity of the surfaces in the scene and the illumination conditions. This leads to a significant reduction in computation time in comparison to conventional ray tracing simulation approaches. The highly time-consuming ray tracing calculations only need to be performed once, and the results are stored in memory to quickly evaluate the irradiance profile on the module under different illumination conditions.

The proposed approach facilitates the simulation of spectral irradiance with high resolution (over 100 spectral bands), which otherwise implies very long computation times, even with the daylight coefficient method. Furthermore, the capability to distinguish between different types of reflectors instead of using a single albedo value, can improve the calculation accuracy on PV modules that receive a high proportion of reflected light. By enabling the calculation of the spectral irradiance and including surfaces with

time-varying optical properties in the 3D model, the proposed approach is particularly well-suited to the simulation of bifacial and tandem PV systems.

The accuracy of the proposed approach was evaluated using different types of irradiance sensors installed at the PVMD monitoring station, in the Netherlands. From the comparison of the simulations to measurements taken with a pyranometer and a reference cell, it was determined that the relative mean bias and mean absolute errors in irradiation over a period of 6 months were lower than 0.1% and 8.1%, respectively. In addition, a comparison with *Radiance* limited to two ambient bounces, suggests that the optical performance of the proposed approach is slightly better and the computation time can be significantly reduced when performing annual irradiance simulations with minutely resolution.

Finally, spectral simulations were performed using pre-generated beam and diffuse spectra as inputs, and compared to measurements taken with a spectroradiometer. Results indicate that even though the proposed approach is capable of quickly computing the incident irradiance with high spectral and temporal resolution, in some cases the simulated spectrum can significantly differ from the measurements. While under clear sky conditions, there is a good agreement between measurements and simulations, in the presence of clouds there is a larger mismatch. These results put in evidence the need for more sophisticated spectral sky models to reproduce the atmospheric conditions with greater accuracy and properly account for the effect of cloud cover in irradiance simulations.

4

SHADING TOLERANT PV MODULE TOPOLOGIES

This chapter is based on the following publication:

A. Calcabrini, R. Weegink, P. Manganiello, M. Zeman, O. Isabella, *Simulation study of the electrical yield of various PV module topologies in partially shaded urban scenarios*, *Solar Energy* **225**, 726 (2021).

The deployment of photovoltaic (PV) systems in urban environments has the potential to supply a significant share of the urban energy demand and to make a positive impact on different aspects of urban sustainability [137]. Nevertheless, while utility-scale PV power generation continues to break price records [138], the average levelised cost of electricity (LCOE) of residential solar PV still remains three times higher [139]–[141]. The large disparity in LCOE is mainly caused by (i) the scale difference between utility and residential PV systems, (ii) the fact that high end components are more frequently used in residential installations, and (iii) the characteristics of the solar potential in urban landscapes, which is uneven and ever-changing due to surrounding buildings, trees and other structures [142]. In this context, the development of shade resilient PV modules can contribute to increase the energy performance and reduce the payback time of urban PV systems. The following chapters are dedicated to evaluating different approaches to improve the performance of partially shaded PV systems.

4.1. INTRODUCTION

Crystalline silicon (c-Si) is the dominant photovoltaic module technology in the market. Many different c-Si modules are readily available, which differ in cell technology, number of cells, encapsulation, frame design, etc. Despite these differences, the electrical interconnections between the cells in most commercial PV modules is a common denominator: most PV modules have all their solar cells connected in series to limit the

output current of the PV module and thereby minimise resistive losses.

Typically, PV modules include bypass diodes to prevent hot-spots [143]–[145] and limit the effect of shading on the module's output power. Conventional c-Si modules depicted in Figure 4.1a consist of 60 (or 72) series-connected solar cells arranged in 3 sub-strings, where each sub-string is a group of 20 (or 24) series-connected cells under the same bypass diode. The way in which diodes are connected to the solar cells is most effective in the case of row-to-row shading in large PV power plants, when proper installation ensures that the shadow is parallel to the longer edge of the module. However, in the urban environment, chimneys, dormers, trees, and other objects usually cast time- and shape-varying shadows on the modules, which result in a poor electrical performance of the PV system.

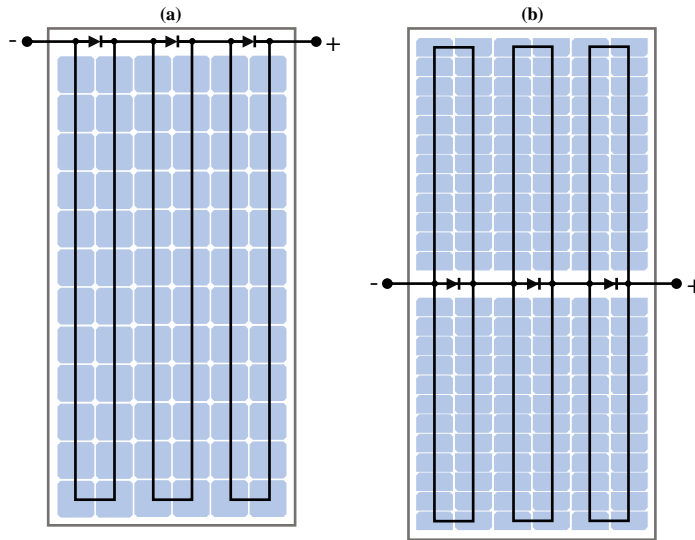


Figure 4.1: Most common c-Si PV module topologies. (a) Conventional topology. (b) Half-cell (or twin) topology.

During clear sky days, the irradiance on the unshaded solar cells in a module can be one order of magnitude higher than the irradiance on the shaded solar cells. When there is irradiance mismatch between cells, conventional modules perform poorly because the breakdown voltage of typical front-back contacted c-Si solar cells is between -10 V and -30 V [146]–[148]. As a consequence, when a cell in a sub-string is shaded, it can be driven into reverse bias operation and limit the current flow. Depending on the operating current of the PV module, one shaded cell can cause the inversion of the voltage across the entire sub-string. In this situation, the bypass diode conducts the additional electrical current generated by the unshaded sub-strings in the module mitigating the irradiance mismatch loss. Nonetheless, the use of bypass diodes also has its downsides: the output power of a conventional PV module can drop by more than 30% even when less than 1% of the area of a PV module is shaded [149].

The most straightforward alternative to improve the electrical yield of partially shaded

PV systems consists in using module level power electronics (MLPE). MLPE devices, including micro-inverters [150]–[152] and DC power optimisers [153], [154], can independently maximise the output power of every PV module in the system. Although MLPE devices have some limitations, such as current decoupling [155] in power optimisers and higher system's costs compared to string inverters, these devices contribute to improve the system's reliability [156] and increase the electrical yield of partially shaded PV systems [149], [157]. Taking it to the next level, power electronics can also be implemented at sub-module, this is the case of full power processing sub-module integrated converters (FPP subMICs) [158]–[160] and differential power processing (DPP) subMICs [161]–[163]. Sub-module-level power converters are a promising approach to boost the shading tolerance of PV modules at the expense of higher cost and complexity.

To increase the energy yield of partially shaded PV systems even further, the design of the PV module must be modified. For example, the shading resilience of an individual solar module can be improved by adding more bypass diodes. In [164] the authors explain how the shading tolerance of a series-connected PV module can be enhanced by increasing the number of bypass diodes and replacing conventional bypass diodes with active bypass elements (e.g., smart bypass diodes). Furthermore, a recent study, shows that PV modules manufactured with one bypass diode per cell can deliver 80 % more power than a conventional PV module when a row of cells is shaded [165]. However, it is yet unclear how much additional electrical energy PV modules with multiple bypass diodes can generate annually compared to conventional modules in realistic scenarios. In practice, a fair evaluation is complex since it requires the monitoring of different PV module topologies in various shading scenarios for long periods of time.

A different approach for increasing the shading tolerance of PV modules consists in connecting solar cells in parallel. While the relation between the maximum power point current and the illumination level is almost linear, the relation between the maximum power point voltage and the incident irradiance is logarithmic [166]. As a result, parallel connections of solar cells are more shading tolerant than series connections. The most common configurations with parallel connections are series-parallel (SP) and total-cross-tied (TCT) modules. An example of an SP module is the Tessera module, which consists of 15 parallel-connected building blocks, each block made of 64 series-connected sub-cells grouped in 4 units, each unit protected by a bypass diode [167]. Series-parallel connections are also present in half-cut cell modules (illustrated in Figure 4.1b), which perform better than conventional PV modules under partial shading conditions mainly when shadows are parallel to the short edge of the module [168], [169]. Total-cross-tied configurations present similar advantages to SP topologies and are also gaining more interest [170].

Previous research on the evaluation of shading tolerance of PV modules [164], [171]–[175] focuses either on the performance of a single (or few) innovative PV module topologies and/or on the evaluation of the power increase in specific shading cases (e.g. row shading, corner shading) at specific time instants and for short time periods (few days at most). The main reason for such a limited analysis is the excessive computational time needed for a thorough and fair comparison.

In this chapter, a simple methodology is presented for comparing shading tolerant PV module topologies in terms of annual DC yield gain (or loss) in realistic shading sce-

narios. Yearlong comparison represents a huge advantage, since it takes into account the probability of occurrence of different shading patterns during an entire year.

4.2. STUDY CASES

4.2.1. SHADING SCENARIOS

Two rooftops were chosen to carry out this simulation study. These "shading scenarios", reconstructed using photogrammetry data from actual buildings, are shown in Figure 4.2. On the red rooftops in Figures 4.2a and 4.2d, a 156-mm-spaced squared grid was generated to compute the irradiance on each cell. In turn, the squared cells on the rooftop were grouped to define modules with 72 cells (organised in a 6-by-12 layout). Furthermore, on each rooftop two scenarios were considered in which modules were either mounted in landscape or portrait orientation.

4

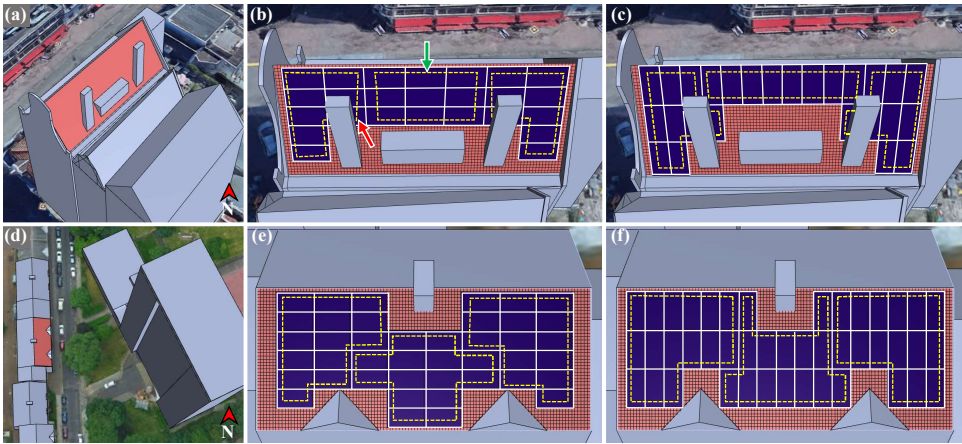


Figure 4.2: Simulated PV rooftops. **(a)** Rooftop 1 (RT1): The roof is tiled 57° facing 214° east of north. **(b)** PV array with 25 modules mounted in landscape on RT1. The green and the red arrows indicate the least and most partially shaded PV modules in the array in Rotterdam, respectively. **(c)** PV array with 26 modules mounted in portrait on RT1. **(d)** Rooftop 2 (RT2): The roof is tilted 30° and facing 100° east of north. **(e)** PV array with 42 modules mounted in landscape on RT2. **(f)** PV array with 44 modules mounted in portrait on RT2.

The shadows on each rooftop have different characteristics. Rooftop 1 (RT1) is facing southwest and shading is mainly caused by two chimneys. Due to the short distance from the rooftop to the chimneys, shadows are relatively small and move slowly on the PV array. The shadow's edges are sharp and during clear sky days there is a large irradiance difference between the shaded and unshaded sectors of the roof. On the other hand, Rooftop 2 (RT2) is facing east and shadows are mostly caused by the tall building in front of the rooftop, which is about 30 m away. In this case, shadows, which occur during the morning, move faster on the rooftop and the shadow's edges are more diffuse. Also, the irradiance difference between shaded and unshaded parts of the rooftop is less pronounced than in the case of RT1.

Furthermore, it was considered that these shading scenarios can be found in three different cities, for which 10-minute resolution climate data was generated with Me-

City	Latitude (°)	Irradiation (MWh m ⁻²)	Cloud cover (okta)
Rotterdam	51.9	1.02	5.6
San Francisco	37.2	1.71	3.3
Bogotá	4.6	1.57	5.9

Table 4.1: Climatic parameters for each of the 3 locations analysed. Irradiation values correspond to the annual global horizontal irradiation and cloud cover values are the average annual cloud cover during daytime.

teonorm [176]. All the locations considered are in the northern hemisphere but the available solar resources in each place differ significantly as shown in Table 4.1.

4.2.2. MODULE TOPOLOGIES

As mentioned in Section 4.2.1, PV modules made of 72 cells organised in a 6-by-12 layout were considered in this study. Contiguous cells can be grouped together to form different module layouts. In this analysis, the 24 module layouts shown in Figure 4.3 were evaluated. Furthermore, two different types of electrical interconnections were evaluated for each PV module layout: (1) modules with bypass diodes (BPD), in which all cells are connected in series forming groups and each group has its own bypass diode; and (2) series-parallel modules (SP), in which cells within a group are connected in series and all groups are connected in parallel. This amounts to 48 different PV module topologies.

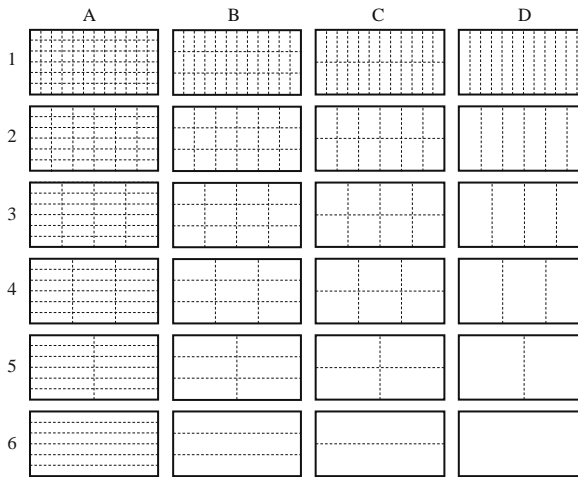


Figure 4.3: Analysed module layouts. Each layout is identified by a letter (column) and a number (row). Each layout consists of a matrix of 6 by 12 solar cells and dashed lines separate different groups of cells in the module.

Module layouts were named after the layout defined in Figure 4.3 and the type of electrical interconnection (BPD or SP). For instance, B6-BPD is the topology of a conventional 72-cell c-Si PV module with 3 bypass diodes; A1-BPD is equivalent to the Smart Hot-Spot Free module by AE Solar [177]; and B3-SP is similar¹ to the Tessera module

¹The Tessera module is actually made of 60 cells, where each cell is cut into 16 sub-cells and then connected

[178].

In addition to the 48 module topologies already mentioned, the performance of 144-half-cut cells PV modules (HC) was also evaluated. The topology of a half-cut cell PV module can be described as a series-parallel-series module with bypass diodes and it should not be confused with B5-BPD where all groups of cells are connected in series, nor with B5-SP where all groups of cells are connected in parallel with each other.

4.3. SIMULATION FRAMEWORK

In this chapter, the DC energy yield of a PV array was simulated with a framework that combines 3 models as shown in Figure 4.4: (1) an optical model to determine the photo-generated current of each solar cell in the module; (2) a thermal model to calculate the temperature of each solar cell; and (3) an electrical model to generate the I-V curve of the module and obtain the power delivered at the maximum power point. High accuracy of the simulation can be ensured by using experimentally validated models.

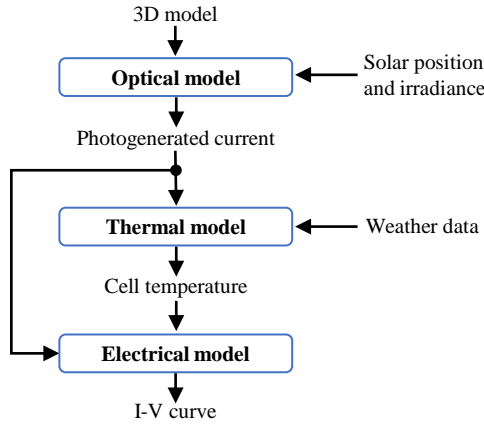


Figure 4.4: Block diagram of the modelling framework used to simulate the I-V curve of solar cells.

The optical model used in this work is the forward ray-tracing model proposed in [88]. To determine the irradiance incident on the cells, first, a 3D model of the PV modules and its surroundings was created. For simplicity, it was assumed that all the surfaces surrounding the PV modules are ideal diffuse reflectors with an albedo of 0.15. Then, sensitivity maps for each cell on the rooftop were generated using a ray-tracing engine. Lastly, the sensitivity maps, which quantify the fraction of the radiance emitted by each sky sector and received by the solar cell [88], were multiplied with sky maps generated with Perez model [52] to calculate the irradiance and the photo-generated current of each solar cell at every time instant.

Once the irradiance was determined, the Faïman model was used to calculate the cell temperature [179]. Only for the temperature calculation, it was assumed that each cell is operated at its maximum power point, which allows for decoupling the thermal

in series losses forming 15 series-parallel groups of cells. Hence, the Tessera module and configuration B3-SP are not exactly the same.

and electrical models. From the sunny side, it was also considered that module lamination is glass/foil and that the back side of the module is thermally insulated. The thermal constants for the Faïman model used in this work ($U_0 = 14.4 \text{ W m}^{-2} \text{ K}^{-1}$ and $U_1 = 0.034 \text{ W m}^{-3} \text{ s}^{-1} \text{ K}^{-1}$) were derived from the empirical coefficients reported in [180].

Knowing the cell temperature and the photo-generated current, the I-V characteristics of solar cells were simulated using the 2-diode electrical equivalent model [181]–[183]. It was considered that both the series and parallel resistances are temperature independent, and the diode's saturation current varies with the cell temperature as described in [184]. Finally, the I-V curves of the cells were added together to calculate the I-V curve of the entire PV module. In this last step, the losses in the interconnecting tabs were modelled as an additional resistance connected in series to each solar cell, and the losses in the bypass diodes [185] were calculated considering their I-V characteristics at 25 °C.

4.4. I-V CURVE APPROXIMATION

To assess the performance of the 49 different module topologies for the case studies presented in Section 4.2, the I-V curves of 137 PV modules using 3 climate data sets needs be simulated. Considering that it takes about 6 minutes to simulate the annual I-V curves of a single module with a 10-minute time step (on a PC with a 4-core Intel Xeon E5-1620 CPU with 16 GB of RAM), the simulation of all possible combinations using the highly accurate simulation framework presented above would take about 3 months. In order to reduce the computational time and perform a fair and reliable relative comparison between PV module topologies, the simulation framework presented above was adapted. Specifically, the two-diode electrical model was replaced with a squared approximation for the simulations presented in this chapter².

4.4.1. THE SQUARED APPROXIMATION

Essentially, the proposed approximation considers that the fill factor of the cell is 100 %, and hence the maximum power point of the solar cell is determined by the short-circuit current and the open-circuit voltage. The short-circuit current of the solar cell at any given irradiance G and cell temperature T , depends on the temperature difference from Standard Test Conditions (STC) conditions ΔT and the temperature coefficient of the short-circuit current α according to [186]:

$$I_{\text{sc}}(G, T) = I_{\text{sc0}} \frac{G}{G_0} (1 + \alpha \Delta T). \quad (4.1)$$

On the other hand, the open-circuit voltage at any given irradiance and temperature is defined similarly as in [180]:

$$V_{\text{oc}}(G, T) = V_{\text{oc0}} + \delta \ln \left(\frac{G}{G_0} \right) + \beta \Delta T, \quad (4.2)$$

²It should be noted that the square approximation is only applicable to the results and analysis presented in this chapter. In Chapters 5 and 6, the I-V curves of the PV cells and modules were simulated using the 2-diode model.

where β is the temperature coefficient of the open-circuit voltage, and two minor simplifications on the original model were considered. First, the parameter δ was taken as the product between the thermal voltage at STC and the ideality factor of the solar cell. And second, the slight variations in the number of photo-generated carriers at different temperatures was neglected in the ratio between G and G_0 .

Following the squared approximation of the I-V of a solar cell, when N_s solar cells are connected in series, the short-circuit current of the string is equal to the short-circuit current of the least illuminated cell and the open circuit voltage can be calculated as:

$$V_{oc-s} = N_s V_{oc0} + \delta \ln \left(\prod_{i=1}^{N_s} \frac{G_i}{G_0} \right) + \beta \sum_{i=1}^{N_s} \Delta T_i \quad (4.3)$$

Likewise, when N_p cells are connected in parallel, the voltage is limited by the least illuminated solar cell and the short-circuit current is given by:

$$I_{sc-p} = \frac{I_{sc0}}{G_0} \left(\sum_{i=1}^{N_p} G_i + \alpha \sum_{i=1}^{N_p} G_i \Delta T_i \right) \quad (4.4)$$

Equations 4.3 and 4.4 can be combined to calculate the squared approximation of the I-V curve of any PV module topology. Despite the squared approximation resulting in an evident overestimation of the annual yield, it reduces the simulation time by at least two orders of magnitude, depending on the computer hardware. In the following section, the suitability of the squared approximation to make a relative comparison between different topologies is discussed.

4.4.2. VALIDITY OF THE SQUARED APPROXIMATION

The difference between the squared approximation and the actual I-V curve of a solar module is smaller for PV modules with higher fill factors. Considering that the fill factor of modern commercially available c-Si PV modules is close to 80 %, the deviations between the squared approximation and the 2-diode model for different module topologies were analysed.

The simulation results presented in this chapter were obtained assuming the c-Si solar cell parameters measured in [187]. The external parameters and the temperature coefficients of the simulated solar cells used in the squared approximation are summarised in Table 4.2.

η_0	FF_0	I_{sc0}	V_{oc0}	α	β	δ
(%)	(%)	(A)	(V)	(1/K)	(mV/K)	(mV)
19.48	79.5	9.345	0.638	0.0005	-1.9	27.2

Table 4.2: External parameters and temperature coefficients of the simulated solar cells.

A comparison between the DC yield obtained using the 2-diode equivalent model and the squared approximation for different module layouts is presented in Figure 4.5a for BPD topologies and in Figure 4.5b for SP topologies. The results correspond to the

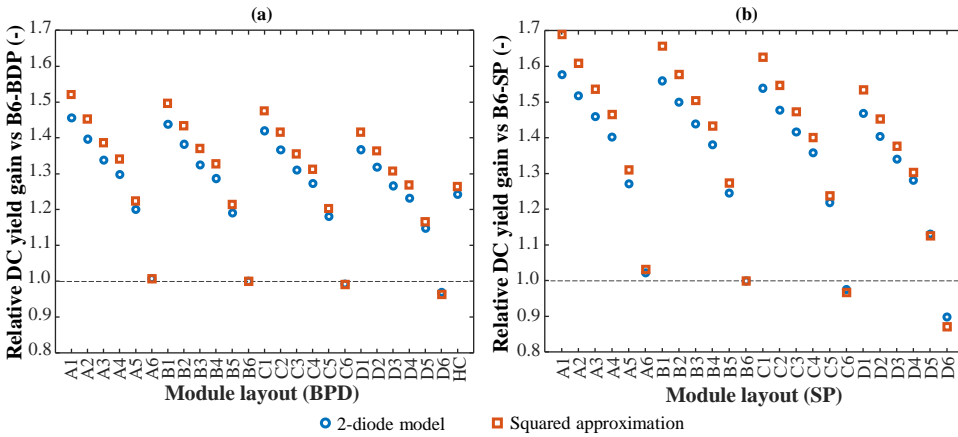


Figure 4.5: Relative DC yield gain relative to module layout B6 for the most shaded PV module on RT1 in Rotterdam. (a) Comparison between BPD topologies and layout B6-BPD. The plot also shows a comparison between the half-cell module (HC) and topology B6-BPD. (b) Comparison between SP topologies and layout B6-SP.

most shaded module in the array in Figure 4.3b using climate data for Rotterdam. This module is subject to partial shading about 50 % of the time in the year. Blue circles in Figure 4.5 refer to simulations performed with the 2-diode electrical model, whereas orange squares refer to simulations performed using the squared approximation. In this case, results indicate that most module topologies would perform significantly better than the conventional topology. For example, the plot in Figure 4.5a shows that, according to the 2-diode model, the annual DC yield of the most shaded module can be boosted almost by 45 % when using modules with one bypass diode per cell (A1-BPD) compared to a conventional module (B6-BPD). It can also be noticed that, since shadows on the analysed position on the roof mostly move from left to right on the surface of the solar module, module D4-BPD, which also has 3 bypass diodes, and the half-cut cell module (HC) can deliver about 25 % more energy than B6-BPD, which exemplifies the importance of the mounting orientation. The relative gain calculated with the squared approximation correlates well with the results from the 2-diode model. Deviations are larger for the best-performing module topologies, yet the maximum deviation (module A1-SP) is only 11.3 % in Figure 4.5b.

Figure 4.6 gives a better picture of the deviations between the squared approximation and the 2-diode model. Since the squared approximation is only intended to make relative comparisons between topologies, ideally, the deviation for all the BPD and SP layouts should be the same but not necessarily zero. In Figure 4.6, layout D6 left aside³, the dispersion of deviations between BPD topologies is roughly 5 % (from A1-BPD to C6-BPD) and between the SP topologies is about 9 % (from A1-SP to C6-SP). It should be noted that the deviations in the SP case are larger than in the BPD case because the

³Both modules D6-BPD and D6-SP have all their solar cells connected in series (with no bypass diodes) and in practice partial shading would cause hot-spots and permanent damage of the PV module, hence this is not a configuration of interest.

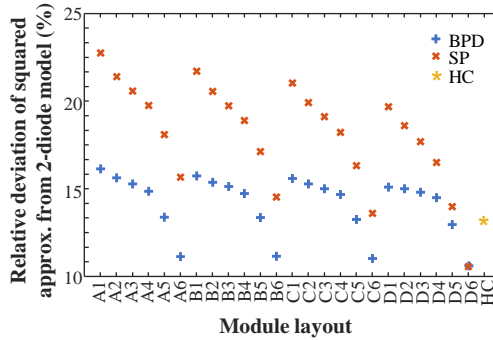


Figure 4.6: Relative deviation between the squared approximation and the 2-diode equivalent model in the worst-case scenario (the most shaded PV module on RT1 in Rotterdam).

difference between the squared approximation and the actual I-V curve of a partially shaded module increases with the number of parallel-connected solar cells.

It is important to mention, that plots in Figures 4.5 and 4.6 were generated considering the worst-case scenario, i.e. the most shaded PV module on the array. If instead the least shaded PV module in the array in Figure 4.2b is considered, which is shaded only 6 % of the year in Rotterdam, deviations range between 21.2 % and 21.7 % for BPD layouts and between 22.3 % and 24.9 % for the SP layouts. This means that the maximum difference between the squared approximation and the 2-diode model is only 0.5 % and 2.6 % for the BPD and SP layouts, respectively. Consequently, if the yield increase of entire PV systems in Figure 4.2 is evaluated, the deviations introduced by the squared approximation are expected to be between those of the most and least shaded modules.

4.5. RESULTS AND DISCUSSION

The squared approximation was applied to compare different PV systems and module topologies based on the case studies presented in the previous section.

4.5.1. STRING INVERTERS VS MLPE

The energy yield of PV systems with string inverters was compared to PV systems with MLPE (i.e., micro-inverters or power optimisers) to quantify the benefits of performing MPPT at module level. For the PV systems with a string inverter, a typical inverter with 3 independent string inputs was considered. The yellow dashed lines in Figure 4.2 indicate which modules are connected in series forming the 3 strings in each of the analysed PV installations. Furthermore, it was considered that each PV module has at least one bypass diode and that the string inverter can independently maximise the power of each string. On the other hand, the energy yield of the PV systems with MLPE was calculated considering that the power output of each PV module is independently maximised by a dedicated converter. For the sake of generality, it was assumed that the conversion efficiency of both type of converters was 100 %.

The energy yield increase obtained in Rotterdam when replacing the string inverter by MLPE is shown in Figure 4.7 for the layout family B (refer to Figure 4.3). Results in-

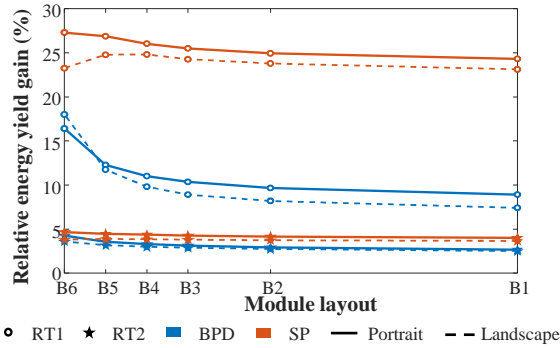


Figure 4.7: Relative energy yield gain in Rotterdam, the Netherlands, when replacing a string inverter by module level power electronics in the installations in Figure 4.2. Layouts on the horizontal axis are spaced according to the corresponding number of bypass diodes or parallel groups of cells.

indicate a significant energy yield boost when using MLPE, especially for the installations on the most shaded rooftop (RT1). It can also be noticed that, for the same installation, the gain is always higher for SP topologies compared to BPD topologies because a partially shaded string of modules with parallel interconnections presents higher current mismatch losses than a string of modules with bypass diodes. Moreover, the clear decreasing trends in the BPD curves suggest that more shading tolerant PV modules (i.e., modules with more bypass diodes) can reduce the energy yield gap between systems with string inverters and systems with MLPE. In essence, increasing the number of bypass diodes per module is an effective approach to increase the shading tolerance of a PV system with a string inverter. On the other hand, the absence of a clear decreasing trend in the SP curves, suggests that MLPE is crucial to benefit from the improved shading tolerance offered by series-parallel module topologies.

4.5.2. PV SYSTEMS WITH MLPE

When PV modules are connected in series forming a string, the shading tolerance of the PV system is strongly constrained by the current mismatch between modules, regardless of the PV module topology. Instead, in PV systems with MLPE the shading tolerance of the PV system is mainly limited by the shading tolerance of the PV module topology. Thus, PV systems with MLPE were further analysed to evaluate the potential of different module topologies.

Figure 4.8 presents a comparison of the annual DC yield gain obtained with different BPD module layouts in landscape orientation in different shading scenarios and locations. It can be noticed from the results in Figure 4.8 that the conventional PV module (B6-BPD) is one of the poorest performing module topologies when a system is affected by partial shading. In particular, when shading objects are close to the PV modules as in RT1, increasing the number of bypass diodes can significantly increase the yield of a PV system, even at locations close to the Equator like Bogotá. In contrast, when shading is caused by large distant objects as in RT2, shadows are generally larger than the dimensions of a PV module, hence solar modules are rarely partially shaded. In such cases,

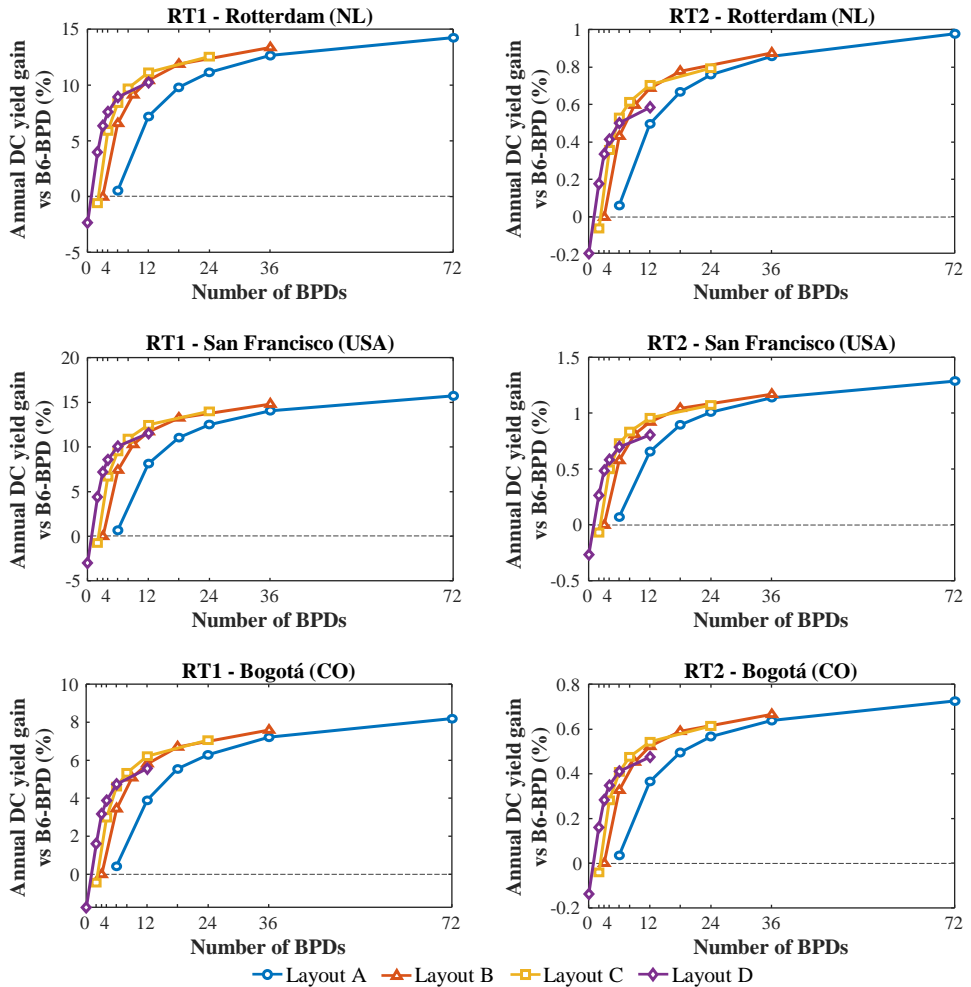


Figure 4.8: Annual DC yield comparison for various BPD topologies. Results correspond to the case when modules are mounted in landscape orientation. The vertical axis in the plot indicates the energy yield increase with respect to the systems with B6-BPD modules.

MLPE provide sufficient shade resilience to the PV systems and using different module topologies can only marginally increase the annual DC yield.

A clear tendency can be identified in the plots in Figure 4.8: the electrical performance of the system rapidly improves when adding bypass diodes but the trend flattens out around 12 diodes. For example, in RT1 in Rotterdam, 3 out of 4 topologies with 12 bypass diodes can boost the annual yield by 10% compared to the conventional PV module, whereas a system with modules with 72 diodes (one per cell) can only produce 4% additional energy. The reason why the trends start to flatten out around 12 BPDs is that all layouts with more than 12 groups of cells have at least two horizontal and two vertical

divisions (see Figure 4.3) which already provides them with high shading tolerance regardless the shape and direction of the shadows. In other words, for the analysed layouts and shading scenarios, increasing the granularity to more than 12 groups contributes only to a slight improvement in the system performance.

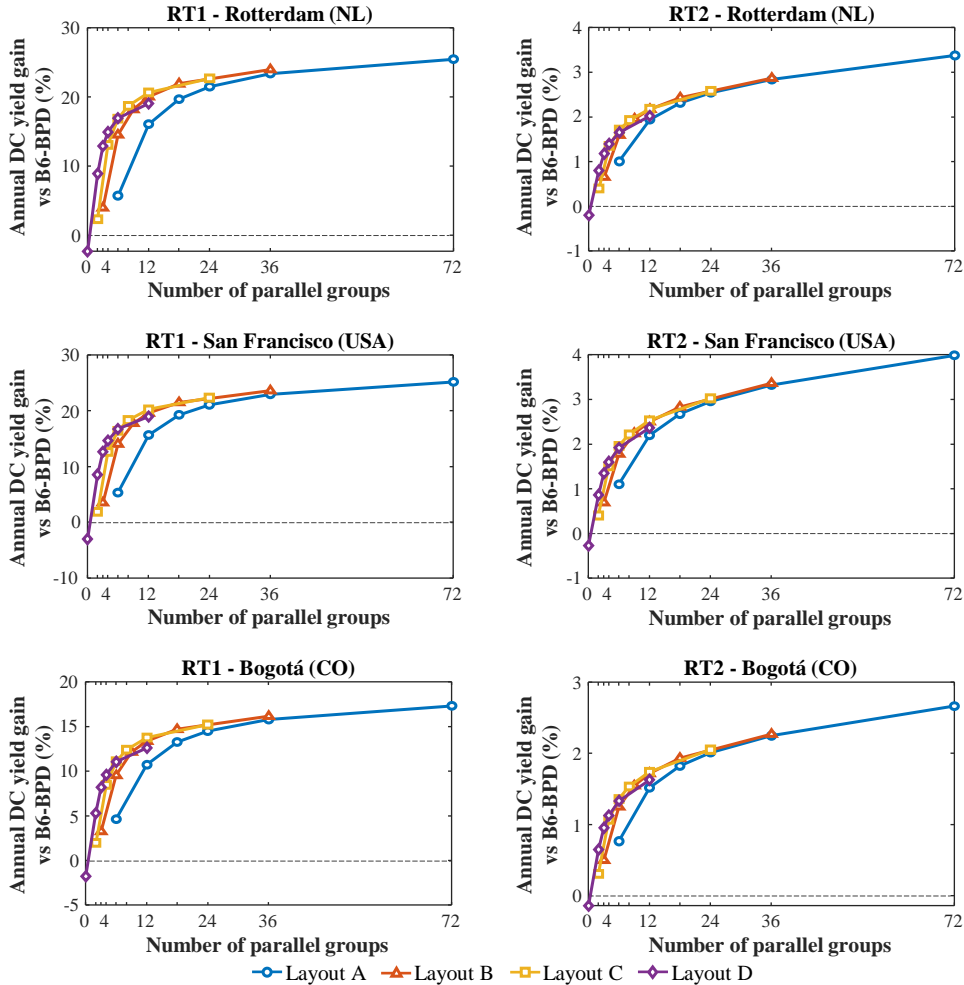


Figure 4.9: Annual DC yield comparison for various SP topologies. Results correspond to the case when modules are mounted in landscape orientation. The vertical axis in the plot indicates the energy yield increase with respect to the systems with B6-BPD modules.

It is worth mentioning, that the results in Figure 4.8 were obtained considering ideal bypass diodes (i.e., zero forward voltage drop). This approximation is highly accurate for modules with active bypass diodes [185]. However, adding too many bypass diodes can become disadvantageous when the forward voltage of the diodes is comparable to the voltage of the solar cell at the maximum power point. Losses in bypass diodes could be

easily included in the proposed approximation by modifying Equation (4.3).

Similar conclusions as for the case of landscape mounting can be drawn from the simulation results of systems with modules mounted in portrait. The main difference is that, in opposition to the landscape mounting case, A and D are the best and worst performing layout families, respectively. The reason is that shadows on the rooftops progress from left to right and in certain layouts bypass diodes are activated progressively, minimising the number of solar cells that are bypassed when the module is partially shaded. From another standpoint, layouts B and C are the best options when the shading direction is unknown.

A comparison of SP topologies is presented in Figure 4.9. Whereas the general trends are similar to those in Figure 4.8, series-parallel modules in scenario RT1 can boost the gain about 10 % more than modules with series-connected cells and bypass diodes. The trends in Figure 4.9 also flatten out for modules with more than 12 groups connected in parallel for the same reason as in Figure 4.8. In this case, more parallel-connected groups imply modules with lower output voltage and higher output current. While this could be problematic for the design of power converters, in practice, series-parallel modules can be built following the approach of the Tessera module [167], where each cell is cut into smaller sub-cells to reduce the string's current and increase its voltage.

Finally, the yield of systems with half-cut cell modules was also simulated. The DC yield gains compared to the conventional module are summarised in Table 4.3. Results indicate that, in terms of shading tolerance, half-cut cells already represent a significant improvement with respect to conventional modules, yet there is still room for improvement.

	RT1 portrait (%)	RT1 landscape (%)	RT2 portrait (%)	RT2 landscape (%)
Rotterdam	7.4	10.2	0.83	0.71
San Francisco	6.8	10.0	0.87	0.90
Bogotá	6.3	6.1	0.55	0.58

Table 4.3: Relative DC yield gain of PV systems with half-cut cell modules compared to PV systems with conventional modules (B6-BPD).

Certainly, improving the shading tolerance has an impact on the cost of PV modules. On the one hand, more bypass elements per module, especially active bypass elements with low voltage drops, imply higher material costs and introduce more peaks in the P-V curve, which might require the implementation of advanced maximum power point tracking techniques in power converters. On the other hand, the design of series-parallel modules might require cutting the solar cells into smaller pieces and design of dedicated power converters able to operate in different voltage and current ranges. The procedure proposed in this chapter allows us to find the (Pareto) optimal module granularity, meaning a point in which increasing the number of groups (thus the granularity) could lead to only a slight improvement of the performance while significantly increasing the complexity, and likely the cost, of the PV module. The trends presented in Figures 4.8

and 4.9 can allow PV module manufacturers to make more thorough cost-benefit analyses of different module topologies. Moreover, the proposed methodology can be used to simulate PV module topologies that differ from the ones presented in this chapter. Therefore, the same analysis can be replicated for any PV module topology of interest. Finally, a quick comparison between different module topologies is beneficial also for PV system designers to choose among available PV modules, and PV module manufacturers dealing with the design/need of custom, installation-specific, PV modules.

4.6. CONCLUSIONS

Shading tolerant PV modules are essential to increase the yield of urban PV systems and maximise the usable surface area for PV in urban environments, where partial shading is ubiquitous.

In this chapter, a method was introduced to compare the annual DC yield of PV systems with different PV module topologies, which enables quick sub-hourly electrical simulations of PV systems by reducing the simulation time required by the equivalent electrical model by two order of magnitude. This method allowed us to evaluate 49 different module topologies, including some that are already commercially available, in different shading scenarios and climates.

The comparison between different PV system architectures indicated that when partial shading is caused by objects that are far from the PV modules, module-level power electronics are sufficient to provide high shading tolerance to a PV system. However, when shading is caused by nearby objects, the module topology plays a determinant role in the electrical performance of the PV system.

The simulation results of module topologies in systems with module-level power electronics suggested that PV modules with one bypass element per cell can deliver between 8 % and 15 % more energy than a conventional module depending on the location, given that the voltage drop on the bypass element is sufficiently low. Series-parallel topologies can improve the performance even more, increasing the yield up to 25 %. In addition, it was estimated that half-cut cell modules, which are becoming increasingly popular, allow partially shaded urban PV system to generate between 6 % and 10 % more energy in a year than conventional PV modules. Finally, the evaluation of the annual DC yield gain as a function of the number of bypass elements and groups of parallel strings in a PV module topology resulted in clear trends that can be valuable to PV module manufacturers when performing cost-benefit analyses of new shade resilient PV module topologies.

5

A SERIES-PARALLEL RECONFIGURABLE PV MODULE

This chapter is based on the following publications:

A. Calcabrini, M. Muttillio, R. Weegink, P. Manganiello, M. Zeman, O. Isabella, *A fully reconfigurable series-parallel photovoltaic module for higher energy yields in urban environments*, *Renewable Energy* **179**, 1 (2021).

A. Calcabrini, M. Muttillio, M. Zeman, P. Manganiello, O. Isabella, *Experimental evaluation of the electrical performance of a fully reconfigurable series-parallel PV module*, *Nature Communications*, (Under review).

5.1. INTRODUCTION

As discussed in the previous chapter, under partial shading conditions parallel interconnections between solar cells help to reduce irradiance mismatch losses. However, under uniform illumination parallel connected strings generate high currents which cause high resistive and power conversion losses. To leverage the advantages offered by both types of interconnections, the concept of reconfigurable PV generators can be utilised to adapt the electrical topology of the system according to the illumination conditions. By modifying the interconnections between individual solar cells within a module or between modules, reconfigurable PV generators can optimise the electrical performance of the system under varying illumination conditions.

This chapter presents a reconfigurable PV module designed to improve the energy yield of PV systems when partial shading cannot be avoided. Moreover, a reconfiguration strategy is proposed to dynamically resolve the interconnections in the module according to the prevailing illumination conditions. Subsequently, the electrical performance of the proposed reconfigurable is simulated and compared to that of PV modules with the same cell layout but different electrical interconnections. Finally, a full-scale

prototype of the reconfigurable PV module is presented and its performance is evaluated under different shading scenarios in the field.

5.2. RECONFIGURABLE PV GENERATORS

A reconfigurable PV generator is a photovoltaic system that can dynamically adjust its electrical interconnections to reconfigure the arrangement of solar cells or modules in response to changes in the illumination levels or shading patterns [188], [189]. This enables the system to maximise the output power in situations where the illumination distribution on the system is uneven.

Reconfigurable PV generators require a switching matrix that enables the system to alternate between series connections (to minimise resistive and power conversion losses under uniform illumination conditions) and parallel connections (to minimise mismatch losses under partial shading). The switching matrix is controlled by an algorithm that dynamically adapts the system configuration according to the illumination conditions.

Most of the literature on reconfigurable PV generators is focused on reconfiguration at array level for commercial or utility scale systems. Reconfigurable PV arrays are usually based on total-cross-tie (TCT) [190]–[192] and series-parallel (SP) [193], [194] architectures. However, in urban environments, where the nature of shading is much more complex, reconfiguration needs to be implemented at sub-module level to minimise irradiance mismatch losses [195], [196].

The implementation of a reconfigurable PV module involves the development of a reconfiguration matrix and a suitable power converter. Naturally, this implies higher costs compared to a module with fixed interconnections. However, reconfigurable PV modules aim to compensate the higher costs by boosting the energy yield and mitigating module ageing and degradation effects, e.g., by disconnecting faulty cells in the module. For example, the reconfigurable module design presented in [196] could deliver 5% to 10% more energy than a conventional PV module with 3 bypass diodes, according to a simulation study considering different degrees of shading and constant power conversion efficiencies. The additional cost of a reconfigurable PV module and its power converter is roughly estimated between €16 and €20 [196]. Considering the current prices of conventional PV modules and module-level power converters, this means that a reconfigurable module could cost around 6% to 8% more than a conventional module. However, the electrical performance of reconfigurable PV modules should also be compared with shade tolerant fixed module topologies under realistic conditions to make a more equitable evaluation of their potential.

5.3. THE SERIES-PARALLEL RECONFIGURABLE PV MODULE

The general schematic of the reconfigurable PV topology proposed and investigated in this chapter is presented in Figure 5.1. It is considered that one module consists of b blocks of cells, where each block consists of c solar cells connected in series, resulting in a total of $b \cdot c$ cells per module.

The switches in Figure 5.1b constitute a switching matrix that connects the blocks in series and (then) in parallel to obtain different series-parallel module configurations.

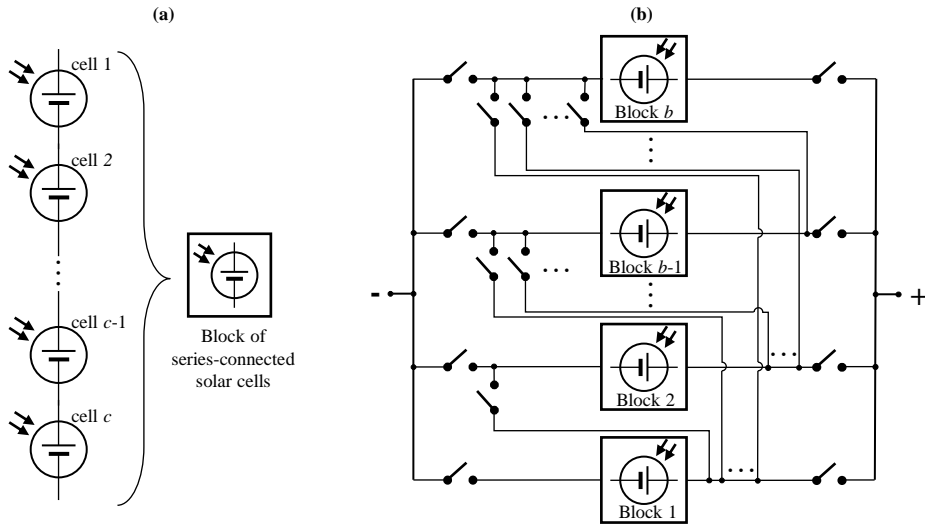


Figure 5.1: Reconfigurable series-parallel PV module. (a) One block of c solar cells connected in series. (b) Generic diagram of a fully reconfigurable series-parallel PV module with b blocks.

Any reconfigurable module can adopt a number of different electrical configurations. The configurations of interest (COI) are defined as the subset of all possible electrical configurations which can result in different I-V curves. In a fully reconfigurable series-parallel PV module with b blocks of cells, the number of configurations of interest is given by:

$$COI = \sum_{(s,p)} \frac{b!}{p!(s!)^p}, \quad b, s, p \in \mathbb{N} \wedge s \cdot p = b \quad (5.1)$$

where s stands for the number of blocks connected in series forming a string and p represents the number of strings connected in parallel. Thus, (s, p) are all possible sorted pairs of natural numbers which, when multiplied together equal the number of blocks, b . For example, a reconfigurable module with 4 blocks has 5 configurations of interest because the pair (s, p) can adopt 3 different values (1,4), (2,2) and (4,1). It is worth noting that Equation (5.1) is also valid for fully reconfigurable total-cross-tied topologies [190].

A straightforward way to improve the shading tolerance of a reconfigurable module is by increasing the number of blocks [196]. However, the number of switches required to build a fully reconfigurable series-parallel module increases quadratically with the number of blocks:

$$\#\text{switches} = \frac{b(b+3)}{2} \quad (5.2)$$

Equation (5.2) imposes cost and complexity limitations to the design of the switching matrix. Other practical limitations on the design of a reconfigurable PV module to be considered are: (1) the maximum drain-to-source voltage that the switches can tolerate; (2) the maximum allowable continuous drain current of each switch; (3) the maximum

number of solar cells per block, which is in turn limited by the reverse characteristics of the solar cells. Aiming to build a reconfigurable PV module prototype with commercially available components, the proposed module design consists of 96 solar cells, grouped in 6 blocks as shown in Figure 5.2.

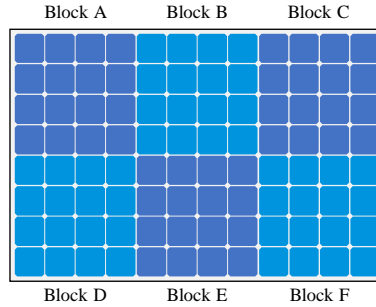


Figure 5.2: Layout of the studied reconfigurable module. The module is organised in 6 blocks ($b = 6$), indicated in different shades of blue) of 4 by 4 solar cells connected in series. The positive and negative terminals of each block are connected to the inputs of the switching matrix in Figure 5.1b.

5

According to Equation (5.1), a reconfigurable PV module with 6 blocks can adopt 27 different configurations: (1) one configuration where all blocks are connected in parallel (s1p6); (2) fifteen configurations where three duplets of series-connected blocks are connected in parallel (s2p3); (3) ten configurations where two triplets of series-connected blocks are connected in parallel (s3p2); and (4) one configuration where all the blocks are connected in series (s6p1). All possible configurations are illustrated in Figure 5.3.

The switching matrix for the proposed module with 6 blocks has 27 switches. In the general schematic presented in Figure 5.1b, all the switches that connect the blocks to the positive and negative terminals can be implemented with a single MOSFET. However, the remaining switches must be bidirectional to prevent shorting blocks of cells through the MOSFET's body diodes.

5.3.1. RECONFIGURATION ALGORITHM

Several algorithms have been proposed to control switching matrices [197] in reconfigurable PV modules and arrays. Some algorithms require periodical I-V curve tracings of each block of cells [198]. Yet in some cases, it is possible to control the switching matrix using only current measurements from each block of cells. For most c-Si solar cells technologies, the short-circuit current of each block can be considered approximately proportional to the irradiance incident on the least illuminated solar cell in the block. Temperature and voltage measurements can eventually be used, on a second level, to improve the robustness of the algorithm [199].

In this work, a simple algorithm based only on current measurements is proposed. The algorithm requires a current sensor to be connected in series to each block of cells in Figure 5.1a to measure the short-circuit current of each block and estimate the irradiance incident on each block of cells. Current measurements can be dynamically processed by the algorithm that decides which is the optimal module configuration and

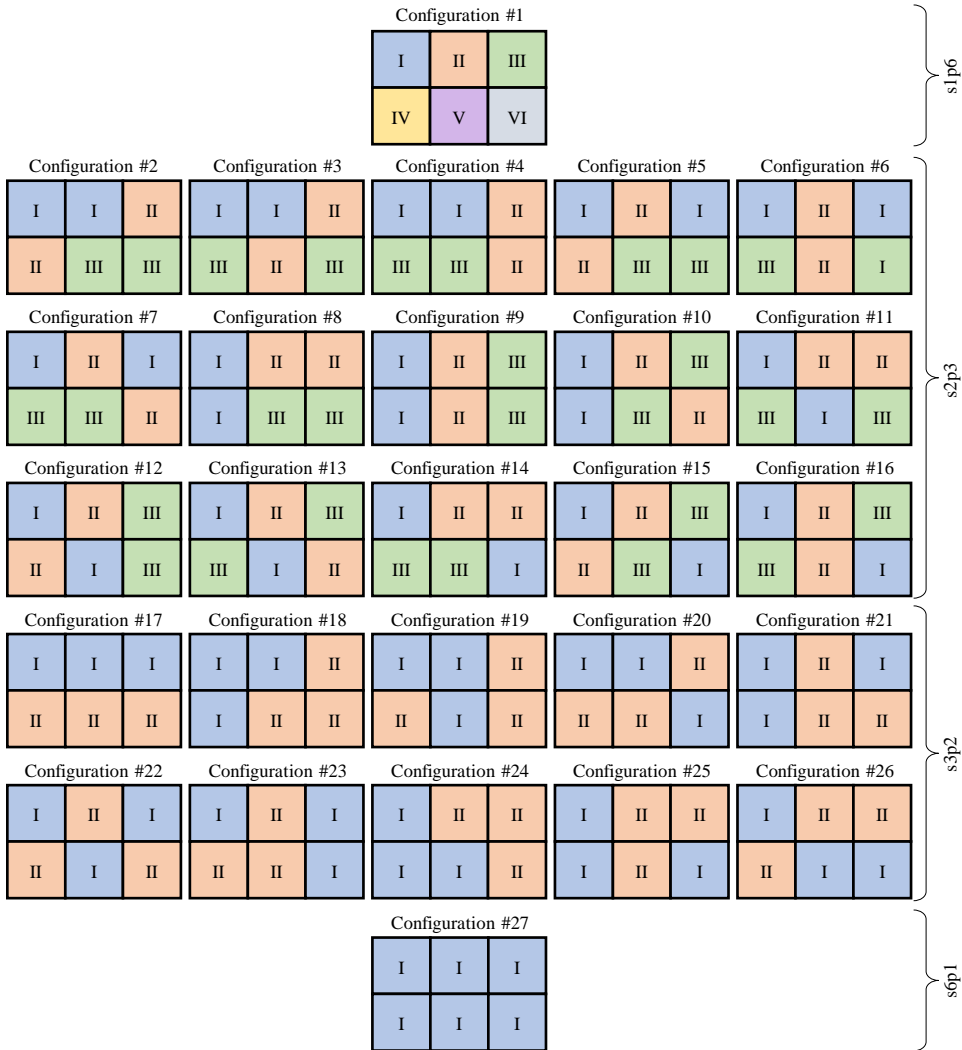


Figure 5.3: Configurations of interest of the proposed PV module with 6 reconfigurable blocks. Numbers represent blocks that are connected in series with each other. Configuration 1 is also referred to as s1p6 or all-parallel. Configurations 2 to 16 are the 15 possible s2p3 configurations. Configurations 17 to 26 are the 10 possible s3p2 configurations. Configuration 27 is also referred to as s6p1 or all-series.

which switches need to be closed. In essence, the algorithm aims to connect equally illuminated blocks of cells in series, for which it compares the measured short-circuit currents with three predefined threshold constants that are used to determine the optimal module configuration.

The proposed algorithm is depicted in Figure 5.4. It begins by measuring the short-circuit current of all six blocks of cells (I_A to I_F). Then, these currents are sorted in de-

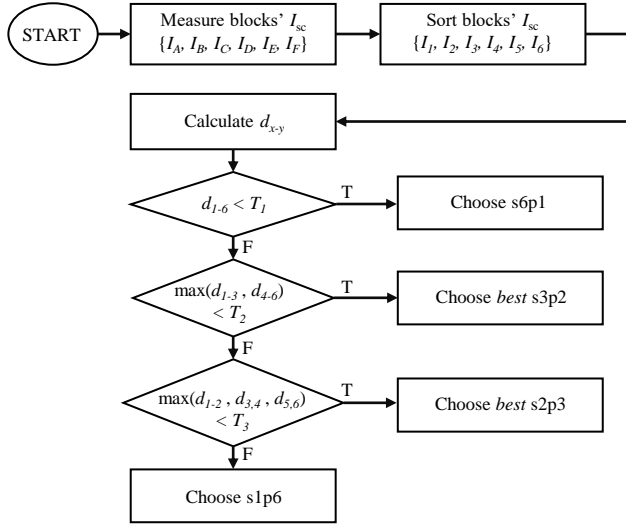


Figure 5.4: Block diagram of the proposed reconfiguration algorithm. In every iteration of the algorithm, the currents of the blocks (named from A to F) are sorted in descending order and then renamed from 1 to 6. According to the notation convention, I_1 represents the highest measured current while I_6 represents the lowest measured current.

scending order and renamed from I_1 to I_6 to calculate six relative differences between the sorted currents, namely d_{1-6} , d_{1-3} , d_{4-6} , d_{1-2} , d_{3-4} and d_{5-6} , where:

$$d_{x-y} = \frac{I_x - I_y}{I_x} \quad (5.3)$$

Next, d_{1-6} is compared to a first threshold value T_1 . If the maximum irradiance deviation between all the blocks (d_{1-6}) is lower than T_1 , it means that all blocks are similarly illuminated; thus, all the blocks are connected in series (configuration s6p1). Otherwise, the largest difference between the sorted triplets of currents (d_{1-3} and d_{4-6}) is compared to threshold T_2 . If both d_{1-3} and d_{4-6} are smaller than T_2 , the best s3p2 configuration is chosen. It is considered that the best s3p2 configuration (among the 10 possible) is determined by the order of the sorted currents. For instance, if the order of the sorted currents is $\{I_B, I_C, I_E, I_F, I_A, I_D\}$, then the best s3p2 configuration has one string formed by groups B, C and E connected in parallel to a second string formed by F, A and D. If a solution is not yet found, the algorithm checks if the largest difference between the sorted duplets of currents (d_{1-2} , d_{3-4} and d_{5-6}) is smaller than threshold T_3 and, if so, it chooses the best s2p3 configuration (also determined by the order of the sorted currents). Finally, if all differences are larger than the established thresholds, configuration s1p6 is chosen and all groups are connected in parallel. In this study, the threshold values were decided based on an optimisation process which considers the electrical characteristics of the solar cells. However, these thresholds could also be adjusted considering the efficiency of the power converter to favour the operation of the reconfigurable PV module in specific voltage and current ranges.

The proposed algorithm is adaptable to reconfigurable modules with different numbers of blocks. For example, for a module with 8 blocks, 4 sets of configurations would be possible ($1 \times s1p8$, $105 \times s2p4$, $35 \times s4p2$ and $1 \times s8p1$). In this case, the algorithm would require 3 threshold values and the calculation of 7 relative differences (d_{1-8} , d_{1-4} , d_{4-8} , d_{1-2} , d_{3-4} , d_{5-6} and d_{7-8}).

It is worth noting that short-circuit measurements represent only a single point of the I-V curves of each block and thus, even when current measurements are free of noise, the proposed algorithm cannot always ensure that the chosen configuration is actually the best one. Additionally, the proposed algorithm relies on the assumption that the current at the maximum power point of a block of cells is affected by shading in the same proportion as its short-circuit current. This is an acceptable assumption as long as the number of series-connected cells per block is relatively small and the breakdown voltage of the solar cells is sufficiently large. However, as discussed in detail in Chapter 6, if the number of series-connected cells per block is large enough to build up a voltage that can force the current to flow through a single reverse biased cell, the short-circuit current of the block may be reduced in a much smaller proportion than the current at the maximum power point. Consequently, the proposed algorithm may not be appropriate for certain module topologies or solar cell technologies. More specifically, a reconfiguration algorithm based solely on current measurements may prove insufficient for commercial module topologies that consist of 3 sub-modules with 24 series-connected solar cells, and for PV modules with low-breakdown voltage solar cells.

It is also evident that the performance of the reconfigurable module depends on the values of the thresholds T_1 , T_2 and T_3 . Higher threshold values increase the tendency of the algorithm to avoid the all-parallel configuration, which leads to lower output currents. At the same time, higher threshold values imply a lower shading tolerance. This trade-off brings out the importance of the choice of threshold values for the algorithm.

Furthermore, there are two additional practical aspects that should be considered when selecting the threshold values. First, threshold values must be larger than the relative measurement error of the current sensors. Second, in the case of reconfigurable PV modules with bypass diodes, the threshold values should be smaller than the relative difference between the maximum power point current and the short-circuit current of the solar cell to avoid choosing configurations with more than one maximum in the P-V curve.

In its simplest version, the interval between reconfiguration events in the algorithm is fixed and typically ranges between 1 and 5 minutes. As a result, the expected variations in the power output of a reconfigurable PV module in timescales shorter than 1 minute (e.g. due to rapid changes in irradiance expected during a partially cloudy day) are the same as for PV modules with fixed interconnections.

A synchronous (i.e. scheduled) reconfiguration algorithm induces unnecessary operational disruptions in the power converter, especially during prolonged periods of uniform illumination conditions. To reduce the frequency of interruptions, it is possible to employ a shade detection algorithm that triggers reconfiguration events when deviations in the operating state of the module or block are detected. For instance, shade detection algorithms may be implemented through either the utilisation of current and voltage sensors within the reconfiguration board [200], or by processing the current and

voltage measurements taken by the Maximum Power Point Tracking (MPPT) algorithm within the power converter [201].

In addition, it is important to point out that, under specific circumstances, a fixed time interval between reconfiguration events could potentially cause hot-spots. For example, if the reconfigurable module is being operated in the all-series and a single cell is totally shaded, the shaded cell could be forced to dissipate a large amount of power until the next reconfiguration event. This problem can be avoided by adding a bypass diode in parallel to each reconfigurable block. Alternatively, the algorithm can be modified to constantly monitor the operating voltage of each block of cells, and generate a hardware interrupt if the voltage of one of the blocks suddenly drops. In turn, the interrupt service routine would trigger a new reconfiguration event which would find a module configuration where the shaded cell is not reversed biased.

5.4. ENERGY YIELD SIMULATION

The additional complexity and cost of a reconfigurable PV module topology compared to fixed module topologies could be justified if the energy yield of the reconfigurable PV module is significantly higher. In this section, the potential of a reconfigurable module is assessed by comparing its annual DC yield to that of two fixed module topologies.

5.4.1. SIMULATION FRAMEWORK

The energy yields were compared with a simulation framework comprising three widely validated models: (1) an irradiance model to determine the irradiance incident on the solar cells; (2) a thermal model to determine the cell temperature, and (3) an electrical model to calculate the PV module's I-V curve.

The irradiance on each cell was simulated using *Radiance* constrained to 2 ambient bounces as explained in Chapter 3. For simplicity, it was assumed that all the surfaces surrounding the PV modules were Lambertian reflectors with an average reflectivity of 0.15.

The cell temperature was calculated with the Faiman model [179] considering that the modules were mounted close to a rooftop. The irradiance and wind parameters of Faiman model used in this work ($u_0 = 14.4 \text{ W m}^{-2} \text{ K}^{-1}$ and $u_1 = 34 \text{ mW m}^{-3} \text{ s}^{-1} \text{ K}^{-1}$) were derived from the empirical coefficients reported in [180] for close roof mount. For simplicity, the Faiman model was decoupled from the electrical model by assuming (only for the thermal calculation) that each cell was operated at its maximum power point (MPP).

The cell temperature and irradiance were combined to calculate the I-V characteristics of a solar cell using the 2-diode electrical equivalent model [181]–[183]. It was assumed that both the series (R_s) and parallel (R_p) resistances in the 2-diode model are temperature independent, and that the saturation current of the diodes varies with the cell temperature as described in [184].

The simulations were conducted considering 5-inch commercially available solar cells with a maximum power of 2.72 W under Standard Test Conditions (STC). The corresponding 2-diode model parameters given in Table 5.1, were fitted using STC and dark I-V curves measurements following the approach described in [202]. Finally, the I-V curves of the cells were combined together to calculate the I-V curves of the PV mod-

ule. In this step, the following electrical losses were included: (1) the equivalent resistance of tabbing wires (2 m Ω) calculated according to [203]; (2) the resistance of the interconnecting tabs (2 m Ω) calculated considering the length and cross-section of the ribbons; (3) conduction losses in the switches calculated assuming a constant channel resistance (2.1 m Ω for the onsemi NVMFS6H800N power MOSFET); (4) conduction losses in bypass diodes calculated using the diode's I-V characteristics at 25 °C (for the onsemi 80SQ045N rectifier). In practice, bidirectional switches were implemented with two back-to-back MOSFET, and hence, it was considered that the resistance of the bidirectional switches was twice as high as that of the unidirectional switches.

I_{ph0} (A)	n_1 (-)	I_{s1} (pA)	n_2 (-)	I_{s2} (μ A)	R_s (m Ω)	R_p (Ω)	$\alpha_{I_{sc}}$ (%/K)
5.67	1	108.9	2	5.645	2.80	20.1	+0.024

Table 5.1: Solar cell parameters at STC for the double diode model. The parameters are presented in the following order: photogenerated current, ideality factor and saturation current of the first and second diodes, respectively, series resistance, shunt resistance and short-circuit current temperature coefficient.

The shading scenario used for this study is shown in Figure 5.5. Results were analysed for the three highlighted module positions. On each of these positions, the energy yield of the proposed reconfigurable module (6REC) was simulated and compared against two module topologies with fixed cell interconnections, namely (1) a module with all 6 blocks connected in series and one bypass diode in parallel to each block (6BPD), and (2) a module with all 6 blocks connected in parallel (6SP). It was assumed each module was connected to an ideal power converter with MPPT capability was connected to the output of the PV modules.

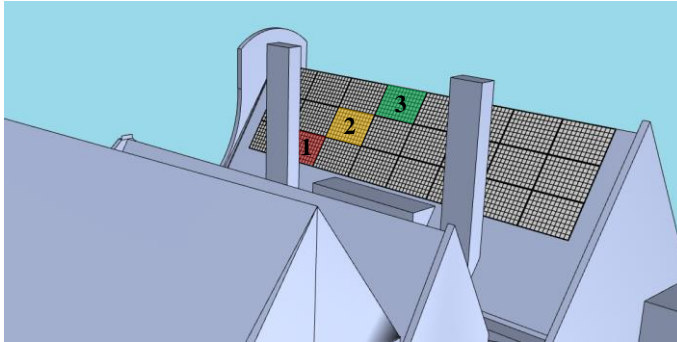


Figure 5.5: Simulated PV array. The roof is tilted 57° facing 214° east of north. The analysed PV modules are highlighted in different colours. The red module (1) is the most shaded PV module while the green module (3) is the least shaded one.

5.4.2. RESULTS

The above-mentioned models were combined to simulate the I-V curves of the different PV modules using 1-minute resolution Meeonorm climate data [176] for the city of

Utrecht, the Netherlands.

In average, in Utrecht, 35 % of the time the PV modules only receive diffuse radiation. During the periods of time with no beam irradiance, the reconfigurable PV module is expected to operate mostly in the s6p1 configuration since the irradiance distribution on the PV module surface is rather uniform. Moreover, simulations results indicate that module positions 1, 2 and 3 in Figure 5.5 are exposed to highly uneven¹ illumination during 32 %, 14 % and 7 % of the daytime hours, respectively. Therefore, the DC yield differences between the 6REC and the 6BPD module are expected to be larger at position 1. At position 3, where the module is barely affected by partial shading, all three module topologies are expected to perform similarly, but REC and 6BPD are expected to generate lower currents than 6SP.

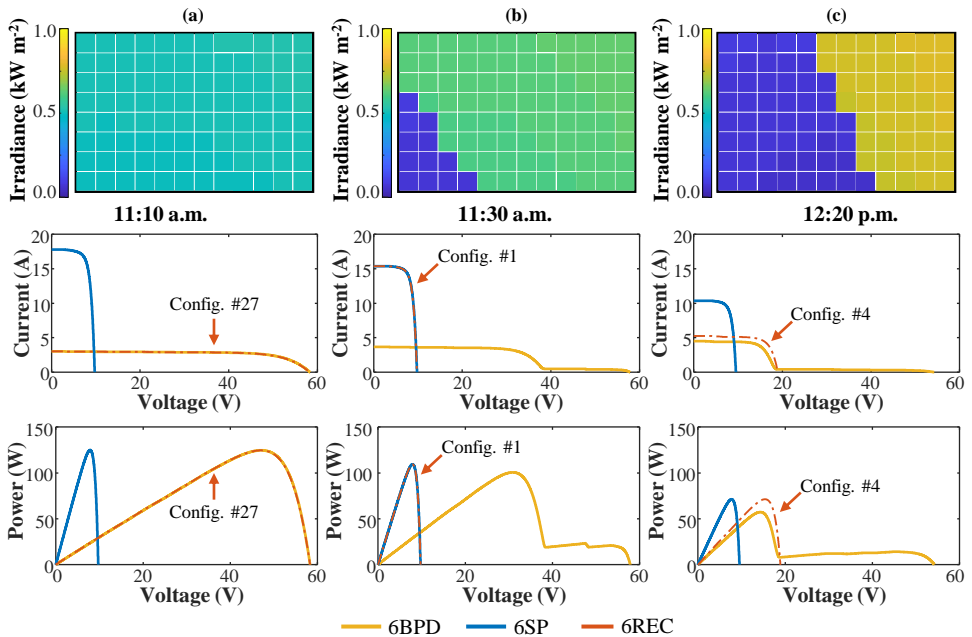


Figure 5.6: Simulation results at rooftop position 1 on April 11th at (a) 11:10 a.m., (b) 11:30 a.m. and (c) 12:20 p.m. The configuration chosen by the algorithm at each time is indicated next to the corresponding I-V and P-V curves.

Examples of the simulated I-V and P-V curves are shown in Figure 5.6 for the three types of modules at the most shaded position on the rooftop. In Figures 5.6a and 5.6b, the reconfigurable module adopted the all-series (#27) and all-parallel (#1) configurations, respectively. In Figure 5.6c, blocks C and F were unshaded and hence, the reconfigurable module adopted configuration #4, where these blocks are connected in series (refer to Figure 5.3).

The DC yield simulation results are summarised in Table 5.2. The yield of the 6BPD

¹In this context, highly uneven illumination means that the irradiance incident on the least illuminated cell in the PV module is at least 50 % lower than the irradiance incident on the most illuminated cell.

module was calculated assuming two cases: (1) an ideal MPPT algorithm that can always find the absolute MPP (6BPD ideal) and (2) a more realistic MPPT algorithm that performs an I-V scans every 5 minutes and might temporarily get stuck in local maxima. The significantly lower performance of the more realistic 6BPD module compared to the ideal case, illustrates the challenge of distinguishing between the true MPP and the local peaks in the P-V curves of modules with many bypass diodes. In Table 5.2, the yield of the 6REC module was also calculated considering two strategies to control the switching matrix: (1) an ideal reconfiguration algorithm that always finds the actual best configuration (6REC ideal) and (2) the proposed reconfiguration algorithm (6REC algorithm). In both cases, reconfiguration events were triggered at every minute.

Yield (Wh/W _p)	Position 1	Position 2	Position 3
6BPD ideal	384.80 (ref.)	622.91 (ref.)	776.67 (ref.)
6BPD 5-min scan	364.84 (-5.2%)	615.97 (-1.1%)	773.98 (-0.3%)
6SP	435.06 (+13.1%)	648.24 (+4.1%)	787.32 (+1.4%)
6REC ideal	434.13 (+12.8%)	646.45 (+3.8%)	784.91 (+1.1%)
6REC algorithm	433.74 (+12.7%)	645.97 (+3.7%)	784.68 (+1.0%)

Table 5.2: Annual specific DC yield comparison of the analysed PV module topologies in different positions on the rooftop shown in Figure 5.5 using typical meteorological year data from Utrecht, the Netherlands.

Energy yield results indicate that the reconfigurable module (6REC) with the proposed algorithm and the fixed series-parallel module (6SP) performed better than the module with 6 bypass diodes (6BPD) in all the cases. In particular, in the case of the most partially shaded rooftop position, the difference between the 6REC and 6BPD modules is 12.7%. It is worth mentioning that, although shadows are shorter in summer compared to winter, the energy yield difference between the 6SP and the 6BPD modules and between the 6REC and the 6BPD modules is larger in summer months as shown in Figure 5.7. The reason is because at the simulated location there are more clear sky days in summer than in winter months, hence modules are more frequently partially shaded.

Table 5.3 shows that the energy yield gains calculated using the same shading scenario and climate data of Barcelona are similar gains to those obtained for the city of Utrecht. Once more, in Barcelona the shadows cast by the chimneys are even smaller but there are many more clear sky days compared to Utrecht.

It is relevant to point out that that in all cases, the 6SP module achieved marginally higher yields than the 6REC module despite the expected higher resistive losses at module-level. Nevertheless, the 6SP module delivers power at significantly higher currents than the 6REC module as shown by the histograms in Figure 5.8. While the 6SP module de-

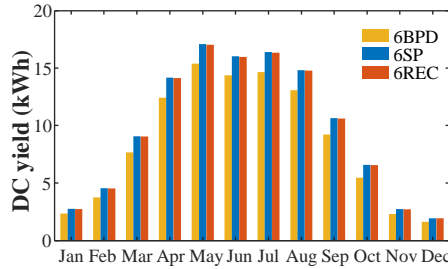


Figure 5.7: Monthly yield comparisons of the analysed module topologies on rooftop position 1 in Utrecht. It is assumed that the 6BPD module is always operated at the true MPP and that the switching matrix of the 6REC module is controlled by the proposed algorithm.

Yield (Wh/W _p)	Position 1	Position 2	Position 3
6BPD ideal	611.32 (ref.)	960.18 (ref.)	1216.93 (ref.)
6BPD 5-min scan	592.28 (-3.1%)	950.77 (-1.0%)	1214.56 (-0.2%)
6SP	690.67 (+13.0%)	1003.65 (+4.5%)	1230.73 (+1.1%)
6REC ideal	688.84 (+12.7%)	1000.25 (+4.2%)	1226.18 (+0.8%)
6REC algorithm	688.37 (+12.6%)	999.76 (+4.1%)	1225.89 (+0.7%)

Table 5.3: Annual DC yield comparison of the analysed PV module topologies in different positions on the rooftop shown in Figure 5.5 using typical meteorological year data from Barcelona, Spain.

livered currents up to 34 A, the current generated by the 6REC module at the least (Figure 5.8a) and most (Figure 5.8b) shaded rooftop positions rarely exceeded 20 A. These observations suggest that a DC-DC converter for the 6REC module would have lower input current requirements and could achieve higher conversion efficiencies than a converter for the 6SP module.

As stated before, the module configuration chosen by the algorithm can sometimes differ from the actual best configuration. Based on the design of the reconfigurable module, the characteristic of the cells and considering the trade-offs discussed in Section 5.3.1, a Pareto optimal solution was found with threshold coefficients $T_1 = 3\%$, $T_2 = 5\%$ and $T_3 = 8\%$. Figure 5.9 shows the effect of the threshold values on the annual DC yield of the PV module. As expected, lower threshold values favour the all-parallel configuration and imply a higher shading tolerance. With the mentioned threshold values, the match between the algorithm's choice and the actual best configurations varies from 51% at module position 1, to 20% at positions 2, to 13% at position 3. Even so, from the results in Table 5.2 that correspond to the 6REC modules, it can be concluded

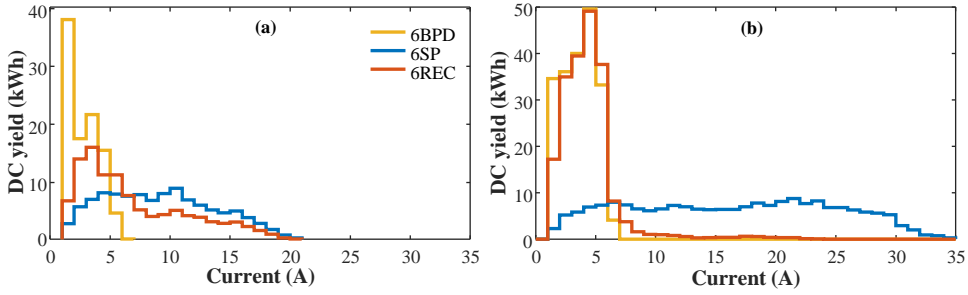


Figure 5.8: DC current distribution of the analysed module topologies in Utrecht. Histograms of the DC energy generated by the analysed module topologies as a function of the module's output current for the most (a) and the least (b) shaded positions on the rooftop. It is assumed that the 6BPD module is always operated at its MPP and that the switching matrix of the 6REC module is controlled with the proposed algorithm.

that, for all the analysed cases, with the proposed reconfiguration algorithm the module could deliver over 99.9% of the total maximum energy that could be obtained with an ideal reconfiguration algorithm.

5

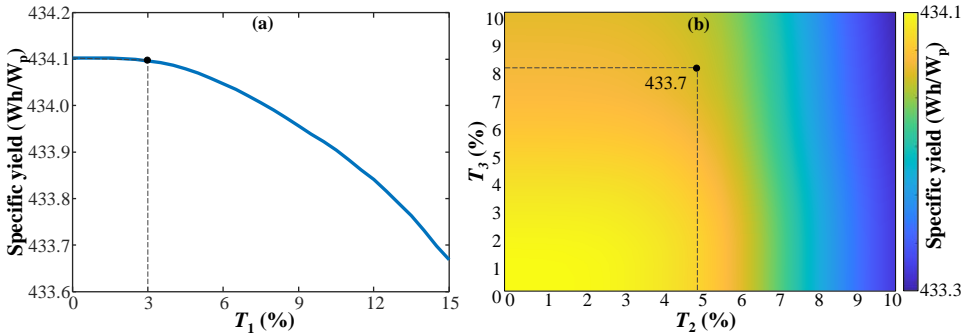


Figure 5.9: Annual energy yield of the PV module on rooftop position 1 in Figure 5.5 for different threshold values. (a) Effect of T_1 on the annual specific yield considering $T_2 = T_3 = 0\%$. (b) Effect of T_2 and T_3 on the annual specific yield considering $T_1 = 3\%$. The circles indicate the yield obtained with the chosen threshold values.

Finally, it must be reminded that in reality there are sources of partial shading that were not considered in the simulations, such as soiling, vegetation and bird droppings. Some of these shading sources can have a random effect on the irradiance distribution over the surface of the PV module. Random shading can have a disproportionate impact on the output power of modules with fixed interconnections because each block of cells is generally limited by the least illuminated cell. In these cases, the ability of a reconfigurable module to group together blocks of cells that are affected in a similar way would help to reduce the negative effects of random shading.

5.5. INDOOR EXPERIMENTAL VALIDATION

In order to validate the results presented in this chapter, a prototype of a reconfigurable module was built and tested using a A+A+A+ flash simulator. The prototype shown in Figure 5.13a consists of 6 reconfigurable blocks, each made of 16 series-connected 5-inch mono-crystalline Si solar cells with the parameters listed in Table 5.1.

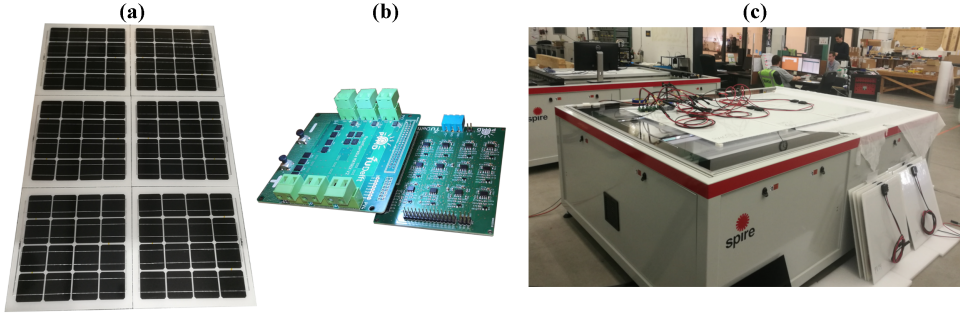


Figure 5.10: Experimental setup. (a) Prototype of the reconfigurable module with 6 blocks, each with 16 solar cells (module dimensions are 120 cm by 180 cm). (b) Prototype of the reconfiguration matrix board. (c) Reconfigurable PV module on an EternalSunSpire A+A+A+ Xenon Single Long Pulse flash simulator.

5

5.5.1. EVALUATION OF MODULE CONFIGURATIONS

The reconfiguration board shown in Figure 5.13b was designed to control the operation of the module. Although the details of the design of the electronic circuit of the switching matrix are out of the scope of this dissertation, it is important to mention that the board includes a microcontroller where the proposed algorithm was implemented and that the switches were implemented with the transistors referred in Section 5.4.1.

The board and the modules were tested at EternalSunSpire's facilities using the flasher setup shown in Figure 5.10c. From an initial characterisation at STC, it was determined that the 6 reconfigurable blocks of cells had a mismatch lower than 1% in P_{mpp} , I_{sc} and V_{oc} . Later, the blocks were connected to the inputs of the reconfiguration board and the output of the board to the electronic load of the flash tester setup. The I-V curves of the 27 module configurations were measured and simulated for the 3 shading experiments shown in Figure 5.11.

In shading experiment A, in Figure 5.11a, two blocks of cells were partially shaded with a 30% translucent foil. It was found that configurations #4, #7 and #14 (refer to Figure 5.3) were the best performing. These three configurations are all the s2p3 configurations in which the two shaded blocks are connected in series.

Figure 5.12 shows the measured and simulated I-V curves of 4 different configurations during experiment A. Results show good agreement between the measured and the simulated maximum power of each configuration. In some of the I-V curves, steps in the I-V curve are visible owing to the bypass diodes that were connected in parallel to each block of cells as a protective measure. Nevertheless, it is worth pointing out that the presented reconfigurable module can be safely operated without any bypass diodes given that the reconfiguration algorithm is robust enough to avoid hot-spots. Moreover,

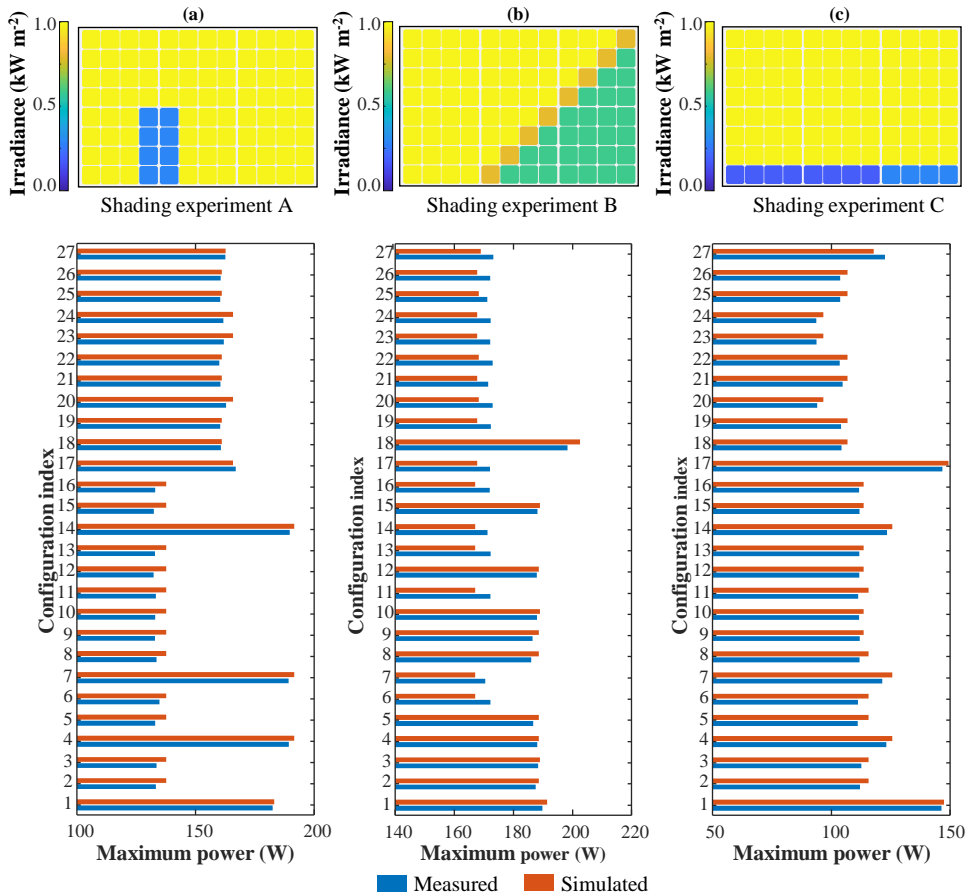


Figure 5.11: Measured and simulated maximum power of the reconfigurable PV module. The figure shows the irradiance distribution on the module as well as the simulated and measured maximum power for each of the 27 module configurations for three different shading experiments.

the addition of bypass diodes in these experiments did not affect the maximum power delivered by the optimal configuration (e.g., configuration #4 in Figure 5.12). This was further evaluated by comparing simulations of a reconfigurable module with and without bypass diodes. The comparison revealed a negligible difference in the annual yield (below 0.05 %) and confirmed that in over 99 % of the cases all bypass diodes were reverse biased at the MPP of the best module configuration.

In experiment B, corner shading was evaluated by covering 3 blocks of cells with a 60 % translucent fabric as illustrated in Figure 5.11b. In this case, both measurements and simulations indicate that the best configuration is #18 (s3p2), where blocks C, E and F are connected in series. Lastly, in experiment C, blocks D and E were shaded with a 16 % translucent foil and block F was shaded with a 30 % translucent foil, which resulted in configuration #17 (s3p2) being the best performing one.

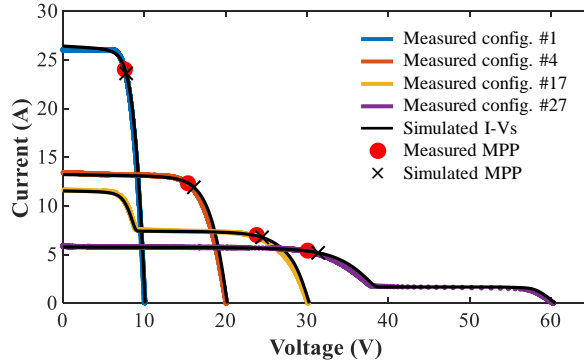


Figure 5.12: Measured and simulated I-V curves of configurations 1, 4, 17, and 27 in shading experiment A.

Despite the small mismatch between the electrical characteristics of the blocks of cells and other possible sources of error, such as small temperature differences and the non-uniformity of the shading objects, it was determined that the maximum mean absolute error in the simulated maximum power point for all the configurations was 4.0 % for shading case A, 2.7 % for shading case B and 4.4 % for shading case C. These small errors reflect the high accuracy of the simulation model described in Section 5.4.1.

5.5.2. EVALUATION OF THE RECONFIGURATION ALGORITHM

The performance of the algorithm was also evaluated for the three shading experiments in Figure 5.11. Table 5.4 presents the measured short-circuit current of blocks A to F, and compares the configuration chosen by the algorithm using the measured currents as inputs to the actual best configuration from measured I-V curves. Only in experiment B the algorithm's choice matched the actual best configuration. In experiments A and C the algorithm choose a sub-optimal configuration. On the one hand, in experiment A, configurations 4 and 14 are equivalent, and therefore the power loss was negligible. On the other hand, in experiment C the discrepancy in power was larger because the algorithm choose configuration #1 (s6p1) instead of the best performing configuration #17 (s3p2). Although the relative power loss can still be considered low (only 1.3 %), it must be noted that configuration #17 delivers lower currents than configuration #1 and it would allow a higher DC-DC conversion efficiency.

Experiment C clearly exemplifies one of the situations where the algorithm found a suboptimal configuration. In this case, increasing the value of T_2 would force the algorithm to choose the right configuration, yet it would be possible to find a different shading experiment in which a higher value of T_2 would have the opposite effect. It is therefore concluded that the proposed algorithm cannot avoid these situations using only short-circuit current measurement and the use of complementary sensors, such as voltmeters across each block of cells, could help to improve the algorithm's performance. At the same time, voltage measurements could be used to immediately identify when a single block of cells is reversed biased. Thus, the addition of voltage measurements to the reconfiguration algorithm can also ensure the safe operation of a reconfigurable module

without any bypass diodes.

	Exp. A	Exp. B	Exp. C
I_A (A)	5.81	5.81	5.79
I_B (A)	5.82	5.82	5.83
I_C (A)	5.79	3.61	5.80
I_D (A)	1.73	5.78	0.97
I_E (A)	1.70	3.58	0.92
I_F (A)	5.73	3.49	1.77
Algorithm's choice	Config. 4	Config. 18	Config. 1
Actual best choice	Config. 14	Config. 18	Config. 17
Relative power loss	-0.1%	0%	-1.3%

Table 5.4: Algorithm performance for the 3 shading experiments analysed.

It is important to consider that, in practice, the output of the switching matrix would be momentarily disconnected from the power converter during each reconfiguration event. This is needed to short-circuit the blocks and measure the short circuit current of each blocks. With the experimental prototype it was determined that the total time required to measure the short-circuit of each of the 6 blocks and run the algorithm is below 150 ms. Then, assuming minutely reconfiguration events, the annual loss in the energy yield due to reconfiguration events would be limited to 0.25%. Furthermore, additional simulation were performed to analyse the effect of the reconfiguration frequency. For the presented shading scenario, results suggested that the reconfiguration interval could be increased up to 5 minutes with a minimal impact on the DC energy yield. In particular, for the 6REC algorithm module in Table 5.2, the annual yield at rooftop position 1 would drop from 433.74 Wh/W_p to 432.89 Wh/W_p if reconfiguration events occurred every 5 minutes instead of minutely. Under slowly changing shading conditions, it is probably desirable to increase the time between reconfiguration events as it could smooth the operation of the power converter with a limited impact on the shading tolerance of the PV module.

5.6. OUTDOOR EXPERIMENTAL VALIDATION

After the initial indoor tests, the reconfigurable module was installed outdoors on the rack as shown in Figure 5.13a at the PVMD monitoring station in Delft. The performance of the PV module was monitored during 4 months using different shading profiles between May and August 2021.

Two PV modules were compared during the outdoor experiments: the reconfigurable PV module (6REC) and a reference PV module with static interconnections (6BPD). Both modules were laminated using commercial 5-inch mono c-Si solar cells from the same batch. In the reference module, the blocks were (statically) connected in series as shown in Figure 5.14a. Instead, in the reconfigurable module depicted in Figure 5.14b, the blocks of cells were connected to a switching matrix as illustrated in Figure 5.15.

The temperature of the modules was measured using T-type thermocouples attached



Figure 5.13: (a) Experimental setup at the PVMD monitoring station in Delft, the Netherlands. (b) Reconfiguration and sensing circuitry. (1) Power supply. (2) Switching matrix. (3) Driver circuit. (4) Microcontroller. (5) Temperature data logger.

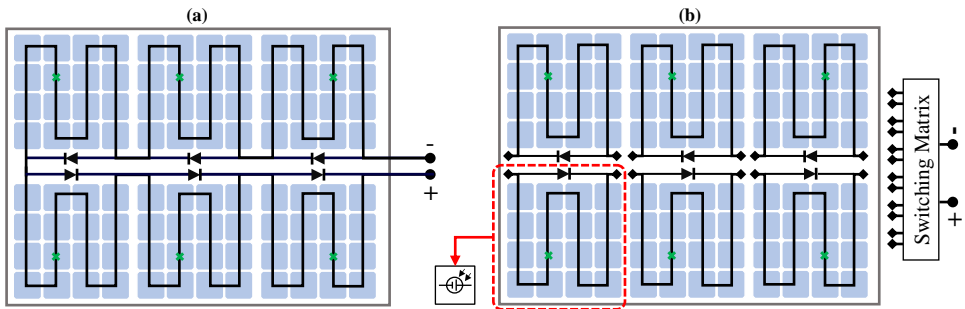


Figure 5.14: Compared PV module topologies. (a) Reference PV module with 96 solar cells connected in series and 6 bypass diodes. (b) Reconfigurable PV module with 6 blocks of series-connected cells. The positive and negative terminals of each block are connected to the switching matrix. Despite not being needed for the operation of the module, bypass diodes were included as an additional protection measure.

to the backsheet of the PV modules and thermally insulated from the air with XPS foam at the positions indicated with green crosses in Figure 5.14.

The electrical performance of the reference PV module was monitored using an LPVO MP1010F-1 MPPT tracking unit [204], which measured the I-V curve of the reference PV module at every minute and kept the PV module at its maximum power point in between I-V sweeps.

The electronics required to operate and monitor the reconfigurable PV module were installed in the electrical box shown in Figure 5.13b, which was mounted on the rear side of the rack. A microcontroller unit, where the reconfiguration algorithm explained in Section 5.3.1 was implemented, controlled the state of the MOSFETs in the switching matrix through a driver circuit. In this prototype, all the devices were powered with an external power supply. Nevertheless, the power consumption of the switching matrix is minimal and eventually it can be (self) powered with the solar cells in the PV module. The electrical performance of the reconfigurable PV module was measured using a BK8616 (B&K PRECISION) electronic DC load which was connected to the output of the switching matrix.

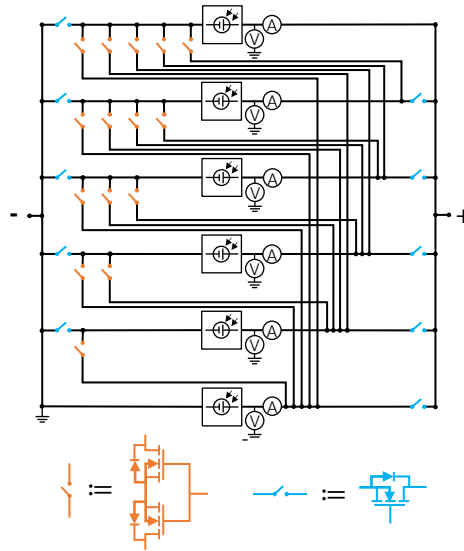


Figure 5.15: Switching matrix schematic. The current and voltage sensors were used for the reconfiguration algorithm and to measure the I-V curves of the individual blocks.

In addition, resistive voltage dividers and Hall-effect current sensors (Allegro ACS722) were included in the switching matrix to measure the voltage and current of each individual block as shown in Figure 5.15). The measurements were digitised using a 12-bit ADC and processed by an ARM core microcontroller embedded in the switching matrix. The accuracy of the current sensors ($\pm 3\%$) defines a lower bound for the value of the threshold constants in the reconfiguration algorithm ($T_1 = 3\%$, $T_2 = 5\%$ and $T_3 = 8\%$). Moreover, the current sensors introduce an additional resistance ($0.65\text{ m}\Omega$) in the path of the current of each block, which represents a 1.45% increase in the cell's equivalent series resistance presented in Table 5.1 and an additional 0.4% power loss at STC.

Only the current sensors were required for the operation of the reconfiguration algorithm. The voltage sensors were added to enable the measurement of block-level I-V curves, which were then processed to emulate the different operating conditions discussed later in Section 5.7.

The procedure implemented to measure the reconfigurable module is illustrated in Figure 5.16. Reconfiguration was performed on a minutely basis. Before each reconfiguration event, all the blocks in the reconfigurable PV module were connected in parallel to measure the I-V curves of each block using the current and voltage sensors integrated in the switching matrix. After this, the reconfiguration algorithm was executed by the microcontroller in the switching matrix, which then acted upon the MOSFETs to set the optimal module configuration. Next, the I-V curve of the reconfigurable module was measured with the BK8616 electronic load, and finally the module was kept at its maximum power point for 1 (until the next reconfiguration event) minute using a perturb and observe (P&O) maximum power tracking algorithm implemented through the

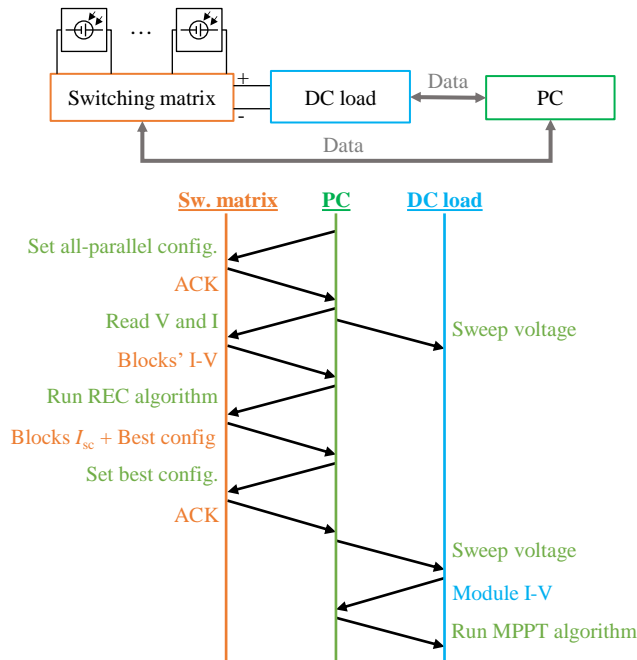


Figure 5.16: Measurement procedure for the reconfigurable PV module. The procedure was executed every 1 minute. The voltage sweeps to obtain the I-V curves are performed by the electronic DC load which is operated in constant voltage mode.

BK8616 electronic load. It is worth noting that under normal operation, it would not be necessary to measure the I-V curves of each block of cells because the reconfiguration algorithm only uses the short-circuit currents of the blocks to find the best module configuration.

The four shading experiments illustrated in Figure 5.17 were conducting throughout the four-month-long monitoring campaign. During experiment 0, the modules were unshaded. Besides, during experiments 1 to 3, the PV modules were shaded by objects fixed on the mounting rack and placed symmetrically on the sides of each module. The goal of these experiments was to evaluate the performance of the module when shading different numbers of groups of cells at the same time.

5.6.1. RECONFIGURABLE PV MODULE PERFORMANCE

The power generated by the reconfigurable and the reference PV modules was compared using the maximum power point (MPP) calculated from the I-V curves measured with the BK8616 electronic load and the LPVO MP1010F-1 MPPT tracking unit, respectively. As an example, the power delivered during a clear sky day by both PV modules during experiment 1 is presented in Figure 5.18a. The power time series show that, when the PV modules were partially shaded (i.e., in the morning and the afternoon) the reconfigurable PV outperformed the reference module. During these intervals, the voltage

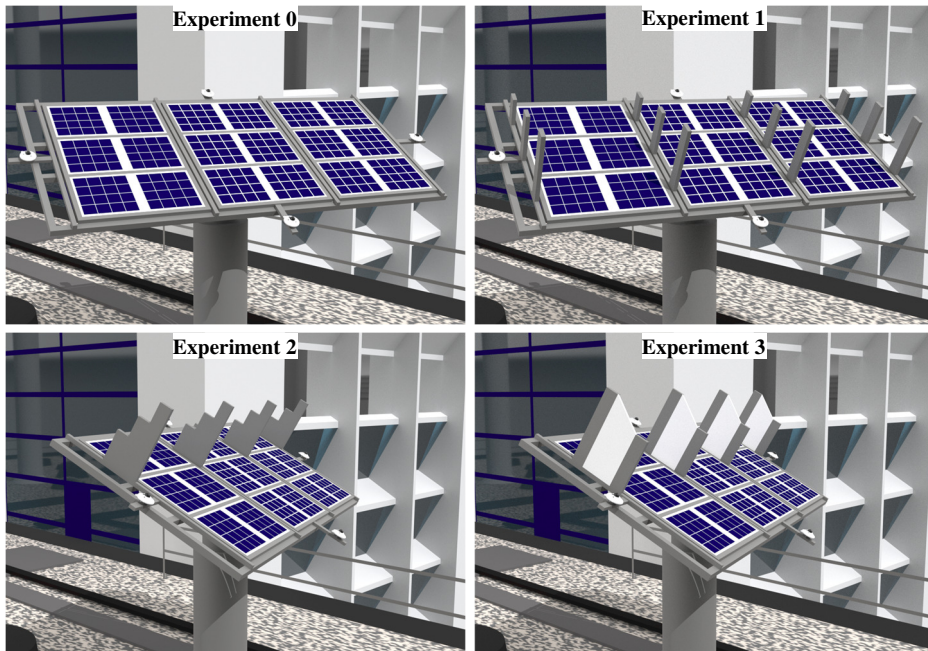


Figure 5.17: 3D models of the shading experiments. In all four experiments the PV modules were tilted 30° . During experiments 0 and 1 the modules were facing south. During experiments 2 and 3 the modules were facing southeast.

time series in Figure 5.18b reveals the progressive activation of the bypass diodes in the reference module and also how the reconfigurable PV module switched between configurations throughout the day to minimise current mismatch losses.

Figure 5.18a also shows that at noon, when the sun was in the south and the modules were unshaded, the reference PV module generated more power than the reconfigurable PV module. From Figure 5.18b it is evident that both modules had the same electrical configuration at noon since the reconfigurable module was operated in the all-series (s6p1) mode. The voltage and power loss in the reconfigurable module under uniform illumination is a direct consequence of the resistive losses in the MOSFETs and the PCB traces in the switching matrix, which amount to an equivalent increase of 7.9% in the series resistance of the solar cells.

The DC energy delivered by the PV modules during each of the experiments is summarised in Table 5.5. On the one hand, the reconfigurable PV module generated about 2% less energy than the reference module in the absence of shading due to the additional resistive losses in the switching matrix. On the other hand, under partial shading (i.e., during experiments 1, 2 and 3), the reconfigurable PV module generated between 4.8% and 13.7% more energy than the reference module. The yield difference was larger for the experiments when the PV modules were more often subject to partial shading (indicated in the "Shading" column in Table 5.5). Moreover, the yield difference between the reconfigurable and reference PV modules was also determined by the number of

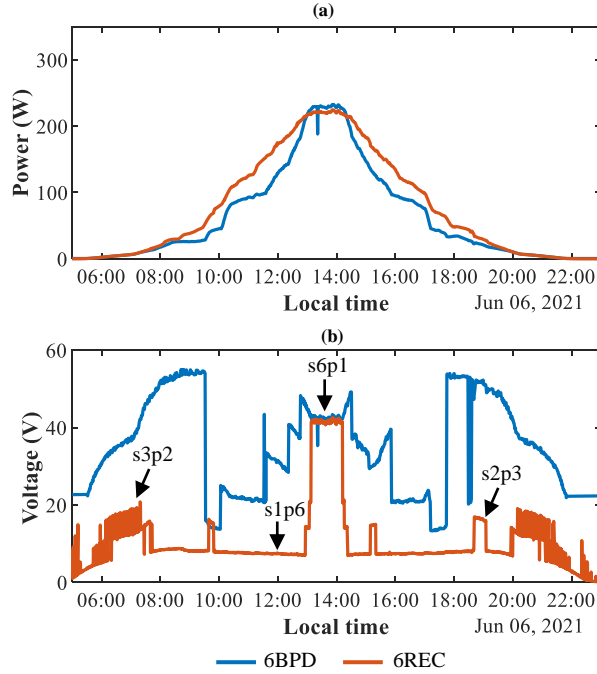


Figure 5.18: Comparison of the electrical output of the reference (6BPD) and reconfigurable (6REC) PV modules in a clear sky day during experiment 1. (a) Maximum power time series. (b) MPP voltage time series. The voltage levels on the red curve can be directly associated to different types of configurations.

	Length (days)	Shading (%)	DC yield 6BPD (kWh)	DC yield 6REC (kWh)	DC yield diff. (%)
Experiment 0	13	0	16.8	16.5	-1.9%
Experiment 1	35	34	32.5	37.0	13.7%
Experiment 2	27	24	22.8	23.9	4.8%
Experiment 3	24	30	18.0	19.9	10.3%

Table 5.5: DC energy yield of each experiment. The DC yield difference was calculated as the relative deviation of the DC yield of the 6REC module from the DC yield of the 6BPD module.

blocks that were shaded at the same time. From the positions of the shading objects in Figure 5.17, it can be seen that in experiment 2, most of the time only one of the top blocks of cells was shaded. This shading pattern was effectively mitigated by the 6BPD module, where the shaded block was bypassed and only one sixth of the total module power was lost. Consequently, the DC yield difference between the 6BPD and 6REC modules in experiment 2 was significantly lower than in experiments 1 and 3, when more than one block of cells were often shaded at the same time.

In addition, the pie charts in Figure 5.19 show the percentage of the energy delivered by the different configurations of the 6REC module during each of the shading exper-

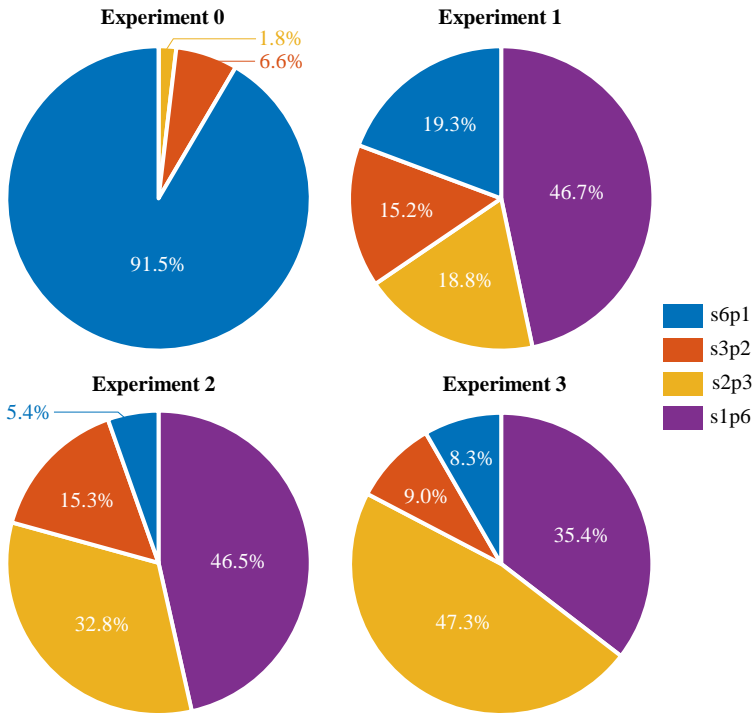


Figure 5.19: Energy yield share by configuration. While the s6p1 and the s1p6 represent only one configuration each, the pie sections corresponding to the s3p2 and s2p3 represent multiple possible configurations with similar electrical characteristics.

iments. As expected, during experiment 0, the reconfigurable PV module was mostly operated in the s6p1 (all-series) configuration because the module was uniformly illuminated. During experiments 1 to 3, the algorithm frequently chose configurations with parallel interconnections to reduce current mismatch caused by the partial shading. In particular, it is evident that the s1p6 (all-parallel) configuration contributed with a significant share to the total generated electricity in all three experiments when the module was partially shaded. As discussed before, the s1p6 configuration implies low output voltages and high output currents that entail a burden on the design and performance of the power converter for the reconfigurable PV module.

5.7. LIMITING THE ELECTRICAL OPERATING RANGE

The results from the outdoor monitoring campaign show that in the absence of shading, the 6REC module was mostly operated in the s6p1 configuration and delivered approximately the same current as the 6BPD module. Instead, when there was partial shading, the reconfigurable PV module tended to deliver higher currents because the algorithm chose configurations with different combinations of blocks connected in parallel.

The electrical operating ranges of the 6BPD and 6REC modules are compared in Fig-

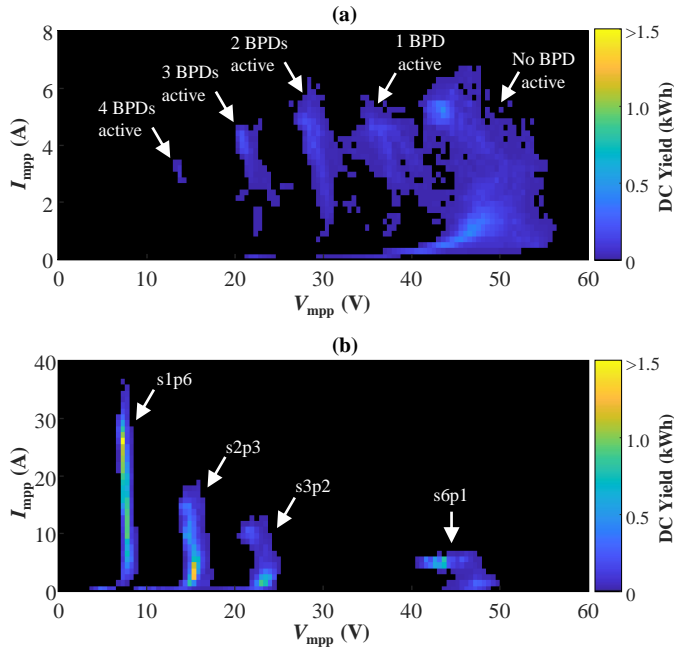


Figure 5.20: Operating point of the PV modules during the shading experiments 1, 2 and 3. (a) Current and voltage delivered by the PV module with 6 bypass diodes (6BPD). (b) Current and voltage delivered by the reconfigurable PV module (6REC). The colour bar indicates how much energy was delivered at the different operating points.

ure 5.20, where it is illustrated how much energy was delivered at each voltage and current level during the experiments when the PV modules were partially shaded. In Figure 5.20b, it can be noticed that the 6REC module generated up to 40.8 A, about 6 times more than the maximum current of 7.2 A of the 6BPD module in Figure 5.20a. In addition, the output voltage of the 6BPD module ranged from 13.3 V to 57.9 V, while the output voltage of the 6REC module range from 5.6 V to 52.3 V.

It is pertinent to observe that the high current differences between the 6REC and 6BPD modules measured during the experiments were unexpected based on the simulation results presented in Figure 5.8a. Nonetheless, there are several factors that could explain these differences. First, it must be noted that the simulated rooftop in Figure 5.5 was tilted 57° . Instead, the tilt during the experiments was 30° , which resulted in higher PoA irradiances. Second, the shadows cast by the chimneys in the simulated rooftop were larger compared to the shadows in the experiments, which resulted in more frequent shading patterns where two or more blocks of cells were shaded at the same time. And third, measurement noise in the short-circuit currents used as input to the reconfiguration algorithm might have promoted the choice of the all-parallel configuration more often than necessary.

As a result of the extended operating range, a power converter for a reconfigurable PV module would be larger, less efficient and/or more expensive than a power converter

for conventional PV module. Although the design of a suitable power converter for a reconfigurable PV module is beyond the scope of this work, one way to reduce the burden on the design of the power converter is by adapting the operation of the reconfiguration algorithm. In particular, one straightforward approach to ease the design of the power converter consists in limiting the electrical output range of the reconfigurable module. This can be achieved by setting the threshold T_3 to infinite (refer to Figure 5.4) to avoid configuration s1p6, which delivers the highest currents and lowest voltages. If configuration s1p6 is removed, the reconfiguration algorithm chooses the best s2p3 configuration, and it is evident that the reconfigurable module becomes less shading tolerant. The energy loss resulting from the modification of the reconfiguration algorithm was evaluated using the measured I-V curves.

Even though the best s2p3 configuration was not measured, it can be calculated using the I-V curves of the blocks measured with the current and voltage sensors integrated in the switching matrix. The I-V curve of the different module configurations were recreated by interpolating and adding the measured voltages (in the case of series connections) or currents (in the case of parallel connections) of each of the six blocks of cells in the reconfigurable module.

Figure 5.21 depicts the operating range of the reconfigurable PV module for the presented shading scenarios after modifying the algorithm to avoid configuration s1p6. While the 6REC module with the original algorithm generated in average 10.2 % more energy than the 6BPD module (only considering shading experiments 1 to 3), the energy yield of the 6REC module with the modified algorithm would be 6.4 % higher than the 6BPD module. In return, the maximum output current the reconfigurable PV module would be reduced to 20.2 A and the output voltage would range from 10.7 V to 52.3 V.

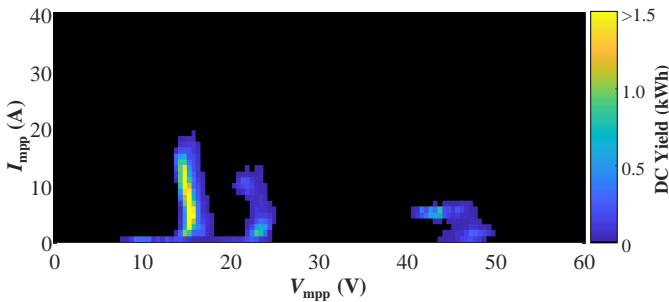


Figure 5.21: Operating point of the 6REC PV module during the shading experiments 1 to 3 after modifying the reconfiguration algorithm to avoid the s1p6 (all-parallel) configuration. The colour bar indicates how much energy was delivered at the different operating points.

It is clear that there is a significant average yield loss (3.8 %) due to the lower shading tolerance of the 6REC module when the s1p6 configuration is precluded. At the same time, by reducing the output of the PV module to approximately 20 A, Joule losses in cables and conversion losses in the power electronics would also be significantly reduced. In order to verify whether it is beneficial to avoid configuration s1p6, the complexity of the design and efficiency of power converters for both versions of the reconfigurable

module should be carefully investigated and further system-level analyses should be performed.

5.8. A WORD ON RELIABILITY

Reliability is one of the most critical aspects of the design of a PV module. Any prospective solution to improve the performance of PV systems should not compromise the performance at 25- to 30-year end-of-life offered by commercially available PV modules. While the analysis of the reliability of the reconfiguration matrix is out of the scope of this work and requires in depth consideration, some basic observations are needed.

The reliability of commercially available PV modules is strongly influenced, among other factors, by bypass diodes. Their failure can have far-reaching consequences, significantly affecting both performance and safety. There are two primary modes in which bypass diodes can fail, each with its own implications [205].

Firstly, the short-circuit mode of failure is relatively common and directly impacts the performance of PV modules. In modules equipped with three bypass diodes, the failure of just one diode due to a short-circuit condition causes an output power loss of approximately one-third. This kind of failure can be attributed to various factors, including incorrect specification or selection of bypass diodes and high voltage events.

Conversely, the open-circuit mode of failure, under normal circumstances does not affect directly the PV module's power but introduces safety concerns. When a bypass diode fails in an open-circuit condition, it can pose a risk when shading occurs. When solar cells are not protected by a bypass diodes, they can be subjected to high reverse bias, potentially leading to cell breakdown, overheating, and, in the most severe cases, a fire hazard.

There are multiple mechanisms that contribute to bypass diode degradation and failure, encompassing phenomena such as arcing, electrostatic discharge, thermal runaway, high-temperature forward bias operation, high-temperature reverse bias operation, and thermal cycling [206]. These mechanisms illustrate the intricate interactions between environmental and operational factors that can impact the reliability of bypass diodes.

Effective thermal management and proper diode selection are crucial to ensure reliability across a range of environmental conditions. For example, the junction box, which typically houses the bypass diodes, experiences temperature increases corresponding to rising ambient temperatures. On sunny summer days, both the module surface and the junction box can reach temperatures over 70 °C. Under these conditions, the leakage current of the diodes can increase up to 35 times, which leads to a proportional increase in the power dissipated in the diodes when the PV module is under uniform illumination [207].

The proposed switching matrix introduces several new reliability challenges. To begin, its implementation requires many more semiconductor devices compared to the typical three bypass diodes found in commercially available photovoltaic modules and to PV modules with sub-module power converters. Moreover, from a reliability perspective, many of the components in this switching matrix are considered series elements. For instance, the correct operation of the switching matrix relies on the simultaneous proper operation of the MOSFETs, their associated driver circuit and all the current sensors. Furthermore, certain MOSFETs will endure more frequent usage than others, re-

sulting in an acceleration of wear and a decrease in the reliability of these specific components.

As a consequence, a higher failure rate of the switching matrix is expected in comparison to conventional PV modules featuring bypass diodes and fixed interconnections. Nevertheless, it must be noted that the switching matrix exhibits a certain degree of resilience against specific failure modes. For instance, MOSFETs are prone to failing in short-circuit conditions due to gate oxide degradation. In the event that one MOSFET fails and transitions into a short-circuit state, the reconfiguration matrix can continue to operate safely, albeit with a reduced number of feasible configurations and higher conduction losses.

In addition, in the proposed reconfigurable module, where bypass diodes could be omitted, the reliability of the system becomes heavily contingent on the accuracy of the current sensors and the reconfiguration algorithm's ability to quickly detect shading conditions to prevent an excessive reverse bias and power dissipation in the shaded solar cells.

Certainly, undertaking a thorough evaluation of the reliability of the proposed reconfigurable modules will be crucial in future work to guarantee that its lifetime is consistent with those of modern commercially available PV modules.

5.9. CONCLUSIONS

In this chapter, reconfigurable PV generators were investigated as a means of maximizing the yield of partially shaded PV systems. In particular, an instance of a series-parallel reconfigurable PV module was proposed and analysed. The reconfigurable module consists with 96 solar cells arranged in 6 reconfigurable blocks and a reconfiguration algorithm to control its switching matrix. The rest of the chapter was dedicated to evaluating the performance of this design.

First, 3 shading tolerant PV module topologies were simulated and compared under different shading scenarios to calculate the potential energy yield that could be obtained with the proposed reconfigurable module. Simulation results indicate that when a PV module is partially shaded about 30% of the time, the reconfigurable PV module topology can deliver up to 12.7% more energy than a shade tolerant PV module topology with 6 bypass diodes. Moreover, it was calculated that a module with 6 strings of cells connected in parallel would perform marginally better than the reconfigurable module in terms of annual DC yield but it would deliver much higher electrical currents, which implies a lower DC-DC conversion efficiency. Simulations also allowed us to determine that the proposed reconfiguration algorithm based only on short-circuit current measurements can in theory achieve an energy efficiency over 99.9%.

Later, a prototype of the proposed PV module and the reconfiguration matrix was built and tested. First, the measured electrical performance of all module configurations was evaluated indoors with a flash tester and three shading cases and resulted in an excellent match with the simulation results. Subsequently, an outdoor measurement campaign was conducted to assess the performance of the reconfigurable series-parallel PV module. As a reference for comparison, a PV module with six bypass diodes and static interconnections was monitored simultaneously with the reconfigurable module. Measurements indicate that in the absence of shading the reconfigurable PV module

performed 1.9% worse than the reference module due to the additional resistive losses introduced by the switching matrix. Instead, when the PV modules were subject to partial shading, the reconfigurable PV module delivered in average 10.2% more energy. In particular, the difference between the energy yield of both modules was larger for shading scenarios where two or more blocks of cells were often shaded at the same time.

During the outdoor shading experiments about 40% of the energy was delivered by the configuration in which all six blocks of cells are connected in parallel. Although the all-parallel is the most shading tolerant among the 27 possible configurations, it is also the one that generates the highest currents and thus may lead to the highest losses at system level. To avoid high currents, the performance of a hypothetical reconfigurable PV module where the all-parallel configuration is precluded was evaluated. This measure effectively limits the maximum current and the minimum voltage generated by the reconfigurable PV module, which implies a simpler design of the power converter and reduced the Joule losses in cables. However, it was found avoiding the all-parallel configuration would reduce the yield of reconfigurable module in 3.8%. It was concluded that further research on the efficiency and complexity of power converters is needed to determine whether it is beneficial to include the all-parallel configuration.

In the future, asynchronous algorithms together with other sensed parameters at the level of PV module can be exploited to improve the performance of reconfigurable modules. Most interestingly, an approach based on machine learning could be implemented for facilitating an AI engine which optimally controls the reconfiguration. Finally, the presence of a microcontroller in the envisioned smart junction box can also be used to tokenise and trade energy packets in the future digital energy market.

6

PV MODULES WITH LOW BREAKDOWN VOLTAGE SOLAR CELLS

This chapter is based on the following publication:

A. Calcabrini, P. P. Moya, B. Huang, V. Kambhampati, M. Muttillio, M. Zeman, P. Manganiello, O. Isabella, *Low breakdown voltage solar cells for shading tolerant photovoltaic modules*, Cell Reports Physical Science **3**, 12 (2022).

6.1. INTRODUCTION

One critical factor that determines the shading tolerance of a PV module is the reverse current-voltage (I-V) characteristics of its solar cells. Most crystalline Si (c-Si) solar cells technologies present a breakdown voltage¹ (BDV) between 10 V and 30 V [208], [209]. Owing to the large BDV, shaded solar cells restrict the current flow and the power output of the entire string of cells. Moreover, when a shaded cell is driven into reverse bias operation, it dissipates large amounts of power, which can lead to the formation of hot-spots [210] and permanent damage in the PV module. The most common approaches to mitigate these negative effects and improve the shading tolerance of PV modules consist in adding bypass diodes and connecting strings of solar cells in parallel [211].

Bypass diodes have been used for decades in the PV industry [143], [145] to limit the output power loss, as well as the power dissipated in reverse biased solar cells. Most c-Si PV modules in the market include 3 bypass diodes that help to reduce (yet do not eliminate) the occurrence of hot-spots [212]. Eventually, the addition of one bypass diode per cell [165] can virtually reduce the BDV of the solar cells below 0.5 V.

¹Breakdown voltages are usually expressed with negative values since the breakdown region is in the second quadrant of current-voltage plane. However, for the sake of clarity, in this chapter the breakdown voltage is always refer to by its absolute value.

Parallel interconnections, on the other hand, improve the shading tolerance of PV modules [213] by avoiding the current mismatch issue. However, connecting solar cells in parallel can lead to high electrical currents and Joule losses at system level. As a countermeasure, PV modules with parallel interconnections are usually made with cut cells to reduce the total module current [167], [214]. The most prominent example of commercial PV modules with parallel interconnections are half-cut solar cell modules [168], [169], [173].

These approaches that were explored in the preceding chapters are effective ways to improve the shading tolerance of PV modules [215], yet they imply a more complex module manufacturing process. Aiming to simplify the module manufacture and reduce costs, it was proposed to integrate bypass diodes directly in the structure of the solar cell. While the implementation of integrated bypass diodes in front-back contact (FBC) [171], [216]–[218] and metal wrap through (MWT) [219] solar cells requires additional fabrication steps and may reduce the active area of the device or introduce new thermal management challenges, developments in interdigitated back contact (IBC) solar cells offer new possibilities for the integration of bypass diodes [220]. In this case, the junctions that naturally form between the back surface field (BSF) and the emitter regions on the rear side of an IBC solar cell can be used to bypass the solar cell when it is reverse biased.

A few research groups and companies have already manufactured IBC solar cells with BDVs as low as 3 V [221]–[224]. However, until now research on IBC structures has been primarily focused on increasing the cell conversion efficiency to maximise the energy yield of PV modules. This chapter explains that improving the reverse characteristics of IBC solar cells can be a promising approach to boost the performance of PV modules by increasing their shading tolerance and limiting the operating temperature of shaded solar cells. First, the breakdown characteristics of realistic IBC solar cells endowed with carrier-selective passivating contacts and presenting contiguous p+ and n+ regions is studied through detailed device-level simulations. Then, system-level performance simulations are presented to quantify the effect of the breakdown voltage of a solar cell on the annual energy yield and the operating temperature of partially shaded PV modules. Finally, the findings of a four-month-long monitoring campaign are summarised, which compared the energy yield of two PV modules made with solar cells having different breakdown characteristics.

6.2. LOW BREAKDOWN VOLTAGE IBC SOLAR CELLS

Even though the fabrication process of IBC solar cells is generally more complex than that of most FBC technologies, IBC devices allow for higher conversion efficiencies by eliminating the optical losses caused by the front metallic grid [225]–[227]. For this reason, IBC technology is expected to become one of the next technological improvements (together with passivating contacts) to be implemented in commercial c-Si cells to continue improving their efficiency.

This chapter focuses on the effects of the breakdown voltage on the annual energy yield of PV modules considering the IBC structure with poly-Si/SiO_x contacts shown in Figure 6.1a. This is the so-called tunnelling oxide passivating contact (TOPCon) technology. Typically, in IBC solar cells based on TOPCon technology [228], [229], the emit-

ter and the back surface field (BSF) regions are physically isolated to prevent shunting due to the diffusion of dopant atoms into the c-Si base during the thermal processing steps [230]. However, it was experimentally demonstrated that it is possible to design highly efficient TOPCon IBC cells with contiguous BSF and emitter regions, where the p+ and n+ fingers are separated by a compensated poly-Si region [231], thus forming a p-i-n junction.

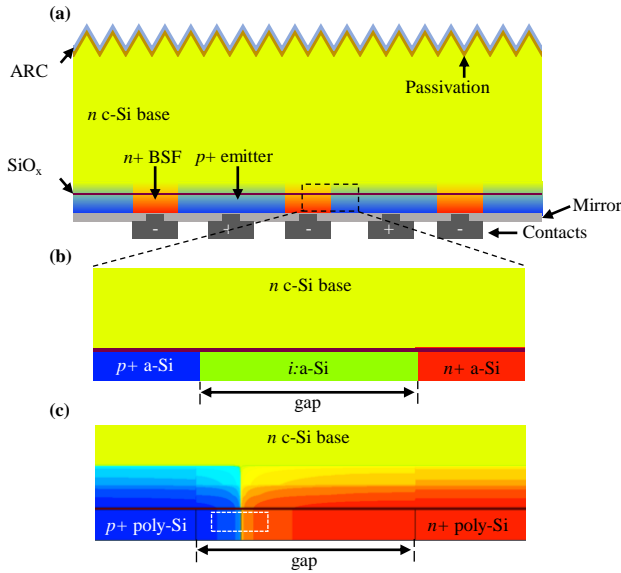


Figure 6.1: Solar cell structure. (a) Analyzed TOPCon IBC solar cell structure. (b) Close-up view of the region between the back surface field (BSF) and the emitter before crystallisation. (c) Distribution of dopants after crystallisation as simulated in TCAD Sentaurus. The vertical dimension of the figure is stretched to also visualise the penetration of dopant atoms in the c-Si base. The dashed rectangle highlights the portion of the gap investigated in Figure 6.2.

Despite the diffusion and mixing of dopant atoms in the emitter and BSF regions during cell processing steps, the recombination of charge carriers in the above-mentioned p-i-n junction is strongly limited when the solar cell is forward biased [232]. Instead, when the cell is reverse biased, the p-i-n junctions facilitate the recombination of the electrons injected at the negative terminal with holes in the emitter. In addition to the avalanche breakdown mechanism, the high doping level in the polysilicon gap region also enables the tunnelling of carriers at low bias voltages. Herein, the influence of this p-i-n junction on the forward and reverse I-V characteristics of a solar cell and the energy yield of PV modules is analysed through detailed simulations.

6.3. BREAKDOWN VOLTAGE SIMULATIONS

Under low-level injection and forward bias conditions, 1-D models can accurately simulate the performance of IBC solar cells [233]. However, for the IBC structure in Figure 6.1a, a 2-D model was required to simulate the horizontal movement of carriers be-

tween the BSF and the emitter [232]. The electrical simulations of solar cells in this work were performed using a 2-D finite element model in TCAD Sentaurus which simultaneously solves Poisson's equation and the charge carrier transport equations. This model has been validated with respect to homojunction, heterojunction and TOPCon IBC c-Si solar cells [234]–[237].

In order to achieve cells with different breakdown voltages, simulations were performed considering different widths for the originally intrinsic gap region between the emitter and the BSF illustrated in Figure 6.1b. It was considered that during the thermal processing steps in the fabrication of an IBC solar cell, the dopant atoms in the BSF and the emitter diffuse towards the i:poly-Si region and the c-Si base. While the SiO_x layer hinders the diffusion of dopant atoms into the c-Si base, dopant atoms can diffuse in the lateral direction rather easily as depicted in Figures 6.1c and 6.2a.

The gap width was varied in the simulated cell structures from $15\ \mu\text{m}$ down to $6\ \mu\text{m}$ maintaining the shape of the doping profiles, i.e., the standard deviation of the Gaussian functions that define the doping concentration was kept constant.

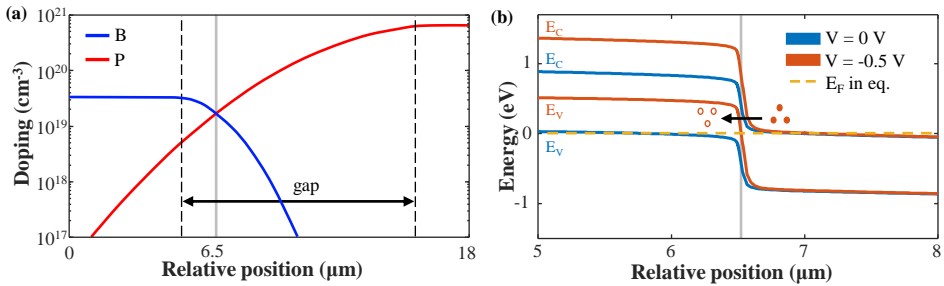


Figure 6.2: (a) Doping profile inside the poly-Si region marked with dashed lines in Figure 6.1. The vertical dashed lines indicate the gap between the p+ and n+ fingers before crystallisation. The vertical grey solid line indicates the position at which the doping profiles meet and polysilicon is compensated. (b) Band diagrams along the polysilicon region of the IBC cell in dark at short-circuit and reverse bias conditions considering the doping profiles shown in sub-figure a. The dashed line represents the Fermi level in short-circuit conditions. In reverse bias, the electrons (filled dots) injected through the negative terminal of the cell recombine through tunnelling with holes (empty dots) in the p+ side.

Solar cell simulations were adapted from previous works on numerical simulation of IBC devices [236] to include the transport of carriers between the BSF and the emitter. In particular, the band-to-band tunnelling effect in this region was simulated using self-consistent tunnelling models.

As previously mentioned, there are two main transport mechanisms that contribute to the breakdown voltage: avalanche and tunnelling. Between these two transport mechanisms, tunnelling is generally dominant when the breakdown voltage is lower than about four times the band gap (approximately 4.5 V in Si) [238]. In addition, the temperature coefficient of the breakdown voltage of all the simulated cells was positive, which also indicates that band-to-band tunnelling dominates over avalanche [223].

The simulated band diagrams in dark along the poly-Si region in Figure 6.2b show that as the solar cell is driven into the reverse bias operating region, the tunnelling barrier reduces allowing electrons injected by the external circuit into the n+ region to re-

combine with holes in the p+ region.

In this study, the width of the gap between the BSF and the emitter was reduced to shorten the tunnelling distance and obtain cells with lower breakdown voltages. However, it must be noted that the breakdown voltage is controlled by the doping profile in the space domain, which is also influenced by cell fabrication steps that define the shape of the doping tails in Figure 6.2a. Therefore, alternative approaches to fabricate a polysilicon region with similar characteristics to those discussed in this chapter could also result in cells with low breakdown voltages.

The simulation results of solar cells with different gaps are summarised in Figure 6.3. Two important trends were identified as the gap between the BSF and the emitter was reduced. A smaller gap implied a shorter tunnelling distance in reverse bias, which in turn led to a lower (absolute) breakdown voltage as shown in Figure 6.3a. At the same time, reducing the (originally) i:poly-Si gap resulted in a higher overlap between heavily doped regions at the bottom of the c-Si base due to vertical diffusion of dopant atoms through the SiO_x layer. This overlap led to a higher recombination, hence a reduction in the open-circuit voltage (Figure 6.3b) and the efficiency (Figure 6.3c) of the solar cell.

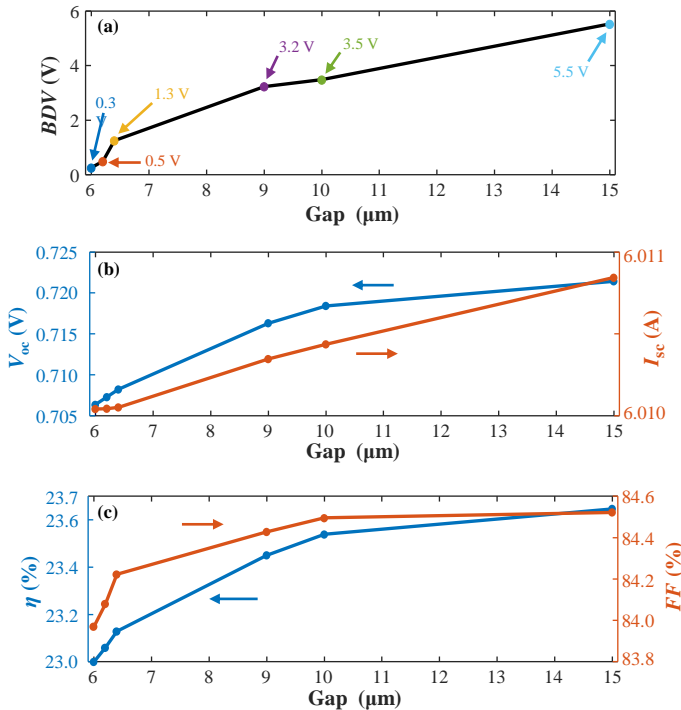


Figure 6.3: External parameters of the simulated solar cells. (a) Breakdown voltage of the IBC solar cells in dark at 2 A. (b) Open-circuit voltage and short-circuit current of IBC cells with different gap widths at standard test conditions. (c) Efficiency and fill factor of IBC cells with different gap widths at standard test conditions.

As the breakdown voltage is reduced, the power dissipated in reverse biased cells is also decreased. On top of that, the dissipated power in IBC cells can be more uniformly

distributed over the area of the solar cell due to the interdigitated structure of the BSF and emitter regions. The combination of these two factors helps to lower the probability of occurrence of hot-spots (in comparison to front-back contact solar cells) and can allow low BDV IBC cells to be safely self-bypassed.

The inclusion of bypass diodes in PV modules with low BDV solar cells can provide additional protection against hot-spots if the number of series-connected cells under one bypass diode (N_s) satisfies²:

$$N_s \leq 1 + \frac{|V_R| - V_{BPD}}{V_F} \quad (6.1)$$

where V_F and V_R are respectively the voltage of one cell in forward and reverse bias at a given current level, and V_{BPD} is the forward voltage of the bypass diode [239]. Nevertheless, bypass diodes can still help to improve the shading tolerance of the PV module even if Equation (6.1) is not satisfied, when more than one cell in a sub-string is shaded.

6.4. ANNUAL ENERGY YIELD SIMULATIONS

In the PV industry, the prevailing metric for evaluating the cost-effectiveness of solar modules has long been price per watt (PPW). While convenient, this metric has limitations that hinder a comprehensive assessment of solar cell technologies. For instance, PPW fails to account for essential factors like shading resilience and thermal coefficients, which are determinant for the module's energy yield performance. While the Levelised Cost of Electricity (LCOE) offers a more holistic approach to cost assessment, estimating the actual electrical energy generated by a PV system remains a challenging task.

The trends in efficiency and breakdown voltage in Figure 6.3 have opposing effects on the energy yield of solar modules. Higher efficiencies lead to a higher power in forward bias, whereas lower BDVs minimise losses in reverse bias. Each pair of efficiency-BDV values results in a certain energy yield that depends on the actual installation and operating conditions of the PV modules. To quantify this, the performance of PV modules in real-world operating conditions was simulated using an advanced optical-thermal-electric simulation framework, which enables the accurate computation of the temperature and the electric power generated (or dissipated) by each solar cell in a PV module.

6.4.1. SIMULATION FRAMEWORK

Numerical simulations were performed using a state-of-the-art framework described by the flowchart in Figure 6.4.

The irradiance incident on the surface of the PV modules was calculated using *Radiance* and detailed CAD models of the PV installations following the approach described in Chapter 3. In order to improve the accuracy of the results, the spectral distribution of the beam, diffuse and reflected irradiance components were approximated using SB-DART [127] and sky classifier introduced in Section 3.4.3.

The absorbed irradiance and generation rate of charge carriers inside the solar cell (i.e., the optical generation profiles) were calculated using GenPro4 [104]. The effect

²This condition is derived from the worst case scenario for hot-spots, i.e., when single cell in a sub-string is shaded.

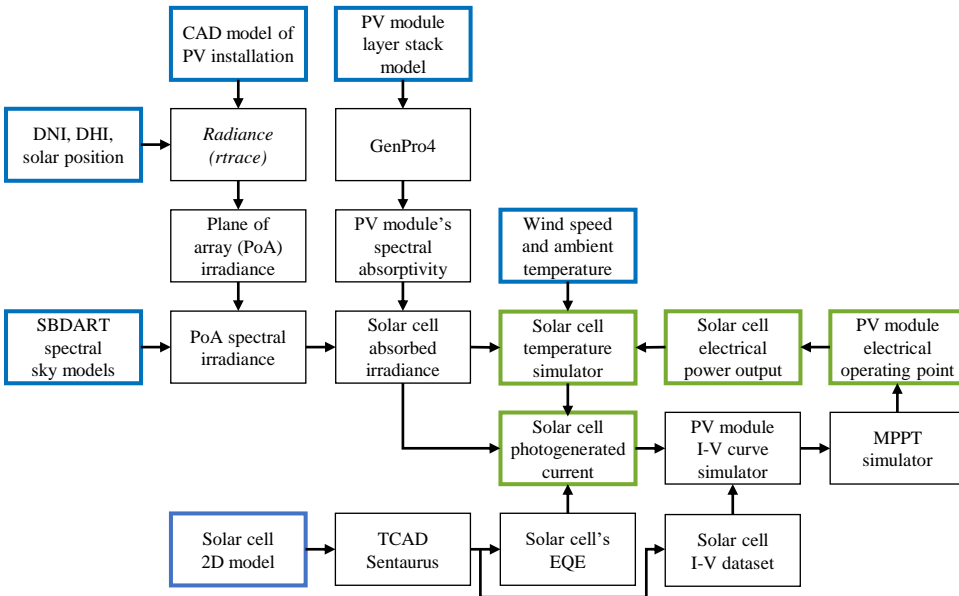


Figure 6.4: Energy yield simulation framework. The inputs and outputs of the framework are highlighted in blue and green, respectively.

of temperature on the refractive index of the c-Si bulk was modelled according to [240] and parasitic light absorption in the c-Si base (e.g., due to free carrier absorption) was neglected. The resulting optical generation profiles at different irradiance and temperature conditions were then imported into TCAD Sentaurus to simulate the I-V curves of the solar cell in forward and reverse bias.

The diffusion of dopant atoms in the gap region was modelled in TCAD Sentaurus according to the profile in Figure 6.2a, which was fitted from measurements on high efficiency IBC devices [231]. Next, the I-V curves of the solar cells were simulated under a wide range of temperature and illumination conditions with 5°C and 100 W m^{-2} resolution. Then, I-V curves simulated with TCAD Sentaurus were interpolated to increase the resolution of the cell's I-V dataset to 1°C and 2 W m^{-2} by applying cubic Hermite splines.

Afterwards, the I-V curves of the PV module were computed by adding together the voltage (in series connections) or the current (in parallel connections) of the I-V curves of the solar cells in the I-V dataset generated with TCAD Sentaurus (or measured in the case of the experimental setup) and the I-V curves of the bypass diodes. Joule losses in tabbing and bus wires were modelled as an increase in the series resistance of the solar cells. Joule losses in wires and connectors were applied to the final PV module I-V curve.

After calculating the I-V curves of the PV modules, the operating point was determined assuming that each module was connected to a dedicated power converter with an operating voltage range of [25 V - 70 V] and a maximum power point tracking algorithm that performs I-V sweeps every 5 minutes to find the global maximum in the P-V curve.

Finally, the cell temperature was modelled using the 2-D finite element method thermal model described and validated in [241]. It is relevant to mention, that contrary to the simulation frameworks described in the preceding chapters, the thermal model in Figure 6.4 was coupled with the electrical model to account for the electrical power extracted from (or dissipated in) the solar cells.

6.4.2. SIMULATION RESULTS

The performance of PV modules made of solar cells with different gap widths was simulated considering a PV system on a typical Dutch rooftop depicted in Figure 6.5a. The simulation was performed throughout an entire year using Meteonorm climate data with 1-minute resolution for De Bilt, The Netherlands [176].

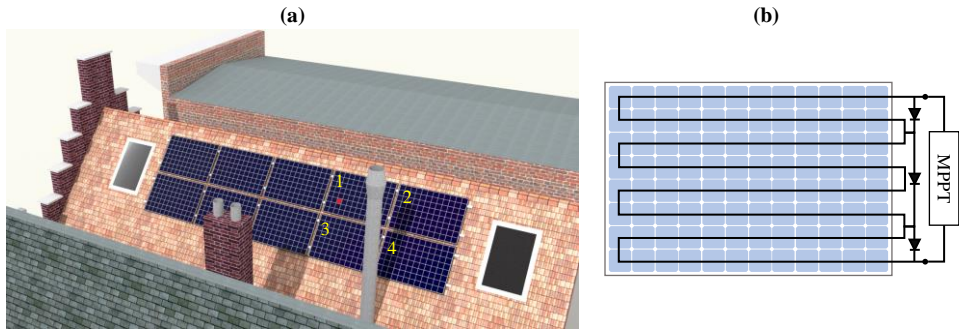


Figure 6.5: Simulated PV system. (a) CAD model of the simulated PV system on the rooftop of a typical Dutch house. The rooftop is tilted 50° and facing south. Simulation results correspond to the PV module positions number from 1 to 4. (b) Simulated PV module topology. It is assumed that each PV module is connected to a dedicated power converter with maximum power point tracking (MPPT) capability.

Despite the chimneys in front of the PV modules, Table 6.1 shows that all four modules still receive relatively high levels of irradiation.

The simulated PV modules topology, illustrated in Figure 6.5b, consists of 96 5-inch IBC solar cells and 3 Schottky bypass diodes interconnected as in typical commercial PV modules.

The simulated power generated by the PV module on rooftop position 1 during a clear sky day is shown in Figure 6.6a. It is possible to see that, when the module was unshaded, the cells with larger gaps delivered slightly more power owing to the higher cell efficiency. However, between 10 a.m. and 1 p.m., when the module was partially shaded by one of the chimneys, the advantage of cells with smaller gaps and thus low breakdown voltages become self-evident. Moreover, the power-voltage (P-V) curves at 11 a.m. portrayed in Figure 6.6b show that cells with smaller gaps result in higher maximum power point voltages under non-uniform illumination but, at the same time, tend to create multiple local peaks in the P-V curve. Despite the multiple peaks, results indicate that an MPPT algorithm with 5-minute I-V scans would be effective at maximising the PV module power in all the simulated cases.

The annual energy yields of the simulated modules are presented in Figure 6.7. The relative energy yield gain was calculated taking as reference a PV module with solar cells

	Average annual irradiation (kWh/m ²)	Relative annual irradiation (%)	Shading (%)
Free horizon	1145	100	0
Position 1	1056	92.2	10.1
Position 2	1056	92.2	10.4
Position 3	893	78.0	18.0
Position 4	905	79.0	19.1

Table 6.1: Solar irradiation on the analysed rooftop positions. The irradiation for the "free horizon" case is calculated assuming that there are no obstacles around the PV module using climate data from De Bilt, the Netherlands. The condition set to calculate the time that a module is partially shaded is when the irradiance on the most shaded cell in the PV module is less than 50 % of the irradiance on the most illuminated cell in the PV module.

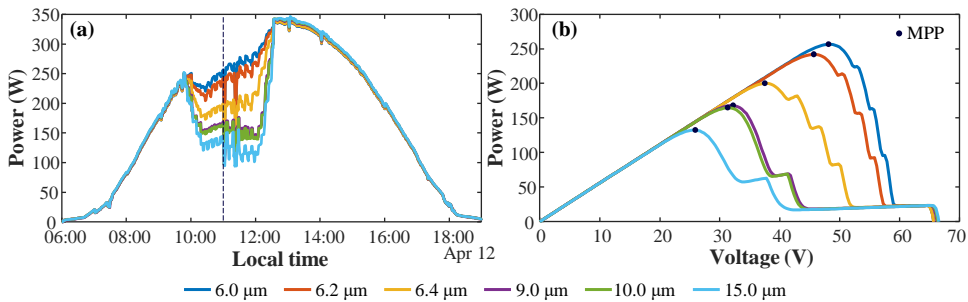


Figure 6.6: Simulated PV system. (a) Simulated maximum power point time series during a clear sky day (April 12th) for the PV module at rooftop position 1 with cells with different gap widths. The vertical dashed line is at 11 a.m. (b) Power-Voltage curves of the PV modules with different gap widths at position 1 on April 12th at 11:00 a.m.

with the same forward characteristics as the cell with a 15 μm gap but an infinite breakdown voltage. In the case of the analysed PV module topology shown in Figure 6.5b, the shading response of a PV module with cells with an infinite breakdown voltage is comparable to any solar cell technology with a breakdown voltage higher than approximately 15 V³, which is the case for most commercial front/back contacted monocrystalline solar cell technologies, including PERC cells [208], [209], [214].

As shown in Figure 6.7, all the modules with low breakdown voltage solar cells delivered higher yields than the reference because shaded cells with low breakdown voltage can be self-bypassed without affecting the power delivered by adjacent unshaded cells. In most cases, the energy yield loss due to a lower cell efficiency was overbalanced by energy yield gain due to a lower breakdown voltage. The energy gain is more evident for gaps smaller than 9 μm ($BDV < 3V$). In particular, the module with cells with a 6 μm gap ($BDV = 0.3V$), generated over 20 % more energy than the reference PV module at rooftop position 4, which is partially shaded about 20 % of the time.

³Considering that in the worst case scenario, when a single solar cell in a sub-string is shaded, the 23 unshaded solar cells can deliver approximately 14 V at the maximum power point, i.e., about 610 mV per cell.

It should be noted that, although industrial solar cells with $BDV = 2.2\text{V}$ have already been achieved [242], the feasibility of manufacturing cost-effective solar cells with breakdown voltages as low as 0.3V is yet to be demonstrated.

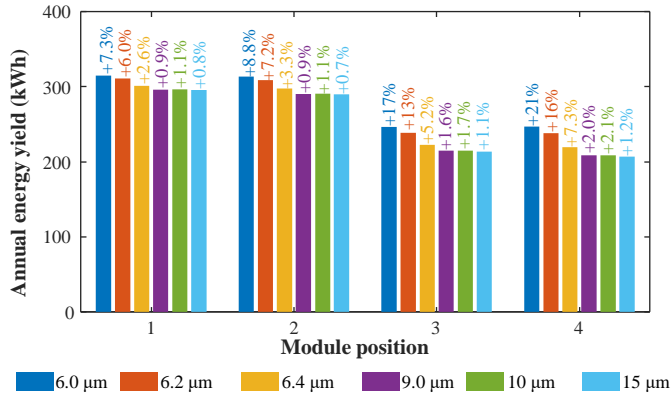


Figure 6.7: Simulated annual energy yield of PV modules on the typical Dutch rooftop of Figure 6.5a. The percentage above the bars indicates the relative energy yield gain with respect to a PV module made with solar cells that have the same forward characteristics as the cell with a $15\mu\text{m}$ gap but with a simulated infinite breakdown, typically $> 10\text{V}$ or greater than the sum of the V_{oc} of the non-shaded cells in the sub-string.

The breakdown voltage also influences the thermal performance of reverse biased solar cells. Figure 6.8a presents the simulated temperature of the cell painted in red in Figure 6.5a during a clear sky day. The plot shows around 11 a.m. when shading occurs, cells with smaller gaps heated up significantly less than cells with larger gaps. One interesting observation is that the temperature of the cells with gaps of $6\mu\text{m}$ and $6.2\mu\text{m}$ dropped instead of increasing because the reduction in the absorbed radiation outweighed the power dissipated under reverse bias in the thermal balance. The average and maximum cell temperature during the whole simulated year are depicted in Figure 6.8b. While the mean annual temperature was approximately constant, it is clear that the maximum cell temperature strongly depends on the reverse breakdown characteristics. These results suggest that solar cells with small gaps can significantly limit the temperature increase due to partial shading which could be beneficial for the PV module's lifetime and reliability, and especially relevant to decelerate the degradation of perovskite/silicon tandem PV modules [243], [244].

In Figure 6.7 it was shown that solar cells with lower efficiencies (and lower breakdown voltages) generally imply higher energy yields for PV modules that are mounted on partially shaded rooftops. A different trend is expected in large scale PV installations, since lower cell efficiencies have a much more direct (and negative) impact on the energy yield in the absence of shading. However, it must be noted that, even in this case, low breakdown voltage solar cells could be beneficial due to the improved performance under random shading (e.g., due to bird droppings and uneven soiling) and the increased module reliability associated with lower cell temperatures.

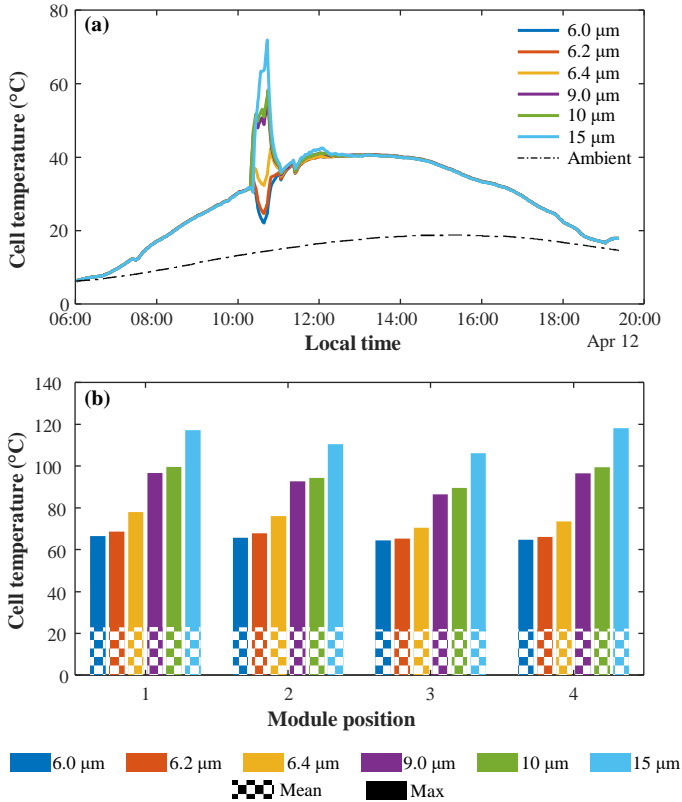


Figure 6.8: Simulated cell temperature. (a) Temperature profile of the solar cell coloured in red in Figure 6.5a during a clear sky day. (b) Mean and maximum temperatures of all the cells in the modules during one entire typical meteorological year in the Netherlands.

6.5. EXPERIMENTAL VALIDATION

Outdoor experiments were conducted to validate the simulation framework used in the previous section and to measure the effect of the breakdown voltage on the shading tolerance of PV modules.

Each module consists of 96 solar cells arranged in 6 sub-strings⁴, where each sub-string is connected in anti-parallel to a Schottky bypass diode as depicted in Figure 6.9a. For a direct comparison between the electrical performance of both PV modules under partial shading, these had to be built with cells of the same size. The first module, referred to as IBC, was built with commercially available 5-inch c-Si IBC solar cells with a breakdown voltage close to 3 V. The second module, referred to as FBC, was built with 5-inch front/back contacted c-Si Al-BSF solar cells with a breakdown voltage larger than 10 V. The two PV modules used during the experiments were laminated with the recipes in Table 6.2.

⁴This particular PV module topology was decided based on the size limitations the PV laminator which has a maximum area of 65 cm by 65 cm.

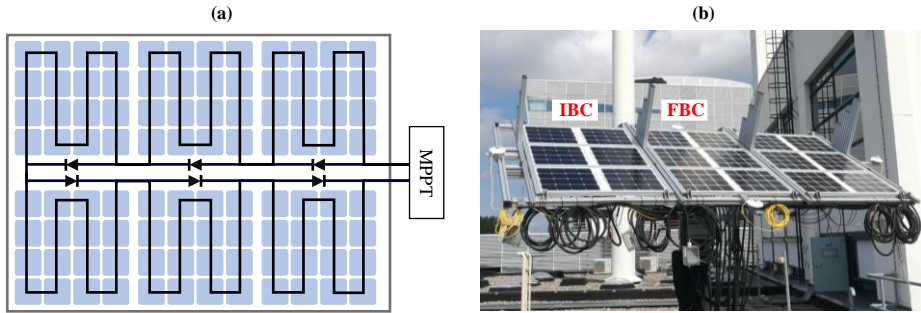


Figure 6.9: Experimental setup. (a) Layout and electrical interconnection of the manufactured PV modules with 96 solar cells and 6 bypass diodes. (b) Photograph of the installation with the 2 monitored PV module.

	FBC	IBC
Front glass	Albarino T (4 mm)	Albarino T (4 mm)
Front encapsulant	3M EVA9110T	3M EVA9110T
Active layer	Al-BSF mono c-Si 2BB	SunPower Gen III
Rear encapsulant	3M EVA9110T	3M EVA9110T
Backsheet	Icosolar PPF	Icosolar PPF

Table 6.2: Bill of materials of the laminated PV modules.

The characteristics of the solar cells are summarised in Table 6.3. Even though commercially available FBC solar cells based on PERC, TOPCon and HJT technologies can achieve higher efficiencies than the chosen Al-BSF cell, newer cells are generally manufactured using 6-inch or larger wafers. Considering that the breakdown voltages of newer FBC technologies are larger than 10 V [214], [245], it is reasonable to assume that the conclusions reached in these experiments are also applicable to newer FBC cell technologies.

	P_{mpp} (W)	V_{mpp} (V)	I_{mpp} (A)	V_{oc} (V)	i_{sc} (A)	Area (cm ²)	BDV (V)	K_P (%/K)	K_V (%/K)	K_I (%/K)
FBC	2.79	0.527	5.29	0.628	5.67	155	>10	-0.46	-0.356	0.024
IBC	3.84	0.634	6.06	0.724	6.43	155	3.0	-0.29	-0.240	0.045

Table 6.3: Characteristics of the solar cells used during the experiments. K_P , K_V and K_I are the temperature coefficients for the maximum power, the open-circuit voltage and the short-circuit current, respectively. The reported breakdown voltage (BDV) was measured in dark and at 2 A.

Prior to the outdoor experiments the PV modules were characterised at Eternalsun Spire's facilities using an A+A+A+ flash simulator and at the PVMD facilities using a Large Area Steady State solar simulator. Then, the two PV modules were installed on a rack at the PVMD monitoring station in Delft as shown in Figure 6.9b. The temperature and output power of the PV modules were monitored between May and August 2021 using

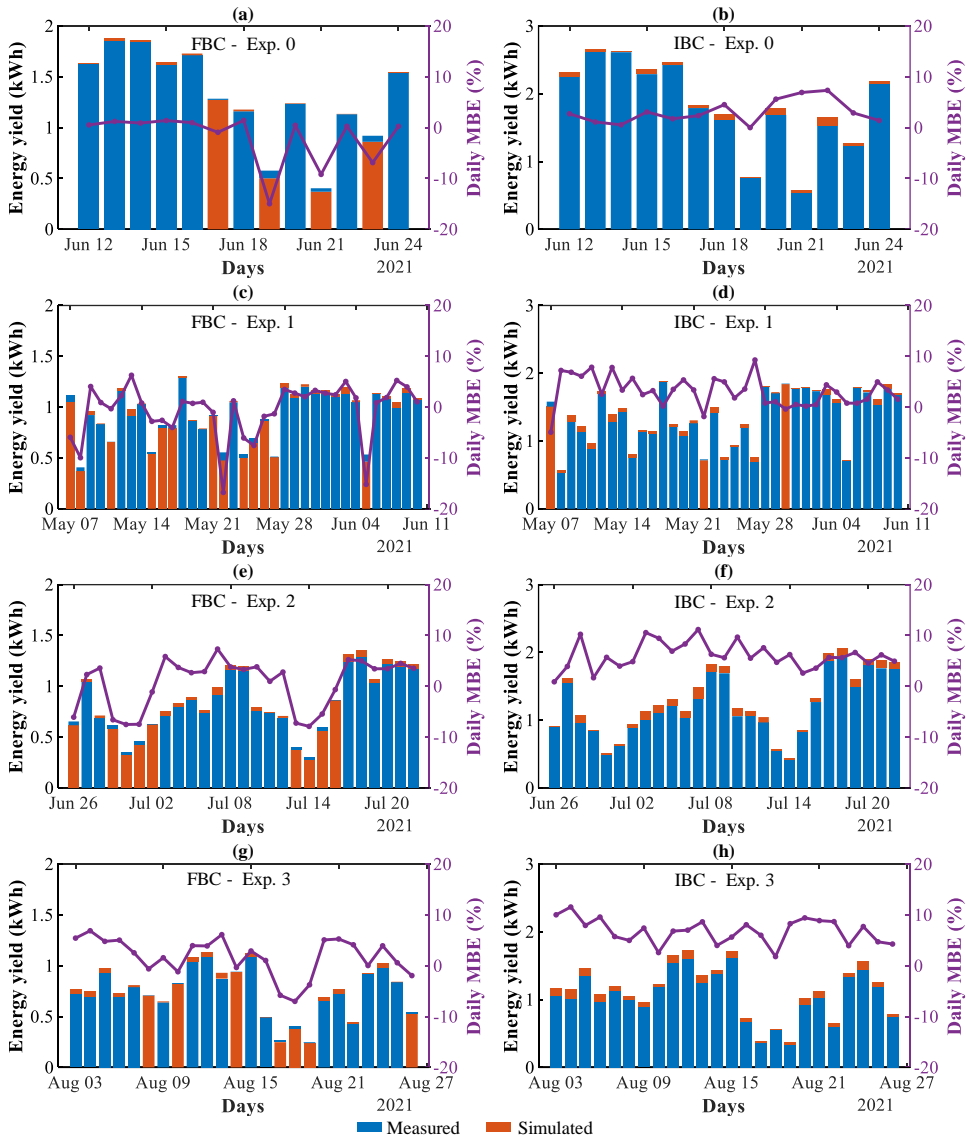


Figure 6.10: Measured and simulated PV module daily DC yield. (a) to (h) Daily energy yield and mean bias error (MBE) during each of the four shading experiments in Figure 6.9 for the FBC and IBC PV modules. The measured and simulated yields are plotted as stacked bars, where the bottom bar represents the lowest of the two values, and the top top bar (sometimes indistinguishable) represents the difference between both values.

K-type thermocouples and two LPVO MP1010F-1 MPPT tracking units [204], which measured the I-V curves of the PV module at every minute and used an MPPT algorithm in between I-V sweeps. During this period the four shading experiments presented in Figure 5.17 were evaluated. In experiment 0 the PV modules were unshaded, whereas in

experiments 1 to 3, the PV modules were partially shaded during every day by structures attached to the mounting rack.

Along with the measurements, the performance of the PV modules was simulated using the same energy yield framework as in Section 6.4. The direct normal irradiance, the diffuse horizontal irradiance, the wind speed and the ambient temperature were measured at the monitoring station and used as inputs to the numerical simulations. The simulated maximum power of the modules was compared to the maximum power point extracted from the measured I-V curves.

As shown in Figure 6.10, in general the simulations were in excellent agreement with the measurements. The overall mean bias error (MBE) between the simulated and measured electrical power during the whole experimental campaign was 1.2 % and 4.6 % for the FBC and the IBC modules, respectively. A detailed comparison between the measured and simulated daily yields is shown in Figures 6.10a to 6.10h, where the low daily MBE values demonstrate the high accuracy of the simulation framework.

Further details are shown in Figure 6.11, where the measured and simulated power time series of Experiment 1 are compared during a clear sky day. In Figure 6.11a, when the bypass diodes in the FBC module start (or stop) conducting, they cause a sudden decrease (or increase) in the output power, which is reflected as steps. On the contrary, these steps are not observable in the output power profile of the IBC module in Figure 6.11b, which is much smoother because the low breakdown voltage allow the IBC cells to become progressively reverse biased while the bypass diodes remain non-conductive.

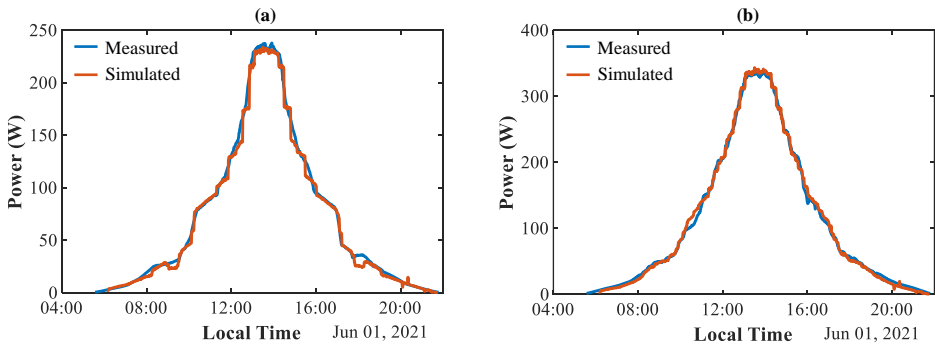


Figure 6.11: Measured and simulated maximum power point time-series in a clear sky day during Experiment 1. (a) Output power of the FBC module. (b) Output power of the IBC module.

The tested modules differ both in breakdown voltage and efficiency. Therefore, in order to compare results, the energy yield obtained during each of the experiments was normalised by the power at Standard Test Conditions (STC) of the corresponding module to quantify the performance improvement due to the breakdown voltage. The resulting specific yields are presented in Table 6.4.

During experiment 0, when the modules were unshaded, the specific yield of the IBC module was 4.3 % higher than that of the FBC module. This can be explained considering that: (1) the IBC module has a significantly better temperature coefficient than the FBC

module; (2) the IBC module operates at slightly lower temperatures due to a higher cell efficiency; and (3) the IBC cells present an improved angular response compared to the FBC cells due to an improved anti-reflective coating (ARC) and front texturing.

However, during experiments 1 to 3, when the modules were partially shaded, the relative difference between the specific yield of both modules was on average 4.2 % compared to experiment 0. This additional gain in specific yield can be mainly attributed to the improved shading tolerance of the IBC module.

	Partially shaded time (%)	FBC yield (Wh/Wp)	IBC yield (Wh/Wp)	Gain (%)
Experiment 0	0	67.0	69.9	4.3
Experiment 1	34	129.7	139.9	7.9
Experiment 2	24	91.0	99.1	9.0
Experiment 3	30	71.8	78.0	8.6

Table 6.4: Comparison between measured specific yields. The STC power of the FBC module is 250.6 W and the STC power of the IBC module is 346.0 W. The gain is calculated taking the FBC yield as a reference.

Unfortunately, the temperature measurements of shaded solar cells did not show clear differences as in Figure 6.8a. After a careful analysis, it was found that the main reason was that the algorithm in the MPPT tracking units failed to find the true maximum power point when the PV modules were partially shaded. Instead, the modules were operated at voltages higher than the maximum power point voltage and most of the time the shaded cells were not driven into reverse bias (except during the brief intervals when the I-V curves were traced). This puts in evidence that, to benefit from the shading tolerance of PV modules with low breakdown voltage and PV modules with many bypass diodes, MPPT algorithms need to be properly engineered to be more effective at finding the global maximum power point.

Finally, after 6 months of continuous operation, the PV modules were measured again and compared to measurements taken prior to the outdoor experiments to verify possible degradation. Post-experiment degradation was measured at EternalSun Spire's facilities using a A+A+A+ flash simulator calibrated with reference samples that had been measured after lamination and were stored in a dark place (at open circuit) while performing the outdoor experiments. The measured degradation of the efficiency of the 6 blocks of cells in the IBC module, was between 2.0 % and 2.5 % relative. While high degradation (up to 10 % relative) has been reported in homojunction IBC cells after prolonged operation in strong reverse bias in the laboratory [246], those testing conditions did not naturally occur during the outdoor experiments in this study. Furthermore, considering that at least two of the blocks of cells in the IBC module in Figure 6.9 were mostly unshaded, it is likely that different effects (other than the operation in reverse bias) have also contributed to the degradation of the tested solar cells [247], [248].

6.6. CONCLUSIONS

In this chapter, the relevance of the breakdown voltage of solar cells to the electrical and thermal performance of partially shaded PV modules was studied.

First, device-level simulations were presented to analyse the performance of reverse biased TOPCon IBC solar cells. The results of the simulation suggest that the reduction of breakdown voltage in TOPCon IBC solar cells is possible by shortening the distance between the emitter and the BSE, without creating a shunt that would degrade the conversion efficiency of the cell.

Then, using the I-V curves of simulated solar cells, system-level simulations of partially shaded PV modules were performed. From the analysis of the results it was concluded that if the breakdown voltage of the solar cells can be reduced to 0.3 V, the energy yield of a PV module with 3 bypass diodes that is shaded approximately 20 % of the time could be boosted up to 20 %. In addition, system-level simulations indicate that low breakdown voltages can help to significantly reduce the temperature increase in reverse biased solar cells.

Finally, to support the results of the simulations, outdoor experiments were conducted using a PV module made with commercially available IBC solar cells with low BDV and a reference PV module with FBC solar cells and six bypass diodes. Three shading scenarios were evaluated during which the PV modules were exposed to partial shading conditions for about 30 % of the time. It was found that after 3 months, the specific yield of the PV module made with IBC cells with a breakdown voltage of 3 V was 4.2 % higher than the reference PV module with FBC solar cells.

The results reported in this chapter put forward additional reasons, beyond the high conversion efficiencies, to promote the market adoption of IBC technology.

7

CONCLUSION AND OUTLOOK

7.1. CONCLUSIONS

The first part of this work was dedicated to the development of simulation models for computing the irradiation and irradiance on PV systems in urban environments. In Chapter 2 the focus was on finding the best locations to install PV systems in the urban environment, whereas in Chapter 3 the characteristics of the solar radiation at a given location were calculated in higher detail.

More specifically, in Chapter 2, a simplified model for the calculation of the solar irradiation in urban environments was proposed, which can be useful for evaluating the best locations to install specific PV systems. The model is based on two indicators, the sky view factor and the sun coverage factor, and five correlation coefficients that depend on the local climate. The indicators can be quickly calculated knowing the sun path and the shape of the skyline profile. As correlation coefficients only need to be generated once for a given surface orientation, when the potential of the same PV system needs to be calculated at a large number of locations, the irradiation model implies a significant reduction in computational effort compared to time-resolved approaches.

The estimation error of the irradiation model was evaluated using the measured annual yield of several residential PV systems and it was found that that the error in the estimated annual irradiation was below 10 % in all the cases. However, as the sun coverage factor is not an irradiance weighted parameter, larger deviations are expected for surfaces with low solar energy potential. Therefore, a more detailed model is required to accurately simulate the performance of urban PV systems after the locations with the highest solar potential are identified.

In Chapter 3, a simulation approach for calculating the irradiance incident on PV systems in complex geometric environments was proposed. The approach is based on a backward ray tracer and allows for the decoupling of the solution of the ray tracing problem from the reflectivity of the surfaces in the scene and the illumination conditions. This approach not only implies a reduction in computation time compared to conventional ray tracing simulation approaches, but it also has two main additional advantages.

First, it enables the simulation. And second, it allows to simulate surfaces with time-varying optical properties improving the calculation of the reflected irradiance on PV modules. For these reasons, the proposed approach is well-suited for simulating bifacial and tandem PV systems. The accuracy of this approach was evaluated using different irradiance sensors installed at the PVMD monitoring station over a period of 6 months. The resulting overall mean bias error was lower than 0.1 % and the mean bias error in the daily irradiation was lower than 0.6 %. It is clear that the very small errors obtained in this particular validation study cannot be generalised for other locations or climates. Nevertheless, the reported results indicate that the proposed approach preserves the high accuracy of (conventional) state-of-the-art ray tracing models.

The second part of this work was dedicated to the analysis and improvement of the shading tolerance of PV modules to maximise the yield of partially shaded PV systems in the urban environment.

In Chapter 4, 49 different PV module topologies, including some that are commercially available, were analysed under various shading scenarios and climates. The comparison was performed using a squared approximation of the I-V curves to reduce the simulation time. The results showed that module-level power electronics can provide high shading tolerance to PV systems when shading is caused by objects far from the modules, such as neighbouring buildings. However, when shading is caused by nearby objects, such as chimneys, dormers or trees, the module topology plays an important role in defining the shading tolerance of the entire PV system. It was determined that in comparison to conventional all-series PV modules, PV modules with one bypass element per cell can generate up to 15 % more energy per year, series-parallel modules can increase the annual yield up to 25 %, and half-cut cell modules can boost the yearly energy output up to 10 %. The DC yield trends presented in this chapter can be valuable to PV module manufacturers when performing cost-benefit analyses of new shade resilient topologies based on the number of bypass elements and groups of parallel strings in a PV module.

In Chapter 5, the concept of reconfigurable PV generators was explored to maximise the energy yield of partially shaded PV systems. A series-parallel reconfigurable PV module with 96 solar cells, a switching matrix and a reconfiguration algorithm were proposed. First, the results of a detailed simulation study indicated that this design could deliver up to 12.7 % more energy than a shade tolerant module with 6 bypass diodes that is partially shaded about 30 % of the time. Next, a prototype of the proposed PV module was built and tested to evaluate its performance in the field. Outdoor measurements revealed that, in the absence of shading, the reconfigurable PV module performed 1.9 % worse than the reference module with 6 bypass diodes and fixed interconnections due to additional resistive losses. Instead, when the modules were partially shaded about 28 % of the time, the reconfigurable PV module delivered in average 10.2 % more energy than the reference module. A deeper analysis of the operation modes of the reconfigurable module revealed that the all-parallel configuration, which is the most shading tolerant but also the one that delivers the highest currents, generated about 40 % of the total energy during the experiments where the module was partially shaded. The analysis also showed that the all-parallel configuration can be avoided to restrict the electrical operating range of the reconfigurable module at the expense of a reduction in the shading

tolerance.

Finally, in Chapter 6 emphasis was placed on the reverse characteristics of solar cells and how they affect the shading tolerance of PV modules. In particular, the breakdown behaviour of TOPCon IBC structure was studied through detailed device-level simulations, which indicated that by shortening the distance between the emitter and the BSF regions, it might be possible to reduce the breakdown voltage (to a certain extent) without sacrificing the conversion efficiency. Subsequently, the reduction in breakdown voltage was translated into energy yield gain by performing system-level simulations. The presented simulation results indicate that by reducing the breakdown voltage of solar cells down to 0.3 V, the energy yield of a conventional PV module that is partially shaded 20% of the time could be increased by about 20%. Moreover, thermal simulations provided indications that low breakdown voltages can help to substantially reduce the temperature increase in shaded solar cells that become reverse biased. Lastly, outdoor experiments were conducted using two full-size PV modules with 6 bypass diodes made with different cell technologies, namely IBC cells with a breakdown voltage of 3 V and FBC cells with a breakdown voltage larger than 10 V. A comparison between both modules after 3 months of operation showed that the specific yield of module with low breakdown voltage solar cells was 4.2% higher. These findings provide compelling evidence that solar cells with low breakdown voltages can significantly boost the shading tolerance of photovoltaic systems.

7.2. OUTLOOK

This thesis presented findings and insights into the modelling, design and optimisation of photovoltaic systems. While the results reported herein demonstrate progress in the field, there remains considerable scope for further research. The following recommendations are put forward:

- The ray tracing approach for simulating solar irradiance in complex geometric environments introduced in Chapter 2 should be implemented applying the latest computer graphics techniques to enable cell-level simulations of PV modules. Scaling approaches could also be investigated to extend the application of the proposed approach to improve the accuracy and expand the capabilities of simulation software for commercial and utility scale PV power plants. Moreover, further experiments are necessary to evaluate the model accuracy on surfaces with very low irradiance levels, such as the rear side of bifacial PV modules that are mounted very close to the ground.
- The above-mentioned ray tracing approach can enable fast and accurate spectral irradiance simulations when combined with models that can describe the spectral radiance of different types of skies. Recent studies show progress in modelling clear-sky spectral radiance, future work should also focus on improving models for intermediate and cloudy skies. This could imply a significant leap towards the accurate simulation of future tandem modules.
- Overall, the proposed reconfigurable PV module concept shows potential for optimising the energy yield of partially shaded PV systems. However, the viability of

this concept hinges on the feasibility of designing an efficient and sufficiently inexpensive power converter that is compatible with the wide output range of the reconfigurable module. This work has clearly established the DC yield gain that can be expected at the output terminals of the module. Further research should determine whether the calculated DC gains are enough to merit the cost of designing a suitable power converter.

- Reducing the breakdown voltage of solar cells appears to be a promising method for making shading tolerant PV modules without requiring significant alterations to current PV module production lines. Nevertheless, it might imply significant modifications to current manufacturing processes of solar cells. The feasibility and cost of these modifications need to be studied in detail to unlock the benefits described in this work.

ACKNOWLEDGEMENTS

I have come to the end of quite an eventful journey, a mix of enriching, rewarding, challenging and frustrating experiences, especially due to the outbreak of the COVID-19 pandemic. However, what I have learnt, and most of all, the people that I have met, made all the grind totally worth it. Therefore, I would like to express my sincere gratitude to my promotors, Prof.dr. Olindo Isabella and Prof.dr. Miro Zeman for providing me with the opportunity to work on this project. Their insightful feedback has been crucial in shaping my research and helping me to overcome many challenges. I am also thankful to Olindo not only for his supervision during the initial stages of my PhD, but also for his efforts to improve the visibility of my work.

I am also deeply grateful to my copromotor and supervisor, Dr. Patrizio Manganiello, for his guidance and support during the most demanding phase of my PhD. Certainly, his knowledge and mentorship have been crucial in this journey, but above all, I praise his empathy and his efforts to allow me to focus on my research.

A special mention also goes to my supervised students: Raoul, Ruben, David, Ben and Viswambher. Their hard work and enthusiasm were key to this project. I am grateful for their contributions and especially for their positive attitude and constructive feedback.

Without a doubt, I have been very fortunate to be surrounded by many excellent people throughout my PhD years, who have offered me their help without expecting anything in return. There were many people indeed, including post-docs, PhD students, technicians, professors, master students and industry partners. Whether the help was in the form of an instruction, sharing a paper, fixing a piece of equipment, quickly reading a paragraph I wrote, helping with a dry run, or just giving me some honest feedback, I am sincerely thankful to all of them. I do not intend to offend anyone, but I also do not want to write an endless list with their names. I would find that too impersonal and especially boring. Instead, I will always offer my help in return, or for those who prefer something more tangible, a fine drink whenever we meet again.

I would also like to thank my friends, the ones who I have known for a long time, and those who I have met during the six years that I have lived in the Netherlands. I cherish every meal, game, party, trip and coffee break that we spent together. They have cheered me up, borne my complaints, helped me relax, and made me a happier person. They understand better than anyone, that I would not write here a list of names to express how much I value our friendship and their support over the past years.

As always, I must mention my parents, who have provided me with endless opportunities and unconditional support throughout my life. Their sacrifices have been the foundation of my achievements and I am forever grateful for their love and belief in me.

Last but not least, I want acknowledge my wife, Rita. I never imagined I would find the love of my life and the mother of my son at work, right behind my screen. Meeting her was definitely the most amazing and happiest occurrence during my PhD, and

I believe this is yet another evidence that the most marvellous things in life cannot be modelled. Her feedback, her help with proofreading, and the time that she spent listening to me when I needed to think out loud are just the tip of the iceberg. Without her love, emotional support and tremendous patience, this journey would have been three thousand five hundred fifty-two times more difficult.

BIBLIOGRAPHY

- [1] Intergovernmental Panel on Climate Change, *Climate Change 2022: Mitigation of Climate Change*, Accessed: 2023-1-1, 2022. [Online]. Available: https://www.ipcc.ch/report/ar6/wg3/downloads/report/IPCC_AR6_WGIII_SPM.pdf.
- [2] BP p.l.c., *bp Statistical Review of World Energy*, 71st ed., Accessed: 2022-01-10, 2022. [Online]. Available: <https://www.bp.com/content/dam/bp/business-sites/en/global/corporate/pdfs/energy-economics/statistical-review/bp-stats-review-2022-full-report.pdf>.
- [3] IRENA, *Renewable Energy Statistics 2022*, International Renewable Energy Agency, 2022. [Online]. Available: <https://www.irena.org/publications/2022/Jul/Renewable-Energy-Statistics-2022>.
- [4] International Energy Agency, *Solar PV*, Accessed: 2023-01-10, 2022. [Online]. Available: <https://www.iea.org/reports/solar-pv>.
- [5] International Energy Agency, *World Energy Outlook 2022 Free Dataset*, Accessed: 2022-12-12, 2022. [Online]. Available: <https://www.iea.org/data-and-statistics/data-product/world-energy-outlook-2022-free-dataset#data-files>.
- [6] P. Frankl, S. Nowak, M. Gutschner, S. Gnos, and T. Rinke, “Technology roadmap: Solar photovoltaic energy”, *International Energy Association*, 2010.
- [7] T. Huld, K. Bódis, I. Pinedo Pascua, E. Dunlop, N. Taylor, and A. Jäger-Waldau, “The Rooftop Potential for PV Systems in the European Union to deliver the Paris Agreement”, *European Energy Innovation*, vol. Spring 2018, pp. 12–15, Mar. 2018.
- [8] P. Gagnon, R. Margolis, J. Melius, C. Phillips, and R. Elmore, “Rooftop Solar Photovoltaic Technical Potential in the United States. A Detailed Assessment”, National Renewable Energy Laboratory, Tech. Rep. NREL/TP-6A20-65298, 2016. DOI: [10.2172/1236153](https://doi.org/10.2172/1236153).
- [9] S. Freitas and M. C. Brito, “Solar façades for future cities”, *Renewable Energy Focus*, vol. 31, pp. 73–79, 2019, ISSN: 1755-0084. DOI: [10.1016/j.ref.2019.09.002](https://doi.org/10.1016/j.ref.2019.09.002).
- [10] H.-M. Neumann, D. Schär, and F. Baumgartner, “The potential of photovoltaic carports to cover the energy demand of road passenger transport”, *Progress in Photovoltaics: Research and Applications*, vol. 20, no. 6, pp. 639–649, 2012. DOI: [10.1002/pip.1199](https://doi.org/10.1002/pip.1199).
- [11] T. Santos, K. Lobato, J. Rocha, and J. A. Tenedório, “Modeling photovoltaic potential for bus shelters on a city-scale: A case study in lisbon”, *Applied Sciences*, vol. 10, no. 14, p. 4801, 2020. DOI: [10.3390/app10144801](https://doi.org/10.3390/app10144801).

- [12] Tesla, Inc., *Solar roof*, Accessed: 2023-01-01, 2016. [Online]. Available: <https://www.tesla.com/solarroof>.
- [13] C. J. Traverse, R. Pandey, M. C. Barr, and R. R. Lunt, "Emergence of highly transparent photovoltaics for distributed applications", *Nature Energy*, vol. 2, no. 11, pp. 849–860, 2017. DOI: [10.1038/s41560-017-0016-9](https://doi.org/10.1038/s41560-017-0016-9).
- [14] G. Yu, H. Yang, D. Luo, X. Cheng, and M. K. Ansah, "A review on developments and researches of building integrated photovoltaic (bipv) windows and shading blinds", *Renewable and Sustainable Energy Reviews*, vol. 149, 2021. DOI: [10.1016/j.rser.2021.111355](https://doi.org/10.1016/j.rser.2021.111355).
- [15] J. C. Ortiz Lizcano, Z. Haghghi, S. Wapperom, *et al.*, "Photovoltaic chimney: Thermal modeling and concept demonstration for integration in buildings", *Progress in Photovoltaics: Research and Applications*, vol. 28, no. 6, pp. 465–482, 2020. DOI: [10.1002/pip.3194](https://doi.org/10.1002/pip.3194).
- [16] D. Sailor, J. Anand, and R. King, "Photovoltaics in the built environment: A critical review", *Energy and Buildings*, vol. 253, p. 111 479, 2021. DOI: [10.1016/j.enbuild.2021.111479](https://doi.org/10.1016/j.enbuild.2021.111479).
- [17] T. Baumann, H. Nussbaumer, M. Klenk, A. Dreisiebner, F. Carigiet, and F. Baumgartner, "Photovoltaic systems with vertically mounted bifacial pv modules in combination with green roofs", *Solar Energy*, vol. 190, pp. 139–146, 2019. DOI: [10.1016/j.solener.2019.08.014](https://doi.org/10.1016/j.solener.2019.08.014).
- [18] D. Aelenei, R. A. Lopes, L. Aelenei, and H. Gonçalves, "Investigating the potential for energy flexibility in an office building with a vertical bipv and a pv roof system", *Renewable Energy*, vol. 137, pp. 189–197, 2019. DOI: [10.1016/j.renene.2018.07.140](https://doi.org/10.1016/j.renene.2018.07.140).
- [19] H. Takebayashi, E. Ishii, M. Moriyama, A. Sakaki, S. Nakajima, and H. Ueda, "Study to examine the potential for solar energy utilization based on the relationship between urban morphology and solar radiation gain on building rooftops and wall surfaces", *Solar Energy*, vol. 119, pp. 362–369, 2015. DOI: [10.1016/j.solener.2015.05.039](https://doi.org/10.1016/j.solener.2015.05.039).
- [20] R. Giridharan, S. Ganesan, and S. Lau, "Daytime urban heat island effect in high-rise and high-density residential developments in hong kong", *Energy and Buildings*, vol. 36, no. 6, pp. 525–534, 2004. DOI: [10.1016/j.enbuild.2003.12.016](https://doi.org/10.1016/j.enbuild.2003.12.016).
- [21] M. Koehl, S. Hamperl, and M. Heck, "Effect of thermal insulation of the back side of pv modules on the module temperature", *Progress in Photovoltaics: Research and Applications*, vol. 24, no. 9, pp. 1194–1199, 2016. DOI: [10.1002/pip.2773](https://doi.org/10.1002/pip.2773).
- [22] A. Gok, E. Ozkalay, G. Friesen, and F. Frontini, "The influence of operating temperature on the performance of bipv modules", *IEEE Journal of Photovoltaics*, vol. 10, no. 5, pp. 1371–1378, 2020. DOI: [10.1109/jphotov.2020.3001181](https://doi.org/10.1109/jphotov.2020.3001181).
- [23] J. Kaldellis and A. Kokala, "Quantifying the decrease of the photovoltaic panels' energy yield due to phenomena of natural air pollution disposal", *Energy*, vol. 35, no. 12, pp. 4862–4869, 2010. DOI: [10.1016/j.energy.2010.09.002](https://doi.org/10.1016/j.energy.2010.09.002).

- [24] I. Peters, S. Karthik, H. Liu, T. Buonassisi, and A. Nobre, “Urban haze and photovoltaics”, *Energy & Environmental Science*, vol. 11, no. 10, pp. 3043–3054, 2018. DOI: [10.1039/c8ee01100a](https://doi.org/10.1039/c8ee01100a).
- [25] C. Ballif, L.-E. Perret-Aebi, S. Lufkin, and E. Rey, “Integrated thinking for photovoltaics in buildings”, *Nature Energy*, vol. 3, no. 6, pp. 438–442, 2018. DOI: [10.1038/s41560-018-0176-2](https://doi.org/10.1038/s41560-018-0176-2).
- [26] N. Skandalos and D. Karamanis, “PV glazing technologies”, *Renewable and Sustainable Energy Reviews*, vol. 49, pp. 306–322, 2015. DOI: [10.1016/j.rser.2015.04.145](https://doi.org/10.1016/j.rser.2015.04.145).
- [27] A. C. Martins, V. Chapuis, A. Virtuani, and C. Ballif, “Ultra-lightweight PV module design for building integrated photovoltaics”, in *44th IEEE Photovoltaic Specialists Conference (PVSC)*, IEEE, 2017, pp. 2104–2108. DOI: [10.1109/pvsc.2017.8366791](https://doi.org/10.1109/pvsc.2017.8366791).
- [28] A. E. Ostfeld and A. C. Arias, “Flexible photovoltaic power systems: Integration opportunities, challenges and advances”, *Flexible and Printed Electronics*, vol. 2, no. 013001, 2017. DOI: [10.1088/2058-8585/aa5750](https://doi.org/10.1088/2058-8585/aa5750).
- [29] K. H. Anderson, M. H. Coddington, and B. D. Kroposki, “Assessing technical potential for city PV deployment using NREL’s in my backyard tool”, in *35th IEEE Photovoltaic Specialists Conference (PVSC)*, IEEE, 2010, pp. 1085–1090. DOI: [10.1109/pvsc.2010.5614697](https://doi.org/10.1109/pvsc.2010.5614697).
- [30] J. M. Espeche, F. Noris, Z. Lennard, S. Challet, and M. Machado, “PVSITES: Building integrated photovoltaic technologies and systems for large-scale market deployment”, *Multidisciplinary Digital Publishing Institute Proceedings*, vol. 1, no. 7, 2017. DOI: [10.3390/proceedings1070690](https://doi.org/10.3390/proceedings1070690).
- [31] R. Compagnon, “Solar and daylight availability in the urban fabric”, *Energy and buildings*, vol. 36, no. 4, pp. 321–328, 2004. DOI: [10.1016/j.enbuild.2004.01.009](https://doi.org/10.1016/j.enbuild.2004.01.009).
- [32] K. Lagios, J. Niemasz, and C. F. Reinhart, “Animated building performance simulation (ABPS)—linking Rhinoceros/Grasshopper with Radiance/Daysim”, *Proceedings of SimBuild*, vol. 4, no. 1, pp. 321–327, 2010.
- [33] J. H. Kämpf, M. Montavon, J. Bunyesc, R. Bolliger, and D. Robinson, “Optimisation of buildings’ solar irradiation availability”, *Solar energy*, vol. 84, no. 4, pp. 596–603, 2010. DOI: [10.1016/j.solener.2009.07.013](https://doi.org/10.1016/j.solener.2009.07.013).
- [34] M. C. Brito, N. Gomes, T. Santos, and J. A. Tenedório, “Photovoltaic potential in a lisbon suburb using lidar data”, *Solar Energy*, vol. 86, no. 1, pp. 283–288, 2012. DOI: [10.1016/j.solener.2011.09.031](https://doi.org/10.1016/j.solener.2011.09.031).
- [35] G. Agugiaro, F. Nex, F. Remondino, R. De Filippi, S. Droghetti, and C. Furlanello, “Solar radiation estimation on building roofs and web-based solar cadastre”, *ISPRS Ann. Photogramm. Remote Sens. Spat. Inf. Sci.*, vol. 1, pp. 177–182, 2012. DOI: [10.5194/isprsannals-I-2-177-2012](https://doi.org/10.5194/isprsannals-I-2-177-2012).

- [36] S. Freitas, C. Catita, P. Redweik, and M. C. Brito, “Modelling solar potential in the urban environment: State-of-the-art review”, *Renewable and Sustainable Energy Reviews*, vol. 41, pp. 915–931, 2015. DOI: [10.1016/j.rser.2014.08.060](https://doi.org/10.1016/j.rser.2014.08.060).
- [37] F. Lindberg, P. Jonsson, T. Honjo, and D. Wästberg, “Solar energy on building envelopes—3d modelling in a 2d environment”, *Solar Energy*, vol. 115, pp. 369–378, 2015. DOI: [10.1016/j.solener.2015.03.001](https://doi.org/10.1016/j.solener.2015.03.001).
- [38] C. Carneiro, E. Morello, G. Desthieux, F. Golay, *et al.*, “Urban environment quality indicators: Application to solar radiation and morphological analysis on built area”, in *3rd WSEAS international conference on Visualization, imaging and simulation*, WSEAS, 2010, pp. 141–148. DOI: <https://dl.acm.org/doi/10.5555/1950211.1950236>.
- [39] J. A. Jakubiec and C. F. Reinhart, “Towards validated urban photovoltaic potential and solar radiation maps based on lidar measurements, gis data, and hourly daysim simulations”, *Proceedings of SimBuild*, vol. 5, no. 1, pp. 628–637, 2012.
- [40] D. Robinson, “Urban morphology and indicators of radiation availability”, *Solar Energy*, vol. 80, no. 12, pp. 1643–1648, 2006. DOI: [10.1016/j.solener.2006.01.007](https://doi.org/10.1016/j.solener.2006.01.007).
- [41] L. R. Rodríguez, E. Duminil, J. S. Ramos, and U. Eicker, “Assessment of the photovoltaic potential at urban level based on 3d city models: A case study and new methodological approach”, *Solar Energy*, vol. 146, pp. 264–275, 2017. DOI: [10.1016/j.solener.2017.02.043](https://doi.org/10.1016/j.solener.2017.02.043).
- [42] J. A. Davies and J. E. Hay, “Calculation of the solar radiation incident on an inclined surface”, in *First Canadian Solar Radiation Data Workshop*, 1978, pp. 59–72.
- [43] C. Chatzipoulka, R. Compagnon, J. Kaempf, and M. Nikolopoulou, “Sky view factor as predictor of solar availability on building façades”, *Solar Energy*, vol. 170, pp. 1026–1038, 2018. DOI: [10.1016/j.solener.2018.06.028](https://doi.org/10.1016/j.solener.2018.06.028).
- [44] C. Demain, M. Journée, and C. Bertrand, “Evaluation of different models to estimate the global solar radiation on inclined surfaces”, *Renewable Energy*, vol. 50, pp. 710–721, 2013. DOI: [10.1016/j.renene.2012.07.031](https://doi.org/10.1016/j.renene.2012.07.031).
- [45] A. H. Smets, O. Isabella, M. Zeman, *et al.*, *Solar energy: the physics and engineering of photovoltaic conversion technologies and systems*. UIT, 2016.
- [46] R. Perez, P. Ineichen, R. Seals, J. Michalsky, and R. Stewart, “Modeling daylight availability and irradiance components from direct and global irradiance”, *Solar energy*, vol. 44, no. 5, pp. 271–289, 1990. DOI: [10.1016/0038-092x\(90\)90055-h](https://doi.org/10.1016/0038-092x(90)90055-h).
- [47] R. Perez, R. Seals, P. Ineichen, R. Stewart, and D. Menicucci, “A new simplified version of the perez diffuse irradiance model for tilted surfaces”, *Solar energy*, vol. 39, no. 3, pp. 221–231, 1987. DOI: [10.1016/S0038-092X\(87\)80031-2](https://doi.org/10.1016/S0038-092X(87)80031-2).
- [48] Meteotest, *Meteonorm Handbook Part II: Theory*, Version 7.2, Jul. 2017.
- [49] Y. Tian, R. Davies-Colley, P. Gong, and B. Thorrold, “Estimating solar radiation on slopes of arbitrary aspect”, *Agricultural and Forest Meteorology*, vol. 109, no. 1, pp. 67–74, 2001. DOI: [10.1016/S0168-1923\(01\)00245-3](https://doi.org/10.1016/S0168-1923(01)00245-3).

- [50] J. Rakovec and K. Zakšek, "On the proper analytical expression for the sky-view factor and the diffuse irradiation of a slope for an isotropic sky", *Renewable Energy*, vol. 37, no. 1, pp. 440–444, 2012. DOI: [10.1016/j.renene.2011.06.042](https://doi.org/10.1016/j.renene.2011.06.042).
- [51] Cesar. "Cesar database". accessed: 2018-02-02. (2013), [Online]. Available: <http://www.cesar-database.nl/>.
- [52] R. Perez, R. Seals, and J. Michalsky, "All-weather model for sky luminance distribution - Preliminary configuration and validation", *Solar energy*, vol. 50, no. 3, pp. 235–245, 1993. DOI: [10.1016/0038-092X\(93\)90017-I](https://doi.org/10.1016/0038-092X(93)90017-I).
- [53] M. K. Fuentes, "A simplified thermal model for flat-plate photovoltaic arrays", Sandia National Laboratories, Tech. Rep. SAND-85-0330, May 1987.
- [54] W. Xiao, W. G. Dunford, and A. Capel, "A novel modeling method for photovoltaic cells", in *Power Electronics Specialists Conference, 2004. PESC 04. 2004 IEEE 35th Annual*, IEEE, vol. 3, 2004, pp. 1950–1956. DOI: [10.1109/PESC.2004.1355416](https://doi.org/10.1109/PESC.2004.1355416).
- [55] F. Lasnier and T. G. Ang, *Photovoltaic engineering handbook*. CRC Press, 1990.
- [56] A. Jain and A. Kapoor, "A new method to determine the diode ideality factor of real solar cell using lambert w-function", *Solar energy materials and solar cells*, vol. 85, no. 3, pp. 391–396, 2005. DOI: [10.1016/j.solmat.2004.05.022](https://doi.org/10.1016/j.solmat.2004.05.022).
- [57] Meteotest, *Meteonorm Handbook Part I: Software*, Version 7.2, Dec. 2017.
- [58] A. Carr and T. Pryor, "A comparison of the performance of different PV module types in temperate climates", *Solar Energy*, vol. 76, no. 1-3, pp. 285–294, 2004. DOI: [10.1016/j.solener.2003.07.026](https://doi.org/10.1016/j.solener.2003.07.026).
- [59] T. Gál, F. Lindberg, and J. Unger, "Computing continuous sky view factors using 3d urban raster and vector databases: Comparison and application to urban climate", *Theoretical and applied climatology*, vol. 95, pp. 111–123, 2009. DOI: [10.1007/s00704-007-0362-9](https://doi.org/10.1007/s00704-007-0362-9).
- [60] S. An, B. Kim, H. Lee, *et al.*, "Three-dimensional point cloud based sky view factor analysis in complex urban settings", *International Journal of Climatology*, vol. 34, no. 8, pp. 2685–2701, 2014. DOI: [10.1002/joc.3868](https://doi.org/10.1002/joc.3868).
- [61] Actueel Hoogtebestand Nederland. "Ahn viewer". Accessed: 2018-01-12. (2013), [Online]. Available: <https://www.ahn.nl/ahn-viewer1>.
- [62] B. Marion, J. Adelstein, K. Boyle, *et al.*, "Performance parameters for grid connected PV systems", in *31st IEEE Photovoltaic Specialists Conference (PVSC)*, IEEE, 2005, pp. 1601–1606. DOI: [10.1109/pvsc.2005.1488451](https://doi.org/10.1109/pvsc.2005.1488451).
- [63] PVOutput. "Live Photovoltaic data". Accessed: 2018-09-21. (2013), [Online]. Available: <http://www.pvoutput.org/>.
- [64] Australian Government Bureau of Meteorology. "Monthly mean daily global solar exposure". Accessed: 2018-02-02. (2018), [Online]. Available: <http://www.bom.gov.au/>.
- [65] J. S. Stein, "The photovoltaic Performance Modeling Collaborative (PVPMC)", in *38th IEEE Photovoltaic Specialists Conference (PVSC)*, IEEE, 2012, pp. 3048–3052. DOI: [10.1109/pvsc.2012.6318225](https://doi.org/10.1109/pvsc.2012.6318225).

- [66] M. Theristis, N. Riedel-Lyngskær, J. S. Stein, *et al.*, “Blind photovoltaic modeling intercomparison: A multidimensional data analysis and lessons learned”, *Progress in Photovoltaics: Research and Applications*, 2023. DOI: [10.1002/pip.3729](https://doi.org/10.1002/pip.3729).
- [67] J. Kanters and M. Horvat, “Solar energy as a design parameter in urban planning”, *Energy Procedia*, vol. 30, pp. 1143–1152, 2012. DOI: [10.1016/j.egypro.2012.11.127](https://doi.org/10.1016/j.egypro.2012.11.127).
- [68] M. Amado and F. Poggi, “Solar urban planning: A parametric approach”, *Energy Procedia*, vol. 48, pp. 1539–1548, 2014. DOI: [10.1016/j.egypro.2014.02.174](https://doi.org/10.1016/j.egypro.2014.02.174).
- [69] F. De Luca, “Solar Form Finding: Subtractive Solar Envelope and Integrated Solar Collection Computational Method for High-rise Buildings in Urban Environments”, in *37th Annual Conference of the Association for Computer Aided Design in Architecture*, Nov. 2017, pp. 212–221. DOI: [10.52842/conf.acadia.2017.212](https://doi.org/10.52842/conf.acadia.2017.212).
- [70] C. Kutter, F. Basler, L. E. Alanis, J. Markert, M. Heinrich, and D. H. Neuhaus, “Integrated lightweight, glass-free PV module technology for box bodies of commercial trucks”, in *37th European Photovoltaic Solar Energy Conference and Exhibition (EU PVSEC)*, 2020, pp. 1711–1718. DOI: [10.4229/eupvsec20202020-6D0.11.6](https://doi.org/10.4229/eupvsec20202020-6D0.11.6).
- [71] M. C. Brito, T. Santos, F. Moura, D. Pera, and J. Rocha, “Urban solar potential for vehicle integrated photovoltaics”, *Transportation Research Part D: Transport and Environment*, vol. 94, 2021. DOI: [10.1016/j.trd.2021.102810](https://doi.org/10.1016/j.trd.2021.102810).
- [72] United Nations, *Sustainable development goals*, Accessed: 2021-10-20, 2016. [Online]. Available: <https://www.un.org/sustainabledevelopment/energy/>.
- [73] B. Y. Liu and R. C. Jordan, “The long-term average performance of flat-plate solar-energy collectors: with design data for the US, its outlying possessions and Canada”, *Solar energy*, vol. 7, no. 2, pp. 53–74, 1963. DOI: [10.1016/0038-092X\(63\)90006-9](https://doi.org/10.1016/0038-092X(63)90006-9).
- [74] D. Reindl, W. Beckman, and J. Duffie, “Evaluation of hourly tilted surface radiation models”, *Solar energy*, vol. 45, no. 1, pp. 9–17, 1990. DOI: [10.1016/0038-092X\(90\)90061-G](https://doi.org/10.1016/0038-092X(90)90061-G).
- [75] M. Lave, W. Hayes, A. Pohl, and C. W. Hansen, “Evaluation of global horizontal irradiance to plane-of-array irradiance models at locations across the united states”, *IEEE Journal of Photovoltaics*, vol. 5, no. 2, pp. 597–606, 2015. DOI: [10.1109/jphotov.2015.2392938](https://doi.org/10.1109/jphotov.2015.2392938).
- [76] P. Ineichen, O. Guisan, and R. Perez, “Ground-reflected radiation and albedo”, *Solar Energy*, vol. 44, no. 4, pp. 207–214, 1990. DOI: [10.1016/0038-092X\(90\)90149-7](https://doi.org/10.1016/0038-092X(90)90149-7).
- [77] A. Mermoud and B. Wittmer, “Bifacial shed simulation with PVSyst”, in *Bifacial Workshop*, 2017, pp. 25–26.
- [78] B. Marion, S. MacAlpine, C. Deline, *et al.*, “A practical irradiance model for bifacial PV modules”, in *44th IEEE Photovoltaic Specialists Conference (PVSC)*, IEEE, 2017, pp. 1537–1542. DOI: [10.1016/S0378-7788\(01\)00058-5](https://doi.org/10.1016/S0378-7788(01)00058-5).

- [79] K. Jäger, P. Tillmann, and C. Becker, “Detailed illumination model for bifacial solar cells”, *Optics Express*, vol. 28, no. 4, pp. 4751–4762, 2020. DOI: [10.1364/oe.383570](https://doi.org/10.1364/oe.383570).
- [80] U. A. Yusufoglu, T. M. Pletzer, L. J. Koduvelikulathu, C. Comparotto, R. Kopecek, and H. Kurz, “Analysis of the annual performance of bifacial modules and optimization methods”, *IEEE Journal of Photovoltaics*, vol. 5, no. 1, pp. 320–328, 2014. DOI: [10.1109/jphotov.2014.2364406](https://doi.org/10.1109/jphotov.2014.2364406).
- [81] I. Shoukry, J. Libal, R. Kopecek, E. Wefringhaus, and J. Werner, “Modelling of bifacial gain for stand-alone and in-field installed bifacial PV modules”, *Energy Procedia*, vol. 92, pp. 600–608, 2016. DOI: [10.1016/j.egypro.2016.07.025](https://doi.org/10.1016/j.egypro.2016.07.025).
- [82] C. W. Hansen, R. Gooding, N. Guay, *et al.*, “A detailed model of rear-side irradiance for bifacial PV modules”, in *44th IEEE Photovoltaic Specialists Conference (PVSC)*, IEEE, 2017, pp. 1543–1548. DOI: [10.1109/pvsc.2017.8366707](https://doi.org/10.1109/pvsc.2017.8366707).
- [83] D. Chudinzow, J. Haas, G. Díaz-Ferrán, S. Moreno-Leiva, and L. Eltrop, “Simulating the energy yield of a bifacial photovoltaic power plant”, *Solar Energy*, vol. 183, pp. 812–822, 2019. DOI: [10.1016/j.solener.2019.03.071](https://doi.org/10.1016/j.solener.2019.03.071).
- [84] A. Asgharzadeh Shishavan and F. Toor, *COMSOL Models - Ray Tracing Work at the University of Iowa*, <https://pvpmc.sandia.gov/pv-research/bifacial-pv-project/bifacial-pv-performance-models/ray-tracing-models-for-backside-irradiance/comsol-models/>, Accessed: 2023-02-06, PV Performance Modeling Collaborative (SNL), 2020.
- [85] *Ray optics module user’s guide*, version Version 5.4, Comsol, 2018.
- [86] C. W. Hansen, J. S. Stein, C. Deline, *et al.*, “Analysis of irradiance models for bifacial PV modules”, in *43rd IEEE Photovoltaic Specialists Conference (PVSC)*, IEEE, 2016, pp. 138–143. DOI: [10.1109/pvsc.2016.7749564](https://doi.org/10.1109/pvsc.2016.7749564).
- [87] S. A. Pelaez, C. Deline, S. M. MacAlpine, B. Marion, J. S. Stein, and R. K. Kostuk, “Comparison of bifacial solar irradiance model predictions with field validation”, *IEEE Journal of Photovoltaics*, vol. 9, no. 1, pp. 82–88, 2018. DOI: [10.1109/jphotov.2018.2877000](https://doi.org/10.1109/jphotov.2018.2877000).
- [88] R. Santbergen, V. A. Muthukumar, R. M. E. Valckenborg, W. J. A. van de Wall, A. H. M. Smets, and M. Zeman, “Calculation of irradiance distribution on PV modules by combining sky and sensitivity maps”, *Solar Energy*, vol. 150, pp. 49–54, 2017. DOI: [10.1016/j.solener.2017.04.036](https://doi.org/10.1016/j.solener.2017.04.036).
- [89] C. Deline and S. Ayala, *Bifacial_Radiance. computer software*. National Renewable Energy Laboratory, 2021. DOI: [10.11578/dc.20180530.16](https://doi.org/10.11578/dc.20180530.16).
- [90] J. Mardaljevic, “Daylight simulation: Validation, sky models and daylight coefficients”, Ph.D. dissertation, Loughborough University, 2020. [Online]. Available: <https://hdl.handle.net/2134/23356>.
- [91] S. Subramaniam, “Parametric modeling strategies for efficient annual analysis of daylight in buildings”, Ph.D. dissertation, The Pennsylvania State University, 2018. [Online]. Available: <https://etda.libraries.psu.edu/catalog/15229sxs1106>.

- [92] I. Horvath, P. Manganiello, H. Goverde, *et al.*, “Towards efficient and accurate energy yield modelling of bifacial PV systems”, in *35th European Photovoltaic Solar Energy Conference and Exhibition (EU PVSEC)*, 2018.
- [93] J. Freeman, D. Freestate, W. Hobbs, and C. Riley, “Using measured plane-of-array data directly in photovoltaic modeling: Methodology and validation”, in *43rd IEEE Photovoltaic Specialists Conference (PVSC)*, IEEE, 2016, pp. 2653–2656. DOI: [10.1109/pvsc.2016.7750130](https://doi.org/10.1109/pvsc.2016.7750130).
- [94] R. Mubarak, M. Hofmann, S. Riechelmann, and G. Seckmeyer, “Comparison of modelled and measured tilted solar irradiance for photovoltaic applications”, *Energies*, vol. 10, no. 11, 2017. DOI: [10.3390/en10111688](https://doi.org/10.3390/en10111688).
- [95] S. A. Khalil and A. Shaffie, “Evaluation of transposition models of solar irradiance over Egypt”, *Renewable and Sustainable Energy Reviews*, vol. 66, pp. 105–119, 2016. DOI: [10.1016/j.rser.2016.06.066](https://doi.org/10.1016/j.rser.2016.06.066).
- [96] D. Berrian and J. Libal, “A comparison of ray tracing and view factor simulations of locally resolved rear irradiance with the experimental values”, *Progress in Photovoltaics: Research and Applications*, vol. 28, no. 6, pp. 609–620, 2020. DOI: [10.1002/pip.3261](https://doi.org/10.1002/pip.3261).
- [97] H. Nussbaumer, G. Janssen, D. Berrian, *et al.*, “Accuracy of simulated data for bifacial systems with varying tilt angles and share of diffuse radiation”, *Solar Energy*, vol. 197, pp. 6–21, 2020. DOI: [10.1016/j.solener.2019.12.071](https://doi.org/10.1016/j.solener.2019.12.071).
- [98] U. Gross, K. Spindler, and E. Hahne, “Shapefactor-equations for radiation heat transfer between plane rectangular surfaces of arbitrary position and size with parallel boundaries”, *Letters in heat and mass transfer*, vol. 8, no. 3, pp. 219–227, 1981. DOI: [10.1016/0094-4548\(81\)90016-3](https://doi.org/10.1016/0094-4548(81)90016-3).
- [99] F. F. Sönmez, H. Ziar, O. Isabella, and M. Zeman, “Fast and accurate ray-casting-based view factor estimation method for complex geometries”, *Solar Energy Materials and Solar Cells*, vol. 200, no. 15, 2019. DOI: [10.1016/j.solmat.2019.109934](https://doi.org/10.1016/j.solmat.2019.109934).
- [100] F. Bartell, E. Dereniak, and W. Wolfe, “The theory and measurement of bidirectional reflectance distribution function (BRDF) and bidirectional transmittance distribution function (BTDF)”, in *Radiation scattering in optical systems*, International Society for Optics and Photonics, vol. 257, 1981, pp. 154–160. DOI: [10.1117/12.959611](https://doi.org/10.1117/12.959611).
- [101] PV Lighthouse, *Sunsolve*, Accessed: 2021-07-19, 2021. [Online]. Available: <https://www.pvlighthouse.com.au/sunsolve>.
- [102] H. Holst, M. Winter, M. R. Vogt, *et al.*, “Application of a new ray tracing framework to the analysis of extended regions in si solar cell modules”, *Energy Procedia*, vol. 38, pp. 86–93, 2013. [Online]. Available: <https://www.daidalos-cloud.de>.

- [103] M. Winter, M. R. Vogt, H. Holst, and P. P. Altermatt, “Combining structures on different length scales in ray tracing: Analysis of optical losses in solar cell modules”, *Optical and Quantum Electronics*, vol. 47, no. 6, pp. 1373–1379, 2015. DOI: [10.1007/s11082-014-0078-x](https://doi.org/10.1007/s11082-014-0078-x).
- [104] R. Santbergen, T. Meguro, T. Suezaki, G. Koizumi, K. Yamamoto, and M. Zeman, “GenPro4 optical model for solar cell simulation and its application to multijunction solar cells”, *IEEE journal of photovoltaics*, vol. 7, no. 3, pp. 919–926, 2017. [Online]. Available: <https://asa.ewi.tudelft.nl/>.
- [105] G. J. Ward, “The RADIANCE lighting simulation and rendering system”, in *21st annual conference on Computer graphics and interactive techniques*, 1994, pp. 459–472. DOI: [10.1145/192161.192286](https://doi.org/10.1145/192161.192286).
- [106] S. A. Pelaez, C. Deline, P. Greenberg, J. S. Stein, and R. K. Kostuk, “Model and validation of single-axis tracking with bifacial PV”, *IEEE Journal of Photovoltaics*, vol. 9, no. 3, pp. 715–721, 2019. DOI: [10.1109/jphotov.2019.2892872](https://doi.org/10.1109/jphotov.2019.2892872).
- [107] P. R. Tregenza and I. M. Waters, “Daylight coefficients”, *Lighting Research & Technology*, vol. 15, no. 2, pp. 65–71, 1983. DOI: [10.1177/096032718301500201](https://doi.org/10.1177/096032718301500201).
- [108] C. F. Reinhart and O. Walkenhorst, “Validation of dynamic Radiance-based daylight simulations for a test office with external blinds”, *Energy and buildings*, vol. 33, no. 7, pp. 683–697, 2001. DOI: [10.1016/S0378-7788\(01\)00058-5](https://doi.org/10.1016/S0378-7788(01)00058-5).
- [109] N. Riedel-Lyngskær, M. Ribaconka, M. Pó, *et al.*, “The effect of spectral albedo in bifacial photovoltaic performance”, *Solar Energy*, vol. 231, pp. 921–935, 2022. DOI: [10.1016/j.solener.2021.12.023](https://doi.org/10.1016/j.solener.2021.12.023).
- [110] M. Brennan, A. Abramase, R. W. Andrews, and J. M. Pearce, “Effects of spectral albedo on solar photovoltaic devices”, *Solar Energy Materials and Solar Cells*, vol. 124, pp. 111–116, 2014. DOI: [10.1016/j.solmat.2014.01.046](https://doi.org/10.1016/j.solmat.2014.01.046).
- [111] C. Monokroussos, Q. Gao, X. Zhang, *et al.*, “Rear-side spectral irradiance at 1 sun and application to bifacial module power rating”, *Progress in Photovoltaics: Research and Applications*, vol. 28, no. 8, pp. 755–766, 2020. DOI: [10.1002/pip.3268](https://doi.org/10.1002/pip.3268).
- [112] M. T. Hörantner and H. J. Snaith, “Predicting and optimising the energy yield of perovskite-on-silicon tandem solar cells under real world conditions”, *Energy & Environmental Science*, vol. 10, no. 9, pp. 1983–1993, 2017. DOI: [10.1039/C7EE01232B](https://doi.org/10.1039/C7EE01232B).
- [113] N. Lindsay, Q. Libois, J. Badosa, A. Migan-Dubois, and V. Bourdin, “Errors in PV power modelling due to the lack of spectral and angular details of solar irradiance inputs”, *Solar Energy*, vol. 197, pp. 266–278, 2020. DOI: [10.1016/j.solener.2019.12.042](https://doi.org/10.1016/j.solener.2019.12.042).
- [114] M. Gul, Y. Kotak, T. Muneer, and S. Ivanova, “Enhancement of albedo for solar energy gain with particular emphasis on overcast skies”, *Energies*, vol. 11, no. 11, 2018. DOI: [10.3390/en11112881](https://doi.org/10.3390/en11112881).

- [115] N. Riedel-Lyngskær, M. Ribaconka, M. Pó, *et al.*, “Spectral Albedo in Bifacial Photovoltaic Modeling: What can be learned from Onsite Measurements?”, in *48th IEEE Photovoltaic Specialists Conference (PVSC)*, IEEE, 2021, pp. 1335–1338. DOI: [10.1109/PVSC43889.2021.9519085](https://doi.org/10.1109/PVSC43889.2021.9519085).
- [116] G. Ward and R. Shakespeare, “Rendering with radiance: The art and science of lighting visualization”, in 3rd ed. 1998, ch. Calculation methods, pp. 491–562.
- [117] T. Möller and B. Trumbore, “Fast, minimum storage ray-triangle intersection”, *Journal of graphics tools*, vol. 2, no. 1, pp. 21–28, 1997. DOI: [10.1145/1198555.1198746](https://doi.org/10.1145/1198555.1198746).
- [118] J. S. Bartlett, Á. M. Ciotti, R. F. Davis, and J. J. Cullen, “The spectral effects of clouds on solar irradiance”, *Journal of Geophysical Research: Oceans*, vol. 103, no. C13, pp. 31 017–31 031, 1998. DOI: [10.1029/1998JC900002](https://doi.org/10.1029/1998JC900002).
- [119] R. E. Bird and C. Riordan, “Simple solar spectral model for direct and diffuse irradiance on horizontal and tilted planes at the earth’s surface for cloudless atmospheres”, *Journal of Applied Meteorology and Climatology*, vol. 25, no. 1, pp. 87–97, 1986. DOI: [10.2172/5986936](https://doi.org/10.2172/5986936).
- [120] L. Hosek and A. Wilkie, “An analytic model for full spectral sky-dome radiance”, *ACM Transactions on Graphics (TOG)*, vol. 31, no. 4, pp. 1–9, 2012. DOI: [10.1145/2185520.2185591](https://doi.org/10.1145/2185520.2185591).
- [121] J. T. Kider Jr, D. Knowlton, J. Newlin, Y. K. Li, and D. P. Greenberg, “A framework for the experimental comparison of solar and skydome illumination”, *ACM Transactions on Graphics (TOG)*, vol. 33, no. 6, pp. 1–12, 2014. DOI: [10.1145/2661229.2661259](https://doi.org/10.1145/2661229.2661259).
- [122] M. Winter, H. Holst, M. R. Vogt, and P. P. Altermatt, “Impact of realistic illumination on optical losses in Si solar cell modules compared to standard testing conditions”, in *31st European Photovoltaic Solar Energy Conference and Exhibition (EU PVSEC)*, 2015, pp. 1869–1874. DOI: [10.4229/eupvsec20152015-5D0.11.3](https://doi.org/10.4229/eupvsec20152015-5D0.11.3).
- [123] M. Ernst, H. Holst, M. Winter, and P. P. Altermatt, “SunCalculator: A program to calculate the angular and spectral distribution of direct and diffuse solar radiation”, *Solar Energy Materials and Solar Cells*, vol. 157, pp. 913–922, 2016. DOI: [10.1016/j.solmat.2016.08.008](https://doi.org/10.1016/j.solmat.2016.08.008).
- [124] C. Gueymard, “SMARTS2, a simple model of the atmospheric radiative transfer of sunshine: algorithms and performance assessment”, Florida Solar Energy Center Cocoa, FL, Tech. Rep. FSEC-PF-270-95, 1995.
- [125] C. A. Gueymard, “Parameterized transmittance model for direct beam and circumsolar spectral irradiance”, *Solar Energy*, vol. 71, no. 5, pp. 325–346, 2001. DOI: [10.1016/S0038-092X\(01\)00054-8](https://doi.org/10.1016/S0038-092X(01)00054-8).
- [126] C. A. Gueymard, D. Myers, and K. Emery, “Proposed reference irradiance spectra for solar energy systems testing”, *Solar energy*, vol. 73, no. 6, pp. 443–467, 2002. DOI: [10.1016/S0038-092X\(03\)00005-7](https://doi.org/10.1016/S0038-092X(03)00005-7).

- [127] P. Ricchiazzi, S. Yang, C. Gautier, and D. Sowle, "Sbdart: A research and teaching software tool for plane-parallel radiative transfer in the earth's atmosphere", *Bulletin of the American Meteorological Society*, vol. 79, no. 10, pp. 2101–2114, 1998. DOI: [10.1175/1520-0477\(1998\)079%3C2101:SARATS%3E2.0.CO;2](https://doi.org/10.1175/1520-0477(1998)079%3C2101:SARATS%3E2.0.CO;2).
- [128] S. Boppana, K. Passow, J. Sorensen, B. H. King, and C. Robinson, "Impact of uncertainty in IAM measurement on energy predictions", in *7th IEEE World Conference on Photovoltaic Energy Conversion (WCPEC)*, IEEE, 2018, pp. 2276–2281. DOI: [10.1109/pvsc.2018.8548024](https://doi.org/10.1109/pvsc.2018.8548024).
- [129] P. Gilman, A. Dobos, N. DiOrio, J. Freeman, S. Janzou, and D. Ryberg, "SAM photovoltaic model technical reference update", National Renewable Energy Laboratory, Tech. Rep. NREL/TP-6A20-67399, 2018. DOI: [10.2172/1429291](https://doi.org/10.2172/1429291).
- [130] R. L. Cook, "Stochastic sampling in computer graphics", *ACM Transactions on Graphics (TOG)*, vol. 5, no. 1, pp. 51–72, 1986. DOI: [10.1145/7529.8927](https://doi.org/10.1145/7529.8927).
- [131] G. J. Ward, F. M. Rubinstein, and R. D. Clear, "A ray tracing solution for diffuse interreflection", in *15th annual conference on Computer graphics and interactive techniques*, 1988, pp. 85–92. DOI: [10.1145/378456.378490](https://doi.org/10.1145/378456.378490).
- [132] S. Subramaniam, "Daylighting simulations with Radiance using matrix-based methods", *Lawrence Berkeley National Laboratory*, 2017.
- [133] A. M. Baldridge, S. Hook, C. Grove, and G. Rivera, "The ASTER spectral library version 2.0", *Remote Sensing of Environment*, vol. 113, no. 4, pp. 711–715, 2009. DOI: [10.1016/j.rse.2008.11.007](https://doi.org/10.1016/j.rse.2008.11.007).
- [134] S. K. Meerdink, S. J. Hook, D. A. Roberts, and E. A. Abbott, "The ECOSTRESS spectral library version 1.0", *Remote Sensing of Environment*, vol. 230, 2019. DOI: [10.1016/j.rse.2019.05.015](https://doi.org/10.1016/j.rse.2019.05.015).
- [135] W. De Soto, S. A. Klein, and W. A. Beckman, "Improvement and validation of a model for photovoltaic array performance", *Solar energy*, vol. 80, no. 1, pp. 78–88, 2006. DOI: [10.1016/j.solener.2005.06.010](https://doi.org/10.1016/j.solener.2005.06.010).
- [136] S. Karki, H. Ziar, M. Korevaar, T. Bergmans, J. Mes, and O. Isabella, "Performance Evaluation of Silicon-Based Irradiance Sensors Versus Thermopile Pyranometer", *IEEE Journal of Photovoltaics*, vol. 11, no. 1, pp. 144–149, 2020. DOI: [10.1109/jphotov.2020.3038342](https://doi.org/10.1109/jphotov.2020.3038342).
- [137] D. M. Kammen and D. A. Sunter, "City-integrated renewable energy for urban sustainability", *Science*, vol. 352, no. 6288, pp. 922–928, 2016. DOI: [10.1126/science.aad9302](https://doi.org/10.1126/science.aad9302).
- [138] IRENA, *Renewable power generation costs in 2018*, Abu Dhabi: International Renewable Energy Agency, 2018.
- [139] C. Kost, S. Shammugam, V. Jülch, H.-T. Nguyen, and T. Schlegl, "Levelized cost of electricity renewable energy technologies", *Fraunhofer Institute for Solar Energy Systems*, 2018.
- [140] A. Jäger-Waldau, "PV status report 2019", Institute for Energy and Transport, Renewable Energy Unit, Tech. Rep. JRC118058, 2019.

- [141] D. Feldman, V. Ramasamy, R. Fu, A. Ramdas, J. Desai, and R. Margolis, "U.S. Solar Photovoltaic System and Energy Storage Cost Benchmark: Q1 2020", National Renewable Energy Laboratory, Tech. Rep. NREL/TP-6A20-77324, 2021. DOI: [10.2172/1765601](https://doi.org/10.2172/1765601).
- [142] U. Jahn and W. Nasse, "Operational performance of grid-connected PV systems on buildings in germany", *Progress in Photovoltaics: Research and Applications*, vol. 12, no. 6, pp. 441–448, 2004. DOI: [10.1002/pip.550](https://doi.org/10.1002/pip.550).
- [143] M. Swaleh and M. Green, "Effect of shunt resistance and bypass diodes on the shadow tolerance of solar cell modules", *Solar cells*, vol. 5, no. 2, pp. 183–198, 1982. DOI: [10.1016/0379-6787\(82\)90026-6](https://doi.org/10.1016/0379-6787(82)90026-6).
- [144] S. Silvestre, A. Boronat, and A. Chouder, "Study of bypass diodes configuration on PV modules", *Applied Energy*, vol. 86, no. 9, pp. 1632–1640, 2009. DOI: [10.1016/j.apenergy.2009.01.020](https://doi.org/10.1016/j.apenergy.2009.01.020).
- [145] R. G. Vieira, F. M. de Araújo, M. Dhimish, and M. I. Guerra, "A comprehensive review on bypass diode application on photovoltaic modules", *Energies*, vol. 13, no. 10, 2020. DOI: [10.3390/en13102472](https://doi.org/10.3390/en13102472).
- [146] J. Bauer, D. Lausch, H. Blumtritt, N. Zakharov, and O. Breitenstein, "Avalanche breakdown in multicrystalline solar cells due to preferred phosphorous diffusion at extended defects", *Progress in Photovoltaics: Research and Applications*, vol. 21, no. 7, pp. 1444–1453, 2013. DOI: [10.1002/pip.2220](https://doi.org/10.1002/pip.2220).
- [147] M. Alonso-García and J. Ruíz, "Analysis and modelling the reverse characteristic of photovoltaic cells", *Solar Energy Materials and Solar Cells*, vol. 90, no. 7-8, pp. 1105–1120, 2006. DOI: [10.1016/j.solmat.2005.06.006](https://doi.org/10.1016/j.solmat.2005.06.006).
- [148] O. Breitenstein, J. Bauer, K. Bothe, *et al.*, "Understanding junction breakdown in multicrystalline solar cells", *Journal of applied physics*, vol. 109, no. 7, 2011. DOI: [10.1063/1.3562200](https://doi.org/10.1063/1.3562200).
- [149] K. Sinapis, C. Tzikas, G. Litjens, *et al.*, "A comprehensive study on partial shading response of c-si modules and yield modeling of string inverter and module level power electronics", *Solar Energy*, vol. 135, pp. 731–741, 2016. DOI: [10.1016/j.solener.2016.06.050](https://doi.org/10.1016/j.solener.2016.06.050).
- [150] C. Deline, J. Meydbray, M. Donovan, and J. Forrest, "Photovoltaic shading testbed for module-level power electronics", National Renewable Energy Laboratory, Tech. Rep. NREL/TP-5200-54876, 2012. DOI: [10.2172/1045715](https://doi.org/10.2172/1045715).
- [151] H. A. Sher and K. E. Addoweesh, "Micro-inverters - promising solutions in solar photovoltaics", *Energy for Sustainable Development*, vol. 16, no. 4, pp. 389–400, 2012. DOI: [10.1016/j.esd.2012.10.002](https://doi.org/10.1016/j.esd.2012.10.002).
- [152] R. Hasan, S. Mekhilef, M. Seyedmahmoudian, and B. Horan, "Grid-connected isolated PV microinverters: A review", *Renewable and Sustainable Energy Reviews*, vol. 67, pp. 1065–1080, 2017. DOI: [10.1016/j.rser.2016.09.082](https://doi.org/10.1016/j.rser.2016.09.082).

- [153] S. M. MacAlpine, R. W. Erickson, and M. J. Brandemuehl, "Characterization of power optimizer potential to increase energy capture in photovoltaic systems operating under nonuniform conditions", *IEEE Transactions on Power Electronics*, vol. 28, no. 6, pp. 2936–2945, 2012. DOI: [10.1109/tpe.2012.2226476](https://doi.org/10.1109/tpe.2012.2226476).
- [154] M. Z. Ramli and Z. Salam, "Performance evaluation of dc power optimizer (DCPO) for photovoltaic (PV) system during partial shading", *Renewable energy*, vol. 139, pp. 1336–1354, 2019. DOI: [10.1016/j.renene.2019.02.072](https://doi.org/10.1016/j.renene.2019.02.072).
- [155] R. Orduz, J. Solórzano, M. Á. Egido, and E. Román, "Analytical study and evaluation results of power optimizers for distributed power conditioning in photovoltaic arrays", *Progress in Photovoltaics: Research and Applications*, vol. 21, no. 3, pp. 359–373, 2013. DOI: [10.1002/pip.1188](https://doi.org/10.1002/pip.1188).
- [156] C. Olalla, D. Maksimovic, C. Deline, and L. Martinez-Salamero, "Impact of distributed power electronics on the lifetime and reliability of PV systems", *Progress in Photovoltaics: Research and Applications*, vol. 25, no. 10, pp. 821–835, 2017. DOI: [10.1002/pip.2893](https://doi.org/10.1002/pip.2893).
- [157] C. Deline, B. Marion, J. Granata, and S. Gonzalez, "Performance and economic analysis of distributed power electronics in photovoltaic systems", National Renewable Energy Laboratory, Tech. Rep. NREL/TP-5200-50003, 2011. DOI: [10.2172/1004490](https://doi.org/10.2172/1004490).
- [158] R. C. N. Pilawa-Podgurski and D. J. Perreault, "Submodule integrated distributed maximum power point tracking for solar photovoltaic applications", *IEEE Transactions on Power Electronics*, vol. 28, no. 6, pp. 2957–2967, 2012. DOI: [10.1109/TPEL.2012.2220861](https://doi.org/10.1109/TPEL.2012.2220861).
- [159] C. Deline, B. Sekulic, J. Stein, S. Barkaszi, J. Yang, and S. Kahn, "Evaluation of maxim module-integrated electronics at the doe regional test centers", in *40th IEEE Photovoltaic Specialist Conference (PVSC)*, IEEE, 2014, pp. 0986–0991. DOI: [10.1109/PVSC.2014.6925080](https://doi.org/10.1109/PVSC.2014.6925080).
- [160] Taylor Technologies BV. "Taylor solar panels". Accessed: 2023-02-02. (2023), [Online]. Available: <https://www.taylor.solar/>.
- [161] K. A. Kim, P. S. Shenoy, and P. T. Krein, "Converter rating analysis for photovoltaic differential power processing systems", *IEEE Transactions on Power Electronics*, vol. 30, no. 4, pp. 1987–1997, 2014. DOI: [10.1109/TPEL.2014.2326045](https://doi.org/10.1109/TPEL.2014.2326045).
- [162] K. Doubleday, B. Choi, D. Maksimovic, C. Deline, and C. Olalla, "Recovery of inter-row shading losses using differential power-processing submodule dc-dc converters", *Solar Energy*, vol. 135, pp. 512–517, 2016. DOI: [10.1016/j.solener.2016.06.013](https://doi.org/10.1016/j.solener.2016.06.013).
- [163] M. Gokdag, M. Akbaba, and O. Gulbudak, "Switched-capacitor converter for pv modules under partial shading and mismatch conditions", *Solar Energy*, vol. 170, pp. 723–731, 2018. DOI: [10.1016/j.solener.2018.06.010](https://doi.org/10.1016/j.solener.2018.06.010).
- [164] B. B. Pannebakker, A. C. de Waal, and W. G. van Sark, "Photovoltaics in the shade: One bypass diode per solar cell revisited", *Progress in Photovoltaics: Research and Applications*, vol. 25, no. 10, pp. 836–849, 2017. DOI: [10.1002/pip.2898](https://doi.org/10.1002/pip.2898).

- [165] H. Hanifi, M. Pander, B. Jaeckel, J. Schneider, A. Bakhtiari, and W. Maier, “A novel electrical approach to protect PV modules under various partial shading situations”, *Solar Energy*, vol. 193, pp. 814–819, 2019. DOI: [10.1016/j.solener.2019.10.035](https://doi.org/10.1016/j.solener.2019.10.035).
- [166] M. Chegaar, A. Hamzaoui, A. Namoda, P. Petit, M. Aillerie, and A. Herguth, “Effect of illumination intensity on solar cells parameters”, *Energy Procedia*, vol. 36, pp. 722–729, 2013. DOI: [10.1016/j.egypro.2013.07.084](https://doi.org/10.1016/j.egypro.2013.07.084).
- [167] A. J. Carr, K. de Groot, M. J. Jansen, *et al.*, “Tessera: Scalable, shade robust module”, in *42nd IEEE Photovoltaic Specialists Conference (PVSC)*, IEEE, 2015, pp. 1–5. DOI: [10.1109/pvsc.2015.7356286](https://doi.org/10.1109/pvsc.2015.7356286).
- [168] F. Lu, S. Guo, T. M. Walsh, and A. G. Aberle, “Improved PV module performance under partial shading conditions”, *Energy Procedia*, vol. 33, pp. 248–255, 2013. DOI: [10.1016/j.egypro.2013.05.065](https://doi.org/10.1016/j.egypro.2013.05.065).
- [169] H. Hanifi, J. Schneider, and J. Bagdahn, “Reduced shading effect on half-cell modules - Measurement and simulation”, in *31st European Photovoltaic Solar Energy Conference and Exhibition (EU PVSEC)*, 2015, pp. 2529–2533. DOI: [10.4229/eupvsec20152015-5cv.2.25](https://doi.org/10.4229/eupvsec20152015-5cv.2.25).
- [170] N. Klasen, D. Weisser, T. Rößler, D. H. Neuhaus, and A. Kraft, “Performance of shingled solar modules under partial shading”, *Progress in Photovoltaics: Research and Applications*, vol. 30, no. 4, pp. 325–338, 2022. DOI: [10.1002/pip.3486](https://doi.org/10.1002/pip.3486).
- [171] E. S. Hasyim, S. Wenham, and M. Green, “Shadow tolerance of modules incorporating integral bypass diode solar cells”, *Solar cells*, vol. 19, no. 2, pp. 109–122, 1986. DOI: [10.1016/0379-6787\(86\)90036-0](https://doi.org/10.1016/0379-6787(86)90036-0).
- [172] H. Ziar, B. Asaei, S. Farhangi, M. Korevaar, O. Isabella, and M. Zeman, “Quantification of shading tolerability for photovoltaic modules”, *IEEE Journal of Photovoltaics*, vol. 7, no. 5, pp. 1390–1399, 2017. DOI: [10.1109/jphotov.2017.2711429](https://doi.org/10.1109/jphotov.2017.2711429).
- [173] M. Mittag, A. Pfreundt, J. Shahid, N. Wöhrle, and D. H. Neuhaus, “Techno-economic analysis of half cell modules: The impact of half cells on module power and costs”, in *36th European Photovoltaic Solar Energy Conference and Exhibition (EU PVSEC)*, 2019, pp. 1032–1039. DOI: [10.4229/eupvsec20192019-4AV.1.20](https://doi.org/10.4229/eupvsec20192019-4AV.1.20).
- [174] B. Lefevre, S. Peeters, J. Poortmans, and J. Driesen, “Predetermined static configurations of a partially shaded photovoltaic module”, *Progress in Photovoltaics: Research and Applications*, vol. 25, no. 2, pp. 149–160, 2017. DOI: [10.1002/pip.2834](https://doi.org/10.1002/pip.2834).
- [175] S. Mishra, H. Ziar, O. Isabella, and M. Zeman, “Selection map for PV module installation based on shading tolerability and temperature coefficient”, *IEEE Journal of Photovoltaics*, vol. 9, no. 3, pp. 872–880, 2019. DOI: [10.1109/jphotov.2019.2900695](https://doi.org/10.1109/jphotov.2019.2900695).
- [176] J. Remund, S. Müller, M. Schmutz, D. Barsotti, C. Studer, and R. Cattin, *Handbook Part I: Software*, version 7.3.4, Meteotest, Mar. 2020.

- [177] AE Solar, *AE Solar Hot-Spot Free MONocrystalline PV Modules*, AES-DS2019, V.002, 2019. [Online]. Available: <https://ae-solar.com/wp-content/uploads/2018/10/AE-M6-60-305W-320W.pdf>.
- [178] W. Eerenstein, M. Jansen, K. de Groot, *et al.*, “TESSERA: Maximizing PV yield performance with size flexibility for BIPV”, in *30th European Photovoltaic Solar Energy Conference and Exhibition (EU PVSEC)*, 2015, pp. 2216–2219. DOI: [10.4229/eupvsec20152015-5BV.2.13](https://doi.org/10.4229/eupvsec20152015-5BV.2.13).
- [179] D. Faiman, “Assessing the outdoor operating temperature of photovoltaic modules”, *Progress in Photovoltaics: Research and Applications*, vol. 16, no. 4, pp. 307–315, 2008. DOI: [10.1002/pip.813](https://doi.org/10.1002/pip.813).
- [180] D. L. King, W. E. Boyson, and J. A. Kratochvill, “Photovoltaic array performance model”, Sandia National Laboratories, Tech. Rep. SAND2004-3535, 2004. DOI: [10.2172/919131](https://doi.org/10.2172/919131).
- [181] M. Wolf, G. Noel, and R. J. Stirn, “Investigation of the double exponential in the current-voltage characteristics of silicon solar cells”, *IEEE Transactions on Electron Devices*, vol. 24, no. 4, pp. 419–428, 1977. DOI: [10.1109/T-ED.1977.18750](https://doi.org/10.1109/T-ED.1977.18750).
- [182] J.-P. Charles, G. Bordure, A. Khoury, and P. Mialhe, “Consistency of the double exponential model with physical mechanisms of conduction for a solar cell under illumination”, *Journal of Physics D: Applied Physics*, vol. 18, no. 11, 1985. DOI: [10.1088/0022-3727/18/11/015](https://doi.org/10.1088/0022-3727/18/11/015).
- [183] D. S. Chan and J. C. Phang, “Analytical methods for the extraction of solar-cell single and double diode model parameters from iv characteristics”, *IEEE Transactions on Electron devices*, vol. 34, no. 2, pp. 286–293, 1987. DOI: [10.1109/t-ed.1987.22920](https://doi.org/10.1109/t-ed.1987.22920).
- [184] K. Ishaque, Z. Salam, H. Taheri, *et al.*, “Modeling and simulation of photovoltaic (PV) system during partial shading based on a two-diode model”, *Simulation Modelling Practice and Theory*, vol. 19, no. 7, pp. 1613–1626, 2011. DOI: [10.1016/j.simpat.2011.04.005](https://doi.org/10.1016/j.simpat.2011.04.005).
- [185] Texas Instruments, *SM74611 Smart Bypass Diode*, SNVS903B, Rev. B, 2012. [Online]. Available: <https://www.ti.com/lit/ds/symlink/sm74611.pdf>.
- [186] R. Chenni, M. Makhoulouf, T. Kerbache, and A. Bouzid, “A detailed modeling method for photovoltaic cells”, *Energy*, vol. 32, no. 9, pp. 1724–1730, 2007. DOI: [10.1016/j.energy.2006.12.006](https://doi.org/10.1016/j.energy.2006.12.006).
- [187] H. Hanifi, D. Dassler, J. Schneider, M. Turek, S. Schindler, and J. Bagdahn, “Optimized tab width in half-cell modules”, *Energy Procedia*, vol. 92, pp. 52–59, 2016. DOI: [10.1016/j.egypro.2016.07.009](https://doi.org/10.1016/j.egypro.2016.07.009).
- [188] R. A. Sherif and K. S. Boutros, *Solar module array with reconfigurable tile*, US Patent 6,350,944, Feb. 2002.
- [189] C. Chang, *Solar cell array having lattice or matrix structure and method of arranging solar cells and panels*, US6635817B2, Oct. 2003.

- [190] G. Velasco-Quesada, F. Guinjoan-Gispert, R. Piqué-López, M. Román-Lumbreras, and A. Conesa-Roca, "Electrical PV array reconfiguration strategy for energy extraction improvement in grid connected PV systems", *IEEE Transactions on Industrial Electronics*, vol. 56, no. 11, pp. 4319–4331, 2009. DOI: [10.1109/tie.2009.2024664](https://doi.org/10.1109/tie.2009.2024664).
- [191] S. Vemuru, P. Singh, and M. Niamat, "Analysis of photovoltaic array with reconfigurable modules under partial shading", in *38th IEEE Photovoltaic Specialists Conference (PVSC)*, IEEE, 2012, pp. 1437–1441. DOI: [10.1109/pvsc.2012.6317867](https://doi.org/10.1109/pvsc.2012.6317867).
- [192] L. Bouselham, B. Hajji, A. Mellit, A. Rabhi, and A. Mazari, "A Reconfigurable PV Architecture Based on New Irradiance Equalization Algorithm", in *Proceedings of the 1st International Conference on Electronic Engineering and Renewable Energy*, B. Hajji, G. M. Tina, K. Ghomid, A. Rabhi, and A. Mellit, Eds., Singapore: Springer Singapore, 2019, pp. 470–477. DOI: [10.1007/978-981-13-1405-6_56](https://doi.org/10.1007/978-981-13-1405-6_56).
- [193] M. Balato, L. Costanzo, and M. Vitelli, "Reconfiguration of PV modules: A tool to get the best compromise between maximization of the extracted power and minimization of localized heating phenomena", *Solar Energy*, vol. 138, pp. 105–118, 2016. DOI: [10.1016/j.solener.2016.09.011](https://doi.org/10.1016/j.solener.2016.09.011).
- [194] G. Spagnuolo, G. Petrone, B. Lehman, C. A. R. Paja, Y. Zhao, and M. L. O. Gutierrez, "Control of photovoltaic arrays: Dynamical reconfiguration for fighting mismatched conditions and meeting load requests", *IEEE industrial electronics magazine*, vol. 9, no. 1, pp. 62–76, 2015. DOI: [10.1109/mie.2014.2360721](https://doi.org/10.1109/mie.2014.2360721).
- [195] D. Nguyen and B. Lehman, "An adaptive solar photovoltaic array using model-based reconfiguration algorithm", *IEEE Transactions on industrial Electronics*, vol. 55, no. 7, pp. 2644–2654, 2008. DOI: [10.1109/tie.2008.924169](https://doi.org/10.1109/tie.2008.924169).
- [196] M. Baka, P. Manganiello, D. Soudris, and F. Catthoor, "A cost-benefit analysis for reconfigurable PV modules under shading", *Solar Energy*, vol. 178, pp. 69–78, 2019. DOI: [10.1016/j.solener.2018.11.063](https://doi.org/10.1016/j.solener.2018.11.063).
- [197] D. La Manna, V. L. Vigni, E. R. Sanseverino, V. Di Dio, and P. Romano, "Reconfigurable electrical interconnection strategies for photovoltaic arrays: A review", *Renewable and Sustainable Energy Reviews*, vol. 33, pp. 412–426, 2014. DOI: [10.1016/j.rser.2014.01.070](https://doi.org/10.1016/j.rser.2014.01.070).
- [198] X. Liu and Y. Wang, "Reconfiguration method to extract more power from partially shaded photovoltaic arrays with series-parallel topology", *Energies*, vol. 12, no. 8, 2019. DOI: [10.3390/en12081439](https://doi.org/10.3390/en12081439).
- [199] M. Alahmad, M. A. Chaaban, S. Kit Lau, J. Shi, and J. Neal, "An adaptive utility interactive photovoltaic system based on a flexible switch matrix to optimize performance in real-time", *Solar Energy*, vol. 86, no. 3, pp. 951–963, 2012. DOI: [10.1016/j.solener.2011.12.028](https://doi.org/10.1016/j.solener.2011.12.028).
- [200] M. Vogt, D. Salokhe, A. Calcabrini, *et al.*, "Novel asynchronous shade detection algorithms for reconfigurable pv modules", in *40th European Photovoltaic Solar Energy Conference and Exhibition (EU PVSEC)*, 2023.

- [201] M. Piliouguine and G. Spagnuolo, "Mismatching and partial shading identification in photovoltaic arrays by an artificial neural network ensemble", *Solar Energy*, vol. 236, pp. 712–723, 2022. DOI: [10.1016/j.solener.2022.03.026](https://doi.org/10.1016/j.solener.2022.03.026).
- [202] A. Hovinen, "Fitting of the solar cell iv-curve to the two diode model", *Physica Scripta*, vol. 1994, no. T54, p. 175, 1994. DOI: [10.1088/0031-8949/1994/t54/043](https://doi.org/10.1088/0031-8949/1994/t54/043).
- [203] S. Guo, J. Singh, I. Peters, A. Aberle, and T. Walsh, "A quantitative analysis of photovoltaic modules using halved cells", *International Journal of Photoenergy*, vol. 2013, 2013. DOI: [10.1155/2013/739374](https://doi.org/10.1155/2013/739374).
- [204] M. Jankovec and M. Topič, *LPVO: PV module monitoring*, <http://lpvo.fe.uni-lj.si/en/services/pv-monitoring/pv-module-monitoring/>, Accessed 2022-04-15.
- [205] M. Köntges, G. Oreski, U. Jahn, M. Herz, P. Hacke, and K.-A. Weiß, *Assessment of Photovoltaic Module Failures in the Field*. International Energy Agency, 2017, ISBN: 978-3-906042-54-1. [Online]. Available: https://iea-pvps.org/wp-content/uploads/2017/09/170515_IEA-PVPS-report_T13-09-2017_Internetversion_2.pdf.
- [206] R. Satpathy and V. Pamuru, "Chapter 5 - manufacturing of crystalline silicon solar pv modules", in *Solar PV Power*, R. Satpathy and V. Pamuru, Eds., Academic Press, 2021, pp. 135–241. DOI: [10.1016/B978-0-12-817626-9.00005-8](https://doi.org/10.1016/B978-0-12-817626-9.00005-8).
- [207] W. G. Shin, S. W. Ko, H. J. Song, Y. C. Ju, H. M. Hwang, and G. H. Kang, "Origin of bypass diode fault in c-si photovoltaic modules: Leakage current under high surrounding temperature", *Energies*, vol. 11, no. 9, p. 2416, 2018. DOI: [10.3390/en11092416](https://doi.org/10.3390/en11092416).
- [208] C. E. Clement, J. P. Singh, E. Birgersson, Y. Wang, and Y. S. Khoo, "Illumination dependence of reverse leakage current in silicon solar cells", *IEEE Journal of Photovoltaics*, vol. 11, no. 5, pp. 1285–1290, 2021. DOI: [10.1109/jphotov.2021.3088005](https://doi.org/10.1109/jphotov.2021.3088005).
- [209] R. Witteck, M. Siebert, S. Blankemeyer, H. Schulte-Huxel, and M. Köntges, "Three bypass diodes architecture at the limit", *IEEE Journal of Photovoltaics*, vol. 10, no. 6, pp. 1828–1838, 2020. DOI: [10.1109/jphotov.2020.3021348](https://doi.org/10.1109/jphotov.2020.3021348).
- [210] M. Simon and E. L. Meyer, "Detection and analysis of hot-spot formation in solar cells", *Solar Energy Materials and Solar Cells*, vol. 94, no. 2, pp. 106–113, 2010. DOI: [10.1016/j.solmat.2009.09.016](https://doi.org/10.1016/j.solmat.2009.09.016).
- [211] A. Calcabrini, R. Weegink, P. Manganiello, M. Zeman, and O. Isabella, "Simulation study of the electrical yield of various pv module topologies in partially shaded urban scenarios", *Solar Energy*, vol. 225, pp. 726–733, 2021. DOI: [10.1016/j.solener.2021.07.061](https://doi.org/10.1016/j.solener.2021.07.061).
- [212] K. A. Kim and P. T. Krein, "Reexamination of photovoltaic hot spotting to show inadequacy of the bypass diode", *IEEE Journal of Photovoltaics*, vol. 5, no. 5, pp. 1435–1441, 2015. DOI: [10.1109/jphotov.2015.2444091](https://doi.org/10.1109/jphotov.2015.2444091).

- [213] A. Calcabrini, M. Muttillio, R. Weegink, P. Manganiello, M. Zeman, and O. Isabella, "A fully reconfigurable series-parallel photovoltaic module for higher energy yields in urban environments", *Renewable Energy*, vol. 179, pp. 1–11, 2021. DOI: [10.1016/j.renene.2021.07.010](https://doi.org/10.1016/j.renene.2021.07.010).
- [214] O. Kunz, R. J. Evans, M. K. Juhl, and T. Trupke, "Understanding partial shading effects in shingled pv modules", *Solar Energy*, vol. 202, pp. 420–428, 2020. DOI: [10.1016/j.solener.2020.03.032](https://doi.org/10.1016/j.solener.2020.03.032).
- [215] N. Klasen, F. Lux, J. Weber, T. Roessler, and A. Kraft, "A comprehensive study of module layouts for silicon solar cells under partial shading", *IEEE Journal of Photovoltaics*, 2022. DOI: [10.1109/jphotov.2022.3144635](https://doi.org/10.1109/jphotov.2022.3144635).
- [216] M. Green, E. Gauja, and W. Withayachamnankul, "Silicon solar cells with integral bypass diodes", *Solar cells*, vol. 3, no. 3, pp. 233–244, 1981. DOI: [10.1016/0379-6787\(81\)90005-3](https://doi.org/10.1016/0379-6787(81)90005-3).
- [217] H. Yoshioka, S. Nishikawa, S. Nakajima, *et al.*, "Non hot-spot pv module using solar cells with bypass diode function", in *25th IEEE Photovoltaic Specialists Conference (PVSC)*, IEEE, 1996, pp. 1271–1274. DOI: [10.1109/pvsc.1996.564364](https://doi.org/10.1109/pvsc.1996.564364).
- [218] K. Chen, D. Chen, Y. Zhu, and H. Shen, "Study of crystalline silicon solar cells with integrated bypass diodes", *Science China Technological Sciences*, vol. 55, no. 3, pp. 594–599, 2012. DOI: [10.1007/s11431-011-4712-6](https://doi.org/10.1007/s11431-011-4712-6).
- [219] T. Schweigstill, A. Spribille, J. D. Huyeng, F. Clement, and S. W. Glunz, "Stable reverse bias or integrated bypass diode in hip-mwt+ solar cells", *EPJ Photovoltaics*, vol. 13, no. 5, 2022. DOI: [10.1051/epjpv/2021016](https://doi.org/10.1051/epjpv/2021016).
- [220] W. P. Mulligan, D. H. Rose, M. J. Cudzinovic, *et al.*, "Manufacture of solar cells with 21% efficiency", in *19th European Photovoltaic Solar Energy Conference and Exhibition (EU PVSEC)*, vol. 387, 2004.
- [221] D. D. Smith, P. J. Cousins, A. Masad, *et al.*, "Generation III high efficiency lower cost technology: Transition to full scale manufacturing", in *38th IEEE Photovoltaic Specialists Conference (PVSC)*, IEEE, 2012, pp. 1594–1597. DOI: [10.1109/pvsc.2012.6317899](https://doi.org/10.1109/pvsc.2012.6317899).
- [222] D. D. Smith, P. J. Cousins, A. Masad, *et al.*, "SunPower's Maxeon Gen III solar cell: High efficiency and energy yield", in *39th IEEE Photovoltaic Specialists Conference (PVSC)*, IEEE, 2013, pp. 908–913. DOI: [10.1109/pvsc.2013.6744291](https://doi.org/10.1109/pvsc.2013.6744291).
- [223] H. Chu, L. J. Koduvelikulathu, V. D. Mihailtchi, G. Galbiati, A. Halm, and R. Kopecek, "Soft Breakdown Behavior of Interdigitated-back-contact Silicon Solar Cells", *Energy Procedia*, vol. 77, pp. 29–35, 2015. DOI: [10.1016/j.egypro.2015.07.006](https://doi.org/10.1016/j.egypro.2015.07.006).
- [224] R. Müller, C. Reichel, J. Schrof, *et al.*, "Analysis of n-type IBC solar cells with diffused boron emitter locally blocked by implanted phosphorus", *Solar Energy Materials and Solar Cells*, vol. 142, pp. 54–59, 2015. DOI: [10.1016/j.solmat.2015.05.046](https://doi.org/10.1016/j.solmat.2015.05.046).
- [225] K. Yoshikawa, H. Kawasaki, W. Yoshida, *et al.*, "Silicon heterojunction solar cell with interdigitated back contacts for a photoconversion efficiency over 26%", *Nature energy*, vol. 2, no. 5, pp. 1–8, 2017. DOI: [10.1038/nenergy.2017.32](https://doi.org/10.1038/nenergy.2017.32).

- [226] K. Yoshikawa, W. Yoshida, T. Irie, *et al.*, “Exceeding conversion efficiency of 26% by heterojunction interdigitated back contact solar cell with thin film si technology”, *Solar Energy Materials and Solar Cells*, vol. 173, pp. 37–42, 2017. DOI: [10.1016/j.solmat.2017.06.024](https://doi.org/10.1016/j.solmat.2017.06.024).
- [227] C. Hollemann, F. Haase, S. Schäfer, J. Krügener, R. Brendel, and R. Peibst, “26.1%-efficient POLO-IBC cells: Quantification of electrical and optical loss mechanisms”, *Progress in Photovoltaics: Research and Applications*, vol. 27, no. 11, pp. 950–958, 2019. DOI: [10.1002/pip.3098](https://doi.org/10.1002/pip.3098).
- [228] G. Yang, P. Guo, P. Procel, *et al.*, “High-efficiency black IBC c-Si solar cells with poly-Si as carrier-selective passivating contacts”, *Solar Energy Materials and Solar Cells*, vol. 186, pp. 9–13, 2018. DOI: [10.1016/j.solmat.2018.06.019](https://doi.org/10.1016/j.solmat.2018.06.019).
- [229] P. Wang, R. Sridharan, X. R. Ng, J. W. Ho, and R. Stangl, “Development of TOPCon tunnel-IBC solar cells with screen-printed fire-through contacts by laser patterning”, *Solar Energy Materials and Solar Cells*, vol. 220, 2021. DOI: [10.1016/j.solmat.2020.110834](https://doi.org/10.1016/j.solmat.2020.110834).
- [230] C. Reichel, R. Müller, F. Feldmann, A. Richter, M. Hermle, and S. W. Glunz, “Influence of the transition region between p- and n-type polycrystalline silicon passivating contacts on the performance of interdigitated back contact silicon solar cells”, *Journal of Applied Physics*, vol. 122, no. 18, 2017. DOI: [10.1063/1.5004331](https://doi.org/10.1063/1.5004331).
- [231] C. Hollemann, F. Haase, M. Rienäcker, *et al.*, “Separating the two polarities of the POLO contacts of an 26.1%-efficient IBC solar cell”, *Scientific reports*, vol. 10, no. 1, pp. 1–15, 2020. DOI: [10.1038/s41598-019-57310-0](https://doi.org/10.1038/s41598-019-57310-0).
- [232] M. B. Hartenstein, C. Stetson, W. Nemeth, *et al.*, “Trap-assisted dopant compensation prevents shunting in poly-si passivating interdigitated back contact silicon solar cells”, *ACS Applied Energy Materials*, vol. 4, no. 10, pp. 10774–10782, 2021. DOI: [10.1021/acsaem.1c01775](https://doi.org/10.1021/acsaem.1c01775).
- [233] P. J. Verlinden, M. Aleman, N. Posthuma, *et al.*, “Simple power-loss analysis method for high-efficiency Interdigitated Back Contact (IBC) silicon solar cells”, *Solar Energy Materials and Solar Cells*, vol. 106, pp. 37–41, 2012. DOI: [10.1016/j.solmat.2012.06.008](https://doi.org/10.1016/j.solmat.2012.06.008).
- [234] P. Procel, A. Ingenito, R. De Rose, *et al.*, “Opto-electrical modelling and optimization study of a novel IBC c-Si solar cell”, *Progress in Photovoltaics: Research and Applications*, vol. 25, no. 6, pp. 452–469, 2017. DOI: [10.1002/pip.2874](https://doi.org/10.1002/pip.2874).
- [235] P. Procel, G. Yang, O. Isabella, and M. Zeman, “Theoretical evaluation of contact stack for high efficiency IBC-SHJ solar cells”, *Solar Energy Materials and Solar Cells*, vol. 186, pp. 66–77, 2018. DOI: [10.1016/j.solmat.2018.06.021](https://doi.org/10.1016/j.solmat.2018.06.021).
- [236] P. Procel, G. Yang, O. Isabella, and M. Zeman, “Numerical simulations of IBC solar cells based on poly-Si carrier-selective passivating contacts”, *IEEE Journal of Photovoltaics*, vol. 9, no. 2, pp. 374–384, 2019. DOI: [10.1109/jphotov.2019.2892527](https://doi.org/10.1109/jphotov.2019.2892527).

- [237] P. Procel, H. Xu, A. Saez, *et al.*, “The role of heterointerfaces and subgap energy states on transport mechanisms in silicon heterojunction solar cells”, *Progress in Photovoltaics: Research and Applications*, vol. 28, no. 9, pp. 935–945, 2020. DOI: [10.1002/pip.3300](https://doi.org/10.1002/pip.3300).
- [238] R. F. Pierret, “Semiconductor device fundamentals”, in Addison-Wesley Publishing Co., 1996, ch. pn Junction Diode: I-V characteristics, pp. 264–270.
- [239] STMicroelectronics, “How to choose a bypass diode for a silicon panel junction box”, Tech. Rep. AN3432, 2011. [Online]. Available: https://www.st.com/resource/en/application_note/an3432-how-to-choose-a-bypass-diode-for-silicon-panel-junction-box-stmicroelectronics.pdf.
- [240] M. A. Green, “Self-consistent optical parameters of intrinsic silicon at 300 k including temperature coefficients”, *Solar Energy Materials and Solar Cells*, vol. 92, no. 11, pp. 1305–1310, 2008. DOI: [10.1016/j.solmat.2008.06.009](https://doi.org/10.1016/j.solmat.2008.06.009).
- [241] J. C. Ortiz Lizcano, P. Procel, A. Calcabrini, *et al.*, “Colored optic filters on c-Si IBC solar cells for building integrated photovoltaic applications”, *Progress in Photovoltaics: Research and Applications*, 2021. DOI: [10.1002/pip.3504](https://doi.org/10.1002/pip.3504).
- [242] M. Sickmoeller, *IBC technology & manufacturing*, <https://corp.maxeon.com/static-files/c5e8e15e-b191-4bab-96ff-cec504040019>, Accessed: 2022-08-01, 2020.
- [243] J. A. Schwenzer, L. Rakocevic, R. Gehlhaar, *et al.*, “Temperature variation-induced performance decline of perovskite solar cells”, *ACS applied materials & interfaces*, vol. 10, no. 19, pp. 16390–16399, 2018. DOI: [10.1021/acsami.8b01033](https://doi.org/10.1021/acsami.8b01033).
- [244] E. J. Wolf, I. E. Gould, L. B. Bliss, J. J. Berry, and M. D. McGehee, “Designing modules to prevent reverse bias degradation in perovskite solar cells when partial shading occurs”, *Solar RRL*, 2021. DOI: [10.1002/solr.202100239](https://doi.org/10.1002/solr.202100239).
- [245] A. Augusto, A. Srinivasa, and S. G. Bowden, “Influence of the bulk resistivity on silicon heterojunction solar cells and module reliability”, *Solar RRL*, 2021. DOI: [10.1002/solr.202100519](https://doi.org/10.1002/solr.202100519).
- [246] H. Chu, “Interdigitated back contact silicon solar cells: Metallization and reverse bias characteristics”, Ph.D. dissertation, International Solar Energy Research Center Konstanz, 2019. [Online]. Available: <https://kops.uni-konstanz.de/handle/123456789/45903>.
- [247] R. Müller, C. Reichel, J. Benick, and M. Hermle, “Ion implantation for all-alumina IBC solar cells with floating emitter”, *Energy Procedia*, vol. 55, pp. 265–271, 2014. DOI: [10.1016/j.egypro.2014.08.078](https://doi.org/10.1016/j.egypro.2014.08.078).
- [248] S. Yamaguchi, B. B. Van Aken, A. Masuda, and K. Ohdaira, “Potential-induced degradation in high-efficiency n-type crystalline-silicon photovoltaic modules: A literature review”, *Solar RRL*, vol. 5, no. 12, 2021. DOI: [10.1002/solr.202100708](https://doi.org/10.1002/solr.202100708).

LIST OF PUBLICATIONS

PEER-REVIEWED PUBLICATIONS

1. **A. Calcabrini**, H. Ziar, O. Isabella, M. Zeman, *A simplified skyline-based method for estimating the annual solar energy potential in urban environments*, [Nature Energy](#) **4**, 206 (2019).
2. **A. Calcabrini**, R. Weegink, P. Manganiello, M. Zeman, O. Isabella, *Simulation study of the electrical yield of various PV module topologies in partially shaded urban scenarios*, [Solar Energy](#) **225**, 726 (2021).
3. **A. Calcabrini**, M. Muttillio, R. Weegink, P. Manganiello, M. Zeman, O. Isabella, *A fully reconfigurable series-parallel photovoltaic module for higher energy yields in urban environments*, [Renewable Energy](#) **179**, 1 (2021).
4. J. C. Ortiz Lizcano, P. Procel, **A. Calcabrini**, G. Yang, A. Ingenito, R. Santbergen, M. Zeman, O. Isabella, *Colored optic filters on c-Si IBC solar cells for building integrated photovoltaic applications*, [Progress in Photovoltaics](#) **30**, 401 (2022).
5. **A. Calcabrini**, P. P. Moya, B. Huang, V. Kambhampati, M. Zeman, P. Manganiello, O. Isabella, *Low breakdown voltage solar cells for shading tolerant photovoltaic modules*, [Cell Reports Physical Science](#) **3**, 101155 (2022).
6. **A. Calcabrini**, R. Cardose, D. Gribnau, B. Pavel, P. Manganiello, M. Zeman, O. Isabella, *Time-varying, ray tracing irradiance simulation approach for photovoltaic systems in complex scenarios with decoupled geometry, optical properties and illumination conditions*, [Progress in Photovoltaics](#) **31**, 134 (2023).
7. **A. Calcabrini**, M. Muttillio, M. Zeman, P. Manganiello, O. Isabella, *Experimental evaluation of the electrical performance of a fully reconfigurable series-parallel PV module*, Nature Communications (Under review).

CONFERENCE CONTRIBUTIONS AS FIRST AUTHOR

1. **A. Calcabrini**, H. Ziar, O. Isabella, M. Zeman, *Simplified Model for Solar Energy Potential Estimation in Urban Environments*, 35th EUPVSEC **1AO.2.1**, (2018).
2. **A. Calcabrini**, R. Weegink, O. Isabella, M. Zeman, *The Ultimate Potential of Reconfigurable Modules for Increasing the Energy Yield of Partially Shaded Urban Photovoltaics Systems*, 36th EUPVSEC **1AO.2.1**, (2019).

3. **A. Calcabrini**, O. Isabella, M. Zeman, *Photovoltaics in the urban environment: towards a fast, accurate and remote 3D-based energy potential simulation framework*, 29th PVSEC **11ThO1**, (2019).
4. **A. Calcabrini**, R. Weegink, O. Isabella, M. Zeman, *A Simulation Study of Reconfigurable Modules for Higher Yields in Partially Shaded PV Systems*, 47th IEEE PVSC, Oral presentation, (2020).
5. **A. Calcabrini**, R. Cardose, O. Isabella, M. Zeman, *Accurate Irradiance Simulation Approach Combining Ray Tracing and View Factors Models*, 37th EUPVSEC **5BO.6.1**, (2020).
6. **A. Calcabrini**, R. Weegink, O. Isabella, M. Zeman, *Reconfigurable Modules for Higher Yields in Urban PV Systems – A Simulation Study*, 37th EUPVSEC **1AO.3.5**, (2020).
7. **A. Calcabrini**, V. Kambhampati, P. Manganiello, O. Isabella, M. Zeman *The Relevance of the Cell's Breakdown Voltage in the DC Yield of Partially Shaded PV Modules*, 48th IEEE PVSC, Oral presentation, (2021).
8. **A. Calcabrini**, M. Muttillio, M. Zeman, P. Manganiello, O. Isabella, *Prototyping and Testing of a Fully Reconfigurable Series-Parallel PV Module*, 38th EUPVSEC **1AO.3.2**, (2021).
9. **A. Calcabrini**, V. Kambhampati, P. Manganiello, M. Zeman, O. Isabella, *Characterization of Low Breakdown Voltage c-Si Solar Cells and Implications on the Annual DC Yield of Partially Shaded c-Si Modules*, 38th EUPVSEC **4AV.2**, (2021).
10. **A. Calcabrini**, D. Gribnau, R. Cardose, P. Manganiello, M. Zeman, O. Isabella, *Novel Spectral Irradiance Simulation Approach for PV Systems in Geometrically Complex Environments*, 8th WCPEC **4BO.16**, (2022).
11. **A. Calcabrini**, M. Muttillio, P. Manganiello, M. Zeman, O. Isabella, *Presentation Title: Outdoor Monitoring Results of a Full-Scale Reconfigurable PV Module*, 8th WCPEC **3BO.12**, (2022).

CURRICULUM VITAE

Andres Calcabrini was born in Quilmes (Buenos Aires, Argentina) on February 17, 1991. In 2014 he received his B.Eng. degree in Electronic Engineering from Buenos Aires Institute of Technology and in 2015 he received his Electronic Engineering diploma from the same institution. In 2015 he moved to the Netherlands where he pursued a M.Sc. degree in Sustainable Energy Technology at Delft University of Technology. In 2018 he started working towards his Ph.D. degree in the Photovoltaics Materials and Devices group at Delft University of Technology under the supervision of Prof.dr. Miro Zeman, Prof.dr. Olindo Isabella and Dr. Patrizio Manganiello. During his Ph.D. he developed models for the simulation of the energy yield of photovoltaic systems in the urban environment and investigated different concepts to improve the electrical performance of photovoltaic systems in partial shading conditions. For the research carried out during his Ph.D., he was awarded with the EU PVSEC Student Award in the 36th EU PVSEC conference in 2019, the PVMD Apple Prize in the same year, and the Best Student Paper Award in the 48th IEEE PVSC conference in 2021. After a brief foray into vehicle integrated photovoltaics, he is currently working on the next generation of energy yield simulation software tools for utility scale and commercial PV plants.